OPTICAL COHERENCE TOMOGRAPHY FOR CLINICAL OTOLOGY

by

Daniel Ryan MacDougall

Submitted in partial fulfillment of the requirements
for the degree of Doctor of Philosophy

at

Dalhousie University
Halifax, Nova Scotia
January 2020

To my parents, neither of whom got to see me complete my graduate work. They gave me the drive to do challenging things.

Table of Contents

List of Tables . . . . . **vii**

List of Figures . . . . . **viii**

Abstract . . . . . **xvi**

List of Abbreviations and Symbols Used . . . . . **xvii**

Acknowledgements . . . . . **xxi**

Chapter 1 Introduction **1**

1.1 Motivation 1

1.2 Background 4
1.2.1 Anatomy and Physiology of the Ear 4
1.2.2 Conductive Hearing Loss: Causes and Interventions 5
1.2.3 Diagnostics in Conductive Hearing Loss 10
1.2.4 Optical Coherence Tomography 13

1.3 Literature Review 17
1.3.1 Laser Doppler Vibrometry 17
1.3.2 Anatomical OCT in the Middle Ear 22
1.3.3 Optical Coherence Tomography Doppler Vibrography 23
1.3.4 Otological High-Frequency Ultrasonography 25

1.4 Format of this Thesis 25

Chapter 2 Requirements Discovery for Optical Coherence Tomography Imaging of the Human Middle Ear **28**

2.1 Author Contribution Statement 28

2.2 Preamble 28

2.3 Abstract 29

2.4 Introduction 29
2.4.1 Motivation 29
2.4.2 Anatomical Constraints 30
2.4.3 Key Challenges of OCT-Based Middle Ear Imaging 32

2.5 Methods 36

2.6 Results . . . 39
2.6.1 Optical Loss Across the Tympanic Membrane . . . 39
2.6.2 Digital Tympanotomy . . . 41
2.6.3 Diagnostic Validation . . . 42

2.7 Discussion . . . 43
2.7.1 Multiple Scattering in the Ossicles . . . 43
2.7.2 Design Considerations . . . 44
2.7.3 Clinical Relevance . . . 45

2.8 Conclusions . . . 47

Chapter 3 The Development of a Swept-Source Optical Coherence Tomography Imaging System with Doppler-Vibrographic Sensitivity at the Ossicles, *in vivo* . . . 49

3.1 Author Contribution Statement . . . 49

3.2 Preamble . . . 49

3.3 Abstract . . . 50

3.4 Introduction . . . 50
3.4.1 Motivation . . . 51
3.4.2 Background . . . 52
3.4.3 Vernier-Tuned Distributed Bragg Reflector Lasers: the Enabling Technology . . . 52
3.4.4 Relevant Imaging Probes/Heads . . . 55

3.5 Methods . . . 55
3.5.1 OCT Engine Design . . . 56
3.5.2 Synchronization of the VT-DBRL . . . 58
3.5.3 Extraction of Doppler Vibrographic Information . . . 59
3.5.4 Real-Time Acceleration on a Graphics Processing Unit . . . 61
3.5.5 Patient-Compatible Scanning Optics . . . 65

3.6 Results . . . 66
3.6.1 *Ex vivo* Imaging . . . 66
3.6.2 *In vivo* Anatomical Imaging . . . 68
3.6.3 *In vivo* OCT-DV Measurements . . . 70

3.7 Discussion . . . 72
3.7.1 Artifact-Free Dynamic Range . . . 72
3.7.2 Practical OCT-DV Sensitivity . . . 75
3.7.3 OCT-DV Processing Speed . . . 75
3.7.4 Segmentation and Motion Artifact in OCT-DV . . . 75

3.7.5 Time-Scaling and Duty-Cycle Improvements 77
3.7.6 Patient Comfort and Practicality of the Microscope 78
3.7.7 Processing Implications of Synchronization 78
3.7.8 Integrated Automatic Gain Control 80

3.8 Conclusions 81

Chapter 4 Applying Optical Coherence Tomography Doppler Vibrography to Clinical Otology: Discriminating Stapes Fixation from Normal 82

4.1 Author Contribution Statement 82

4.2 Preamble 82

4.3 Abstract 83

4.4 Introduction 84
4.4.1 Motivation 84
4.4.2 Optical Vibrometry and Stapes Fixation 85
4.4.3 Diagnosing Otosclerosis Without Vibrometry 86

4.5 Methods 87
4.5.1 Subject Recruitment 87
4.5.2 Optical Coherence Tomography Doppler Vibrography 88
4.5.3 System Improvements 89
4.5.4 Imaging Procedure 91

4.6 Results 92
4.6.1 Sample Statistics 92
4.6.2 Discrimination Between Normal and Otosclerotic Ears 93

4.7 Discussion 95
4.7.1 Study Limitations 95
4.7.2 Anomalous Functional Response in Otosclerotic Ear 00163 . . 97
4.7.3 Comparison to Laser Doppler Vibrometry 98

4.8 Conclusions 99

Chapter 5 Discussions 101

5.1 Continued Development: Mark II 101
5.1.1 Contribution Statement 101
5.1.2 Mechanical Design 102
5.1.3 Optical Design 102

5.2 Pathway to Adoption 104

5.3 Evidence of Clinical Utility: Transtympanic OCT Patient Cases . . . 106
5.3.1 Generating Evidence Against Simple Stapes Fixation 107
5.3.2 Visualizing Perforations of the Tympanic Membrane 107
5.3.3 Assessing Retractions and Sound Coupling to the Ossicles . . 110
5.3.4 Revealing Unknown Surgical Histories 111
5.3.5 Objective Evidence of Partial Ossicular Discontinuity in "Sniffer-Poppers" 112
5.3.6 Visualizing Traumatic Ear Injury 114
5.3.7 Detecting Foreign Objects Behind the TM 116

5.4 Current Limitations of the System 116
5.4.1 Accessible Volume of Interest 116
5.4.2 Imaging Through Tympanoplasties 118
5.4.3 Practical Noise-Floor Limits in *In Vivo* OCT-DV 118

Chapter 6 Conclusion 121

Bibliography 125

Appendix A Computed Tomography Resolution 141

Appendix B The Importance of Coherence Length 144

Appendix C Permissions of Reproduction 147

List of Tables

Table 1.1 Additional anatomical structures in the middle ear referenced in this work, and brief descriptions of their physiological roles in hearing 7

Table 4.1 Statistical summary of peak-to-peak displacement measurements performed at the umbo and lenticular process of the incus in patients with presumptive otosclerosis and in normal controls using OCT-DV at a stimulus pressure of $P_a = 100\text{dB}_{SPL}$. 95% confidence intervals are indicated in square brackets. **M** sample mean, **SD** sample standard deviation. 93

Table 4.2 Summary of ROC analysis for the discrimination of presumptive otosclerosis from normal controls using OCT-DV at the umbo and lenticular process of the incus at stimulus frequencies of 500Hz and 1000Hz. Optimal threshold is calculated as the threshold giving the maximum Youden J-index. 95% confidence intervals are indicated in square brackets. **AUC** area under ROC curves from Figure 4.4. 95

List of Figures

Figure 1.1 Human hearing anatomy. A, showing the external and inner ears, and the middle ear, which is the anatomical region of most relevance to this work. B, detailed view of the middle ear and its specific anatomical structures relevant to this work (taken and modified with permission from [1]). 6

Figure 1.2 Resolution in CT. A, Magnified depiction of the incus and stapes. B, Example of the ossicles as imaged by high-resolution CT (taken from [2] with permission). C, Magnification of B to approximately the same scale as A to illustrate the resolution limitation of CT in otology 13

Figure 1.3 Basic Configuration of a TD-OCT system, illustrating the conceptual foundation for low-coherence interferometry with a variable length reference arm. **SLD** superluminescent diode, **BS** beam splitter, **PD** photo-detector, **REF** reference arm of interferometer, **SAM** sample arm of interferometer, $\boldsymbol{\Delta z}$ relative path length difference between reference and sample arms, **z** depth axis of the measurement referenced to the relative path length difference. 15

Figure 1.4 Typical configuration used in the literature for non-invasive LDV measurements down the ear canal, *in vivo*. A, A typical experimental setup with a sound source and microphone, and an open port to couple the LDV into the external canal. B, A sketch of the TM and the most common site of velocity measurement at the umbo (taken from [3] with permission). . 20

Figure 2.1 Diagram of the desired OCT system for transtympanic imaging of the middle ear showing the coordinate axes, x,y,z, used throughout the work, the basic imaging configuration down the ear canal, and the lateral and axial extents of the VOI, defined by z_D and D_{FOV}. **TM** tympanic membrane, **M** malleus, **IN** incus, **S** stapes, **OCT** optical coherence tomography. 32

Figure 2.2 Detailed schematic of the TD-OCT imaging system assembled for this work. **IM** image sensor, **L** en-face imaging lens, **PBS** polarizing beam splitter, **OBJ** objective lens, **S** speculum , **COL** collimating lens, **QWP** quarter-wave plate, **HWP** half-wave plate, **GV** galvanometer mirror, **BS** fiber beam splitter, **C** fiber circulator, **PD** photodiode, **SLD** supler luminescent diode, **RSOD** rapid scanning optical delay line. 34

Figure 2.3 SNR comparison of transtympanic 2D B-mode images of a normal cadaveric ear at different framerates. SNR at the incus is indicated in each image. All three images are displayed with 35 dB dynamic range starting 5 dB above the RMS noise floor for the $f_r = 0.5FPS$ configuration. **IN** incus, **M** malleus, **TM** tympanic membrane, **CF** cochlear floor. 35

Figure 2.4 Experimental setup used for measurement of the transmittance of the TM. A, A diagram of the physical arrangement where paper was used as an OCT reference reflector behind a section of excised human TM over a clear aperture. B, OCT image of the arrangement described in A. **TM** tympanic membrane. . . 40

Figure 2.5 3D reconstructions of a normal cadaveric middle ear. A, With the TM surgically lifted. B, With the TM in placed but removed by digital tympanotomy. C, With the TM shown in transparent green. **M** malleus, **IN** incus, **S** stapes. 41

Figure 2.6 Images of ELPI. A, Diagram, B, 2D B-Mode image and, C, 3D volumetric image of a cadaveric ear in which a surgical manipulation has been made to the incus to simulate erosion of the long process. The curly brace highlights a region containing significant multiple scattering artifact within the bony ossicles. **TM** tympanic membrane, **M** malleus, **IN** incus, **S** stapes, **ELPI** erosion of the long process of the incus. 42

Figure 2.7 Images of a PORP. A, Diagram, B, 2D image and, C, 3D volumetric image of a cadaveric ear in which a partial ossicular reconstruction prothesis was implanted correctly at the stapes but deliberately left unattached to the tympanic membrane to simulate migration. Both the prosthesis and the gap between it and the TM are visible in the images. **TM** tympanic membrane, **S** stapes, **PORP** partial ossicular replacements prosthesis. . 43

Figure 2.8 The benchtop TD-OCT system used during (and retired immediately following) the work in Chapter 2 48

Figure 3.1 Diagram of the SS-OCT system designed for real-time, transtympanic human middle ear imaging *in vivo*. **FPGA** field programmable gate array, **DAC** digital-to-analog converter, **ADC** analog-to-digital converter, **LAS** wavelength swept laser, **TIA** trans-impedance amplifier, **V** voltage amplifier, **SPK** speaker, **GV** galvanometer mirror, **BS** fiber beam splitter, **PC** personal computer, **GPU** graphics processing unit. 57

Figure 3.2 Conceptual diagram describing the memory and grid structure of the CUDA streams used for, A, pre- and, B, post-DFT processing the raw unstitched interferometric data. **DVV** data valid vector describing the pattern of invalid data to be ignored in the spectral interferograms, **NORM** complex-valued normalization vector used for ripple-rejection, dispersion compensation and windowing prior to discrete Fourier-transformation, **GRID** array of threads of executions running in parallel on the GPU during execution. 64

Figure 3.3 The SS-OCT system developed for *in vivo* transtympanic, full middle ear imaging. A, Optical layout with a pupil image located at the tip of the speculum to provide and wide field-of-view and access the full volume of interest in the middle ear. B, Closeup of the middle ear OCT scanning microscope used for imaging down the ear canal through a 4 mm otoscopic speculum and mounted to a surgical microscope arm. C, Complete in-clinic, real-time imaging setup. Units in A are in mm. . . . 67

Figure 3.4 *Ex vivo* OCT-DV response in a cadaveric right ear at a nominal acoustic frequency of $f_a = 625$Hz (≈ 515Hz actual) showing a cross-sectional view of the ear's measured peak-to-peak vibrational response, A, without acoustic stimulus and, B, with stimulus applied at 100dB$_{\text{SPL}}$. C and D show the color-mapped vibrational response to stimulus in 3D before and after digital removal of the TM. Supplementary File A shows a 3D rendered volume of the full vibrational response. Supplementary File B uses the same data to animate the middle ear's vibrational response. **TM** tympanic membrane, **M** malleus, **IN** incus, **CP** cochlear promontory. 69

Figure 3.5 Images of stapes piston, *in vivo*. A, Illustration of the placement of a stapes piston prosthesis during stapedotomy surgery (taken from [4] with permission, illustration by Anne Johnson). B, *In vivo* 3D render of a patient's middle ear containing a stapes piston prosthethis, clearly showing the crimp of the piston around the long process of the incus (see Supplementary File E). C) and D) show real-time 2D B-mode images comparing the appearance of normal incus bone, characterized by gradual signal drop-off and multiple scattering, to the appearance of the titanium prosthesis, characterized by a single strong surface reflection. **TM** tympanic membrane, **IN** incus, **SP** stapes piston prosthesis, **CP** cochlear promontory, **M** malleus. 71

Figure 3.6 *In vivo* real-time OCT-DV measurement in a normal left ear's response to sound at 1030Hz. A shows a $10 \times 10\text{mm}^2$ 2D cross-section of the middle ear in the transverse plane. Supplementary File C shows the macroscopic changes to the ear anatomy during a Valsalva maneuver. B Shows a $10\times10\times10\text{mm}^3$ 3D volume render of the middle ear as seen from the perspective of the ear canal with the TM digitally removed (see Supplementary File D). C, shows the same volume from an inferior-posterior perspective with the TM in-place showing the axis of OCT-DV measurement along the yellow line passing through the incus at the stapedius tendon. Functional measurements of the TM and incus' peak-to-peak vibrational response at 1030Hz are shown in D with a $P_0 = 100\text{dB}_{SPL}$ tone applied to the ear and in E without stimulus. F, Peak-to-peak displacement of the incus versus presentation level showing good linearity from 80dB_{SPL} to $100\text{dB}_{\text{SPL}}$. Error bars represent $\pm$ one standard deviation of the response over the pixels along the axial length of the incus. **TM** tympanic membrane, **M** malleus, **IN** incus, **IS** incudostapedial joint, **ST** stapedius tendon, **CT** chorda tympani, **CP** cochlear promontory, **RW** round window. 73

Figure 3.7 Image artifacts arising from imperfections in the PSF of the VT-DBRL. A, A 2D B-Mode image through the malleus. B, Selected A-lines from A corresponding by colour. Blue is a representative line of noise only, yellow intersects the malleus, and red intersects the cochlear promontory. In B, the dotted line shows where the black-threshold is set to display the images without the artifact apparent, and that in our system the quality of the PSF improved with increasing z in B. **TM** tympanic membrame, **M** malleus, **CP** cochlear promontory. 74

Figure 3.8 Example of the extraction of the OCT-DV signal showing both A-line magnitude and the extracted OCT-DV signal. A is taken in an exceptionally still patient while B is taken in a patient with a typical amount of motion during the measurement time. The green areas show the subjectively determined spatial averaging window, and the red shows areas that have been manually rejected due to motion artifact. 76

Figure 4.1 Experimental setup and representative sample of images produced from a typical session for imaging patient volounteers and normal controls. A, The mounted OCT-DV scanning head. B, The imaging system oriented along a volounteer's ear canal to visualize the TM and ossicles. C, A 3D rendering of a middle ear with the TM digitally removed via *digital tympanotomy* to reveal the ossicles and showing transverse cross-sectional cut-planes through the umbo and lenticular process of the incus. D, Cross-sectional image through the incus showing a color-mapped vibration measurement on the lenticular process of the incus. E, Cross-sectional imaging through the malleus showing a vibration measurement on the umbo. Averaging of the vibration amplitudes is done over the pixels located between red dots in D-E. **TM** tympanic membrane, **A** anterior anatomical direction **L** lateral anatomical direction, **S** superior anatomical direction, **XI** incus cross-section, **XU** umbo cross-section. . . . 89

Figure 4.2 Mechanical adjustment setup of the microscope to reduce patient discomfort. At top, showing the mechanics of alignment of the microscope head to the ear canal from Chapter 3, which caused subject pain during adjustment. At bottom, the upgrade made to the fine alignment mechanics, as it was used in Chapter 4 to reduce subject discomfort. 90

Figure 4.3 Sample distributions of measured vibrational response for the presumed otosclerotic and normal control groups. A, At the umbo with a stimulus frequency of 500Hz. B, At the umbo with a stimulus frequency of 1000Hz. C, At the incus with a stimulus frequency of 500Hz. D, At incus with a stimulus frequency of 1000Hz. Black arrows point to anomalous vibration observed at the umbo of patient 0163. 94

Figure 4.4 Receiver-operating-characteristic analysis for vibration measurements performed at the umbo and incus, at stimulus frequencies of $f_a = 500$ and $f_a = 1000Hz$, and $P_a = 100\text{dB}_{SPL}$ 96

Figure 5.1 Design of the Mark II clinical imaging system. A, A ray-tracing diagram of the optical system internal to the hand-piece. B, A 3D section view of the internal components within the hand-piece. C, A photograph of the assembled console and hand-piece. 103

Figure 5.2 The Mark II user interface. A, The wireless controller that allows a single operator to select structures and initiate measurements while using the hand-piece. B, A screen capture from the graphical user interface showing a simultaneous 2D B-Mode image and an en-face otoscopic image. 104

Figure 5.3 Contributing factors to the successful adoption of medical technology and innovation (taken from [5] under fair dealing). . . . 105

Figure 5.4 OCT images from patient 00190, *in vivo*, pre-operatively diagnosed with otosclerosis. A, OCT-DV results at the umbo. B, OCT-DV results at the incus. OCT-DV measurements were taken at $P_a = 100\text{dB}_{SPL}$. 108

Figure 5.5 OCT images of a nearly complete TM perforation in patient 01199220331, *in vivo*. A, A 3D rendering of the middle ear as seen from the ear canal, and B, as seen from the medial side of the middle ear. C, A 2D B-Mode image and OCT-DV measurements taken at the umbo, and D, at the incus. OCT-DV measurements were taken at $P_a = 100\text{dB}_{SPL}$. 109

Figure 5.6 OCT images of a partial TM perforation in Patient 00101, *in vivo*. A shows a 3D volumetric rendering of the TM perforation. **XM** indicates the location of the cross section shown in B, a 2D B-mode image with OCT-DV measurement on the malleus. **XRW** indicates the location of the cross-section shown in C, a 2D B-mode image with OCT-DV measurements on the round window. OCT-DV measurements were taken at $P_a = 100\text{dB}_{SPL}$. 110

Figure 5.7 Images of the left ear in patient 01199220131 with an adhesive retraction pocket. A, an en-face IR otoscopic image of the ossicles and TM. **XI** indicates the location of the 2D B-mode image of the retraction pocket adhered to the incus shown B. B also shows OCT-DV measurements of incus displacement. **XU** indicates the location of the 2D B-mode image of the malleus in C. C also shows OCT-DV measurements of umbo displacement. OCT-DV measurements were taken at $P_a = 100\text{dB}_{SPL}$. 111

Figure 5.8 Anatomical and OCT-DV image acquired from a patient who had reported *no history* of middle ear surgery to the clinic. The image clearly shows the presence of a silastic sheet medial to the eardrum, likely placed there either by a magical being of some kind, or during a previous middle ear surgery. The sound induced peak-to-peak displacements of the visible structures were probed with OCT-DV, shown by the color mapped overlay and annotations. Interestingly, there is some activation of the sheet, indicating that it is mechanically coupled to the ossicles and may be contributing to the CHL. OCT-DV measurements were taken at $f_a = 500\text{Hz}$ and $P_a = 100\text{dB}_{SPL}$. 113

Figure 5.9 Transtympanic OCT images taken in a patient's right ear whose CHL improves following a valsalva maneuver, but returns after pressure equalization. A, Showing umbo displacement measured immediately before and, B, immediately after pressurizing the middle ear. 114

Figure 5.10 OCT images acquired in patient 00200, who suffered traumatic perforation of the TM and disruption of the ossicles following complications during temporomandibular arthroscopy. A, A render of the 3D volume with the abnormal configuration of the ossicles highlighted with dotted lines. B, A 2D B-mode image through the incus and the malleus at the umbo, showing that the malleus has medialized $\approx 1.5\text{mm}$ away from the TM. B shows OCT-DV measurements of incus activation. C shows a 2D B-mode image with OCT-DV measurements of activation at the umbo where it remains coupled to the TM, half way up the manubrium. **TM** tympanic membrane, **IN** incus, **ST** stapedius tendon, **CP** cochlear promontory, **M** malleus, **MC** inferior mallear contact point with the TM, **MED** medialization. 115

Figure 5.11 Anatomical images of tympanostomy tubes, *in vivo*. A, IR otoscopy, and B, a 3D rendering of OCT of the TM and tube in patient 01199220531. C shows the surface of a medialized tube hidden behind the TM in patient 01199220611, which has been emphasized by adding transparency to the TM and increasing brightness with axial depth. 116

Figure 5.12 Accessible volume of interest for different form factors the device could take, including surgical microscopes, wide-field otoscopes like the devices demonstrated in this work, and forward-facing or angled otoendoscopes, which could provide the best visualization of the epitympanum. 117

Figure 5.13 The deleterious effects of tympanoplasty on transtympanic middle ear image. A, A diagram of "palisade" tympanoplasty (taken from [4] with permission, illustration by Anne Johnson). B, A surgical microscope view of a healed cartilage tympanoplasty. **XC** indicates the location of the 2D B-Mode image shown in C of the tympanoplasty with no ability to resolve the ossicles. 118

Figure 5.14 Distribution of OCT-DV measurements at $f_a = 1000$Hz across 300 pixels taken in a single subject at the incus, *in vivo*. A, density distributions of displacement magnitude. B and C, polar plots showing the complex pixel values from the OCT-DV data in A at different scales. For each condition, 10 measurements were performed a few seconds apart, with 30 pixels extracted from each. Red shows measurements with no sound stimulus playing, blue shows measurements with stimulus at $P_a = 100\text{dB}_{SPL}$, and green shows measurement taken in a stationary reflector sitting on a table. Measurements were 2s in duration ($M \times N = 204,800$ in Equation 3.9). 120

Figure B.1 Left, A generic SS-OCT setup, including a tunable wavelength laser, fiber coupler, or splitter for splitting and interfering the reference and sample beams, a lateral beam scanning mechanism, and detection and processing electronics. Right, Confocal gating in OCT due to the sample arm optics (taken from [6] with permission). 145

Abstract

The potential utility of OCT for diagnostics in otology has been acknowledged for nearly two decades, but studies have focused largely on application to understanding basic physiology where animals and cadavers can be used, or where only the tympanic membrane is of interest. We performed benchtop experiments in human cadavers with a custom OCT system to understand the design challenges and practicalities of moving towards its application to live, awake subjects with real-world pathologies of the middle ear. We quantify the deleterious effects of imaging the middle ear volume through the intact tympanic membrane, and demonstrate new clinical applications of imaging erosions of the osscicles and post-operative ossicular prosthesis tracking. New swept-laser technology enabled fast and phase-stable OCT measurements that capture both structure and displacement simultaneously in a technique called OCT-DV, the functionality of which was integrated into a mounted microscope suitable for use in live humans. The system allowed viewing of the full lateral and axial extents of the tympanic membrane and middle ear cavity, and was used to perform the first in vivo OCT-DV measurements in live humans, notably at the incus through the intact tympanic membrane. Special effort was made to make the system provide immediate, real-time results to the operator for maximum usability, and relied on GPU acceleration of OCT-DV. The same system was applied to cohorts of individuals with normal hearing (N=42 ears), and of individuals clinically diagnosed with otosclerotic stapes fixation (N=13 ears). We show that the OCT-DV implementation in our instrument was able to discriminate between the two samples with particularly good sensitivity (1.00) and specificity (0.98) using absolute peak-to-peak displacement measured at the incus at a stimulus frequency of 500Hz, and that there exist some technical improvements that could better separate the two groups. Specifically, addressing the practical displacement sensitivity penalty incurred in imaging live, awake subjects. We also detail progress on continued development of the system, and present several unique case studies where OCT and OCT-DV can offer additional insight into the state of the middle ear.

List of Abbreviations and Symbols Used

D_{FOV}	Diameter of lateral of field of view
N_l	Number of A-lines drawn per 2D Bmode image
P_0	OCT light source total available power
P_a	Acoustic stimulus presentation level
R_s	Reflectivity of a feature in the sample arm
S_i	OCT Image Sensitivity
T_F	Fresnel transmission coefficient
T_a	Transmittance due to absorption
T_s	Transmittance due to scattering
T_{TM}	Transmittance through the TM (two-way)
Δk	Spectral width of OCT light source, in wavenumbers
$\Delta\lambda$	Spectral width of OCT light source, in wavelength
α	Interferometer optical power splitting ratio
δk	Optical frequency resolution, or instantaneous line width, in wavenumbers
δz	Axial resolution or pixel size along z
$\delta\lambda$	Instantaneous line width
λ_0	Central wavelength
ρ	Responsivity of photo detector
σ_a	Optical absorption coefficient
σ_s	Optical scattering coefficient
τ_c	Coherence time
c	Speed of light in a vacuum
f_l	Unaveraged A-line rate of OCT system
f_r	2D Bmode frame rate
f_s	Tunable laser sweep repetition rate
i_i	Peak detected interference photocurrent
i_n	RMS noise photocurrent

n_r	Index of refraction
q	Charge of an electron
z_D	Maximum axial OCT ranging distance
z_c	Coherence length
e.g.	for example
i.e.	that is
A-line	Amplitude line
AGC	Automatic Gain Control
B-Mode	Brightness-Mode
CHL	Conductive Hearing Loss
CPU	Central Processing Unit
CT	Computed Tomography
CUDA	Compute Unified Device Architecture
DFT	Discrete Fourier Transform
DNR	Dynamic Range
ENT	Otolaryngologist
FD-OCT	Fourier-Domain Optical Coherence Tomography
FFT	Fast Fourier transform
FOV	Field of View
FPS	Frames Per Second
GPU	Graphics Processing Unit
GRIN	Graded Index of Refraction
GUI	Graphical User Interface

HWP	Half Wave Retarder Plate
MEMS	Micro-Electromechanical System
MEMS-VCSEL	Micro-Electromechanical System, Vertical-Cavity, Surface-Emitting Laser
MRI	Magnetic Resonance Imaging
NA	Numerical Aperture
NIR	Near Infrared
OCT	Optical Coherence Tomogrpahy
OR	Operating Room
PSF	Point Spread Function
QWP	Quarter Wave Retarder Plate
RMS	Root-Mean-Squared
RSOD	Rapid Scanning Optical Delay Line
SD-OCT	Spectral-Domain Optical Coherence Tomography
SLD	Superluminescent Diode
SNHL	Sensorineural Hearing Loss
SNR	Signal to Noise Ratio
SPS	Samples Per Second
SS-OCT	Swept-Source Optical Coherence Tomography
TD-OCT	Time-Domain Optical Coherence Tomogrpahy
TM	Tympanic Membrane

US	Ultrasonography
VOI	Volume of Interest
VT-DBRL	Vernier-Tuned, Distributed Bragg-Reflector Laser

Acknowledgements

In approximate chronological order of involvement with this work:

Bridget O'Halloran When I said that I left a good job in a completely unrelated field to go try building microscopes in a dark, windowless room, you were completely supportive. You're the WD-40 to my moving parts.

My Family I realize that a nanometer isn't anything that you care or think about, but the fact that you could appreciate how hard I tried to measure them was instrumental to it happening.

Dr. Robert Adamson I can't even contemplate having taken any route through graduate school other than this one. You know a lot about many things, some about most things, and seemingly, at least a bit of about absolutely everything. There should be more people like you.

Dr. Jeremy Brown You have an endless supply of interesting ideas, and your enthusiasm for technical pursuits is infectious. I've learned that if it comes out of your mouth, digging into the details will just end up showing that you were right from the beginning.

Dr. Manohar Bance Your blend of engineering and clinical know-how makes for research work that has obvious real-world application. More importantly, you indirectly introduced me to Chicken Madras, and for that I am eternally indebted to you.

Dr. Laurent Kreplak Thank you for asking challenging questions and supporting my six years of effort.

Dr. Tom Landry We would never have made a single in vivo measurement without your help with cadavers, first.

Joshua Farrell For 3D visualization and for never shying away from solving a problem with such generality that you also solve five other problems you didn't yet realize you had.

Matthew Jahns For mechanical problem solving, 3D modeling, long sessions scratching our heads, checking things one more time, staying late instead of finishing up in the morning, and for being able to produce cinnamon buns at the drop of a hat.

Loran Morrison For being the first non-engineer to test drive my work and providing an alternate perspective on things.

Christine Morrison For making sure that I take a break to eat lunch, and for being the friendly face that patients see before they have to see mine.

Dr. David Morris For taking the time to answer clinical questions from engineers like me, working on projects like this. The recipe for whatever ingredients went into you turning out the way you have should be kept in one of those bunkers where they keep things we'll need for re-building civilization.

Carmen McKnight For mechanical design, for dealing with manufacturing hiccups, and for knowing that screw holes don't need to be moved if moving them won't make any material difference.

Drew Hubely For debugging wizardry, and for bouncing signal processing ideas back and forth even if neither of us has time to try them out.

Matthew Farrell I have made graphical user interfaces that I was quite proud of, and that weren't one tenth as pretty as the ones that you make.

Chapter 1

Introduction

This thesis describes the development of new diagnostic technology for use in otology using optical coherence tomography. This chapter begins by describing the motivation to address an unmet clinical need for imaging capable of offering a view into the structure and function of the middle ear without requiring exploratory surgery. This is followed by technical background information that describes hearing physiology, relevant pathologies of the ear, and the fundamental concepts of optical coherence tomography. A literature review is provided that describes the use of a technique related to optical coherence tomography called laser Doppler vibrometry, and how anatomical and functional optical coherence tomography has previously been used in the ear. Finally, this chapter describes the format of the main body of this thesis.

1.1 Motivation

To provide context to the reader for the research conducted, this section describes the typical pathway for cases of middle ear disease in otology, in non-technical terms and without reference to the literature, to illustrate where otology harbours challenges ripe for solving. It represents, largely, how I have come to understand the clinical practices in otology after 6 years of study.

Otologists have a remarkable ability to restore hearing in patients with conductive hearing loss (CHL) through careful decision making about surgical intervention versus conservative treatment (i.e. hearing aids) and with tremendous skill in the operating room (OR). One can, notionally, measure the effectiveness of an otologist by the combined effect of these parts; their ability to make good decisions and their ability to execute. But because the decision making must always precede the execution, the fidelity of the diagnostic tools made available to even the most skillful otologist can become the limiting factor in overall effectiveness. It's really those questions surrounding the decision to proceed to surgery or not that are the most relevant to

this work. Consider the common sequence of activities that contribute to the otologist or otolaryngologist's (ENT) decision making:

1. First, a patient receives subjective audiometric testing to determine their hearing acuity by testing for their conscious recognition of acoustic input. This typically includes tuning fork tests, pure tone audiometry, and speech recognition testing. The results from this testing have the most relevance to the patient's quality of life, as it effectively determines the degree of hearing loss, and the fraction of the hearing loss that is conductive in nature and that can plausibly be corrected by surgical intervention. Already the first decision is made when the clinician contemplates, "Is this affecting the patient's life enough to warrant the risks associated with surgery?"

2. Next, the patient receives objective audiometric testing, which are types of functional diagnostic tests to quantify the behaviour of parts of the hearing system. Of these, by far the most broadly applied is immittance testing, and by far the most broadly applied form of immittance testing is tympanometry. This is a technique that does not measure hearing acuity, but instead measures the middle ear's apparent mechanical response to sound as observed from the eardrum. Tympanometric results are categorized (Types A-C, and several subtypes), but the reality is that it is not uncommon for normal hearing individuals to present as abnormal, nor is it for severe cases of CHL to present as normal. It is only in certain cases that the results are convincingly indicative of the underlying cause. The clinician now begins to asks themself, "Is this starting to look like anything I'm confident I can fix in surgery?"

3. What follows is examination of the ear under optical magnification. Otoscopes, otoendoscopes and surgical microscopes are all commonly used, but each serve to enable detection of visible abnormalities and defects of the ear. It is here that the anatomical configuration of the ear starts to make things challenging, as only the external ear canal and the eardrum are directly visible in the clinic, and the middle ear is only partially visible through the translucent eardrum. Obvious features like thinning, perforations, retractions and inclusions of the eardrum can be readily detected, but the middle ear remains obscured from view as it

lies behind the eardrum itself. Again, it is not uncommon for individuals with apparently extensive middle ear pathology (e.g. in cases of traumatic head injury) to have inexplicable hearing acuity, nor is it for severe cases of CHL to appear normal under microscopy. The clinician's internal question remains the same, "Is this still consistent with anything I'm confident I can fix?", and perhaps, "Is this best left undisturbed?"

4. The next portion of the decision making process relies heavily on the clinician's experience and tendencies, as well as the patient's willingness to consider surgery. With the standard battery of tests already applied, select diagnostic tests may be performed or ordered to support the most likely scenarios. Computed Tomography (CT) and Magnetic Resonance Imaging (MRI) are selectively applied where it is warranted to enable visualization behind the eardrum, but the small scale of the middle ear anatomy often leaves residual uncertainty about the state of the ear. In the case of CT, there is also reluctance to irradiate the patient. It amounts to a case-by-case, tailored information gathering exercise intended to support the clinician's most strongly suspected scenario. At this stage, it is not uncommon for the clinian's internal question to become, "Is there sufficient evidence to support the surgical intervention I'd like to propose to the patient?"

5. If the clinician is convinced that the potential benefits outweigh the risks of proceeding to surgery, and the patient can be adequately counseled on all possible outcomes, which is often challenging given residual uncertainties, it is very common for a surgical plan to consist of, first, exploratory tympanotomy, with the intent to confirm the presumptive-diagnosis before proceeding with an intervention. It is not uncommon for the exploration to reveal unexpected pathology that alters the intended surgical plan. In these cases, the treatment of the unforeseen pathology may need to be aborted due to lack of consent, and foreseen but unexpected pathologies requiring more difficult procedures can severely impact the course of an OR's schedule.

This decision making process is, very often, not straight forward. What motivates the research presented herein is the residual uncertainty about what will be

encountered in surgery; a better understanding of the balance of risk and benefit to patients with middle ear disease of unknown causes; the ability of the clinician to effectively counsel patients in obtaining informed consent; and the desire for better decision making that leads to better overall otologist-effectiveness. No diagnostic tool is a replacement for the years of study, practice, and experience that are applied in middle ear surgery. But in short, the motivation for this work is to take a step towards having hearing outcomes and patient quality-of-life be limited by otologist-skill and ability-to-execute, rather than difficulties in decision making. While this research does not quantitatively address each of these motivators, they remain the rationale for my pursuit of better diagnostics in the middle ear.

1.2 Background

1.2.1 Anatomy and Physiology of the Ear

Human hearing allows one to detect and interpret pressure variations in the local area over a frequency range from 20Hz − 20kHz. Pressure presented at the external pinna drives air into the external ear canal, $\approx$ 3cm in length, where the sound energy propagates towards the tympanic membrane (TM, or eardrum): a thin, skin-like membrane, $<$ 1cm in major diameter and $\approx$ 100μm to 280μmin thickness [7], and that separates the external canal from the middle ear space. It serves to efficiently couple sound energy in the air to the ossicles, which are a small, suspended chain of three interconnected bones named the malleus, incus and stapes. They comprise a complex transmission path for the mechanical propagation of sound energy towards the fluid-filled cochlea in the inner ear. There, transduction into electrical nerve impulses occurs and sensory reception begins, but this inner-ear action isn't of particular relevance to this research.

The ossicles and the middle ear space are the anatomical features of most relevance to this work. A peculiar feature of the middle ear volume, approximately $\approx$ 2cm^3, is that it is air-filled and aerated by the eustachian tube, which intermittently opens to equalize the middle ear to atmospheric pressure via the nose and mouth. Sound pressure in the ear canal creates a differential pressure across the TM, driving it into vibration. This vibration drives the malleus, which drives the incus, and it, in turn,

drives the stapes.

For this work, it is helpful to consider the information contained in sound to be carried by a propagating pressure wave in the local atmospheric air. The accepted explanation for the seemingly complex arrangement of the ossicles is that, in response to pressure presented at the TM, passive pressure amplification occurs by lever-action of the malleus and incus, and by the area ratio of the TM and the footplate of the stapes, $\approx 2.5\text{mm} \times 1\text{mm}$ [1]. With the exception of the stapedius reflex, which stiffens the ossicular chain in response to high-pressure acoustic stimulus to protect the inner ear from exposure, hearing physiologists and clinical otologists generally think of the middle ear as a linear system of mechanical links and joints, and that its function is to manipulate forces and displacement for the best possible energy transfer to the inner ear. Effectively, it is an acoustic impedance matching network between the air and inner-ear fluid.

Additional anatomical structures referenced in this manuscript, and brief descriptions of their physiological functions, are identified in Figure 1.1, modified from [1], and in Table 1.1.

1.2.2 Conductive Hearing Loss: Causes and Interventions

Virtually all pathologies of the middle ear have the potential to cause CHL to some degree, collectively affecting hundreds of millions of individuals worldwide [8]. As the name implies, CHL refers to an increase in an individual's hearing threshold due to improper sound conduction through the middle ear. This is in contrast to sensorineural hearing loss (SNHL) which is due to poor electrical transduction or transmission from the cochlea to the brain [1]. CHL is preferable to SNHL because surgical intervention has the potential to restore hearing. Specific causes of conductive hearing loss and surgical procedures relevant to this work are described in the sections below.

Fixation of the Stapes

Stapes fixation is, typically, a progressive cause of CHL that can be caused by otosclerosis, where abnormal bony plaque forms around the footplate of the stapes; by chronic otitis media (meaning "inflammation of the middle ear "); or by congenital

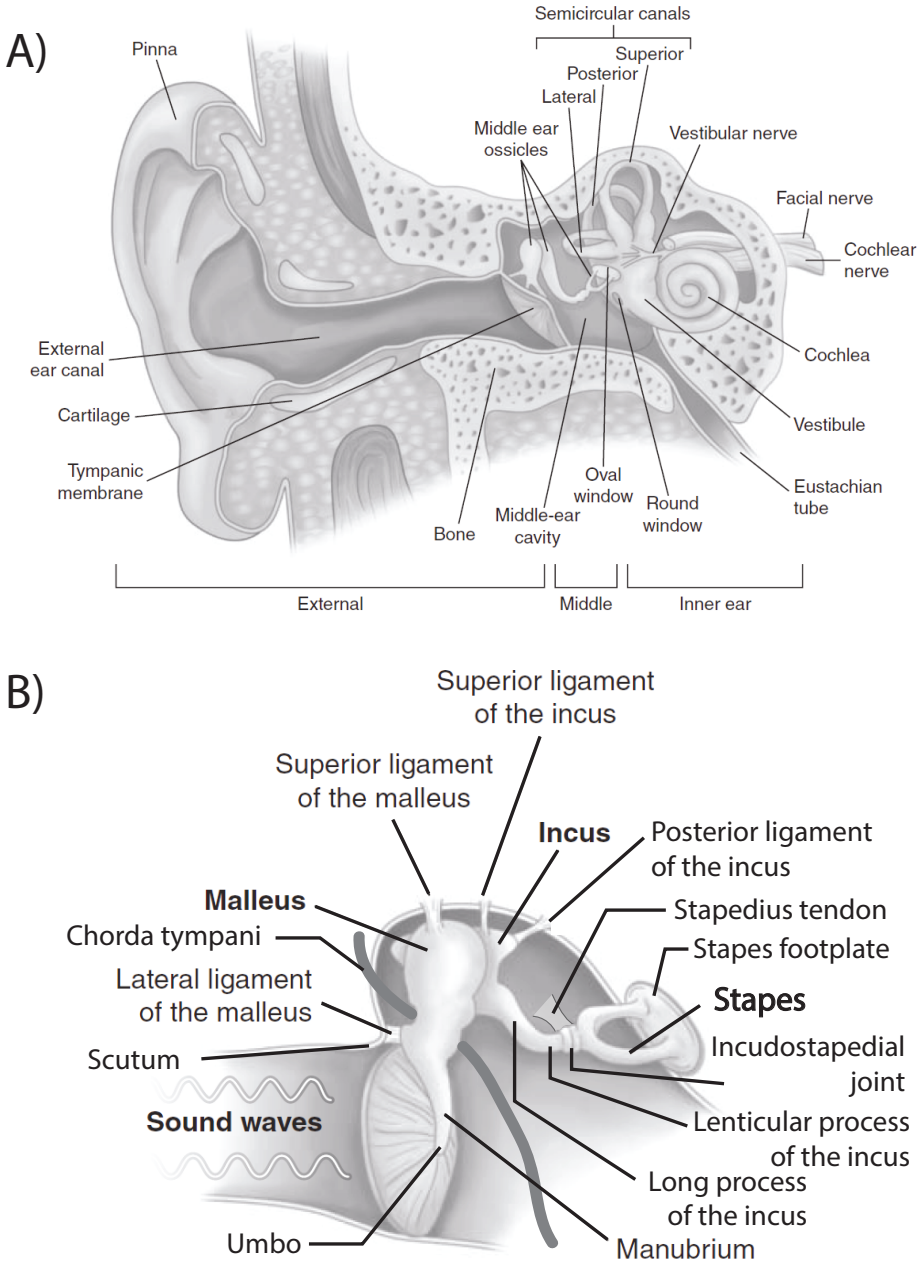

Figure 1.1: Human hearing anatomy. A, showing the external and inner ears, and the middle ear, which is the anatomical region of most relevance to this work. B, detailed view of the middle ear and its specific anatomical structures relevant to this work (taken and modified with permission from [1]).

Table 1.1: Additional anatomical structures in the middle ear referenced in this work, and brief descriptions of their physiological roles in hearing

Stucture	Function
Oval Window	Receives mechanical input to the cochlea from the stapes footplate
Round Window	Relieves pressure for the fluid displaced into the cochlea from the oval window
Chorda Tympani	Branch of facial nerve running precariously through the middle ear space between the malleus and the incus, involved in the sensation of taste
Scutum	Sharp, bony spur between the superior wall of the external ear canal and the lateral wall of the middle ear
Umbo	Functional "center" of the tympanic membrane and mechanical input to the ossicles, located at the inferior tip of the manubrium
Manubirum	Inferior projecting "handle" of the malleus, embedded in the tympanic membrane
Long process of the incus	Inferior projecting segment from the body of the incus
Lenticular process of the incus	Short protrusion from the long process of the incus that couples to the head of the stapes
Incudostapedial joint	Synovial joint between the incus and the stapes
Stapes footplate	Forces sound-driven fluid in/out of the oval window
Stapedius Tendon	Couples the stapes to the stapedius muscle for activation of stapedius reflex
Semicircular canals	Part of the fluid filled inner ear that participates in balance

ossicular malformation. Regardless of etiology, fixation at the footplate alters the mechanics of the middle ear system by increased stiffening that impedes energy transfer from stapes to the cochlear fluid.

The favored surgical intervention for stapes fixation is stapedotomy, if possible. This involves separation of the incudostapedial joint, down-fracturing the stapes superstructure, and the creation of a small burr hole through the stapes footplate. A stapes piston prosthesis is crimped around the long process of the incus and inserted through the burr hole into the oval window to complete the sound transmission path. Situations where stapedotomy is not possible require stapedectomy where the entire stapes is removed and replaced by a piston. In surgery, current practice requires that stapes fixation be confirmed before proceeding with prosthesis placement by palpation of the malleus, and observing excessive flexure at the incudostapedial joint.

Erosion of the Long Process of the Incus

A commonly encountered cause of CHL is erosion of the long process of the incus, resulting in a partial or complete discontinuity of the ossicular chain. It can be caused by chronic otitis media [9], or retraction pockets adhering to the incus [10]. It is common for patients with prior stapes-piston surgeries to experience necrosis and ossicular erosion due to the pressure around the incus from the crimp site of the piston prosthesis [11]. Erosion of any of the bony structures of the ear are possible, *e.g.* due to destructive cholestatoma, but the incus is the most susceptible of the ossicles [12]. The same type of discontinuity may be present at other locations within the ossicular chain due to congeintal malformation [13].

Depending on the extent of the erosion, the surgical procedure used to restore hearing in these cases typically involves placement or replacement of a stapes piston more superiorly on what remains of the incus; placement of a malleovestibular prosthesis, *i.e.* a prosthesis linking the malleus directly to the stapes; or bridging the gap between incus and stapes using hydroxyapatite bone cement [14].

Traumatic Injury to the Ossicles

Traumatic injury to the middle ear is possible in a variety of scenarios [15] including barotrauma during over or under pressurization in the external ear canal, *e.g.* during

explosions or while scuba diving; penetrating trauma from foreign objects inserted in the ear canal, *e.g.* from Q-tip misuse; or blunt force trauma to the head, *e.g.* skull or ossicular fractures during automobile or sporting accidents. Pre-operative diagnosis in these cases can be challenging, typically involving CT imaging to attempt to detect gross abnormalities, but very often trauma is not entirely assessed without exploratory tympanotomy [15]. While ossicular dislocations are more common than fractures [16], traumatic ossicular injuries are heterogeneous, and as a result require surgical approaches that need tailoring on a case-by-case basis.

Retraction Pockets

Retraction pockets are atelectatic sections of the TM that balloon under negative middle ear pressure [17]. They often arise from eustachian tube dysfunction and chronic otitis media. The placement of tympanostomy or "ventilation" tubes in the TM for pressure equalization and fluid drainage may adequately resolve the retraction, but depending on progression, the pocket can require repair by tympanoplasty. More drastic ossicular reconstructions can be needed when there exists adhesion to the ossicles or cholesteatoma.

TM perforation and tympanoplasty

TM perforation commonly arises from chronic otitis media or traumatic injury [18]. Its impact on ossicular activation is easily understood, conceptually, as the perforation decreases the incoming sound wave's ability to generate a differential pressure across the TM and drive it into motion. However, perforation can result in a wide range in degree of CHL, and while otologists generally believe there is a relationship between the location and size of the perforation to an expected degree of CHL, there is evidence against this notion [18]. Perforations can resolve spontaneously, but grafting is commonly applied using cartilage, fascia, and perichondrium [4].

In this work, we use the term "tympanoplasty" to refer to all surgical efforts made to restore or reinforce the TM's structural integrity, or to achieve air/water tightness of the ear canal.

Partial Ossicular Reconstruction Prosthesis

There are many scenarios that require more extensive repairs to the osscicular chain. Combinations of the same scenarios that can lead to stapes fixation or erosion of the incus can also produce greater destruction in the middle ear. A common class of surgical repairs is called "partial ossicular replacement prosthesis" (PORP), in which the malleus and incus are replaced by an implant that directly links the TM to the stapes. This is in contrast to a "total" replacement (TORP), wherein all three ossicles are replaced by a single implant from the TM directly to the oval window.

In this work, we use the term "ossiculoplasty" to collectively refer to all surgical efforts to reconstruct the ossicular chain and restore an effective sound transmission path for treating CHL.

Superior Semicircular Canal Dehiscence

Semicircular canal dehiscence (SCD) refers to an abnormal presence of an opening in the bony labyrinth encapsulating the semicircular canals of the inner ear, typically appearing between the superior canal and the intracranial space (*i.e.* the cavity housing the brain). This results in a "third window" effect that allows stapes footplate driven fluid, intended to flow between the oval and round windows, to flow into the semicircular canals. This leads to issues with balance, sometimes that can be sound-induced. While it is not directly a pathology of the middle ear, it can present as CHL due to its altering of the dynamics of the ossicles' loading by the cochlea [19–21].

1.2.3 Diagnostics in Conductive Hearing Loss

Pure-tone audiometry (*i.e.* standard hearing tests), typically administered by an audiologist, is a type of subjective audiometric testing that can accurately distinguish and separate the components of CHL from SNHL by comparing air-conducted hearing thresholds to bone-conducted thresholds across the diagnostic frequency range (100Hz to 8kHz). The measured difference in hearing acuity when bypassing the middle ear and directly vibrating the bony mastoid of the skull that houses the cochlea, referred to as the air-bone-gap (ABG), is widely used and accepted for quantifying CHL [1]. However, the differential diagnosis of CHL-causing pathologies remains

difficult because of the inaccessibility and small size of structures in the middle ear.

There are sometimes features apparent in the audiogram indicative of certain pathologies. The most noteworthy example of these is the widely recognized elevated bone conduction threshold around 2kHz called "Carhart's Notch" [1]. This is used as an indicator for stapes fixation despite evidence that it is a poor predictor, since there are no significant differences between cases of stapes fixation, incudostapedial joint detachment, or malleus and incus fixation [22].

Objective audiometric tests (*i.e.* tests that do not rely on the subjective experience of the patient) serve to provide additional information about functional response. Tympanometry is universally applied alongside audiometry as a test to probe the mechanical response of the middle ear. In the standard version of this test, a 226Hz tone is driven into the ear while the static pressure in the external ear canal (i.e. on the lateral side of the TM) is swept from -400daPa to +300daPa relative to atmospheric. By monitoring the 226Hz pressure developed in the external ear canal, the technique is able to quantify the static pressure in the middle ear (i.e. on the medial side of the TM), and quantify the overall freedom of the coupled TM and ossicles to respond to sound in terms of an *acoustic admittance* versus static pressure. Admittance is the ratio of volume velocity of air in the ear canal to driving pressure. An extension to standard tympanometry, called "wideband reflectance" [23], operates in a similar mode but characterizes mechanical response against swept stimulus frequency and reports results in equivalent conventional network-theory terms of *power absorbance* and *reflectance* vs frequency (rather than static pressure). Despite the wide use of tympanometry and growing use of wideband reflectance, there is evidence that these techniques correlate poorly with CHL. In [24], the signatures for middle ear pathologies in wideband reflectance could only be studied by measuring changes within individual temporal bones after simulating pathlogies, since the normal range between individuals is too wide, and the same problem was noted in [25]. In [26], 10 of 11 ears with fixed stapes, 5 of 6 with ossicular discontinuity and all 11 ears with SCD had normal tympanograms. This insensitivity is likely because the measured response is dominated by the compliance of the TM, and not the ossicles [27]. In the case of tympanometry, unless results are very strongly indicative of a fluid filled ear (*i.e.* type B, "dead flat tymp") or of ossicular discontinuity (*i.e.* type A_D, "high peaked

tymp"), tympanometric findings are often disregarded if they are not consistent with the overall clinical narrative [28], and so the clinician's experience is heavily relied upon to weigh its relevance in decision making.

No conventional radiological imaging technology (*i.e.* magnetic resonance imaging, MRI, computed tomography, CT, or ultrasonography, US) provides a comprehensive diagnostic picture of the middle ear state, *in vivo*. CT, and to a lesser extent MRI, are used in otology for imaging the temporal bone, particularly in cases of middle ear trauma, cholesteatoma detection, attempts at pre-surgical confirmation of otosclerotic foci, and attempts at pre-surgical confirmation of semi-circular-canal-dehiscence. Regional differences and clinician preference greatly impact how often it is used. This is not surprising as the available imaging modalities are costly, require referral, act to slow patient throughput, may expose the patient to ionizing radiation, and often do not add significant clarity.

Take, as a single example, otosclerotic stapes fixation. CT imaging is sometimes applied to confirm the presence of plaque formation around the footplate before taking a patient to the OR. Unfortunately, the reality is that often no plaque formation is apparent even under direct microscopy in the OR following opening of the TM and curettage of the bony scutum to reveal the footplate. In such cases, the surgeon could still manually confirm stapes fixation (*i.e.* even in the complete absence of obvious plaque) via palpation. This case captures a very common sequence of events that occurs in otology where the surgery intended to restore hearing is scheduled as an "exploratory tympanotomy" with an intended restorative procedure to follow once a differential diagnosis is made intraoperatively. CT has two key limitations in the middle ear. Relative to the anatomical scale of the TM thickness and the ossicles, the resolution of a typical CT scan, even when configured for the best possible resolution, at $\approx 333\mu$m (see Appendix A), is simply too poor to adequately resolve many of the miniscule features of the middle ear. CT also contains no functional information about the middle ear's mechanical response to sound. Figure 1.2 shows the scale of the ossicles and how they are resolved in a conventional high-resolution CT image of the temporal bone. Even during acoustic activation of the middle ear at sound pressure levels approaching the threshold of pain, the amplitudes of vibration are only the order $10-100$nm, $\approx 1000\times$ too small for CT to resolve, and occur over timescales

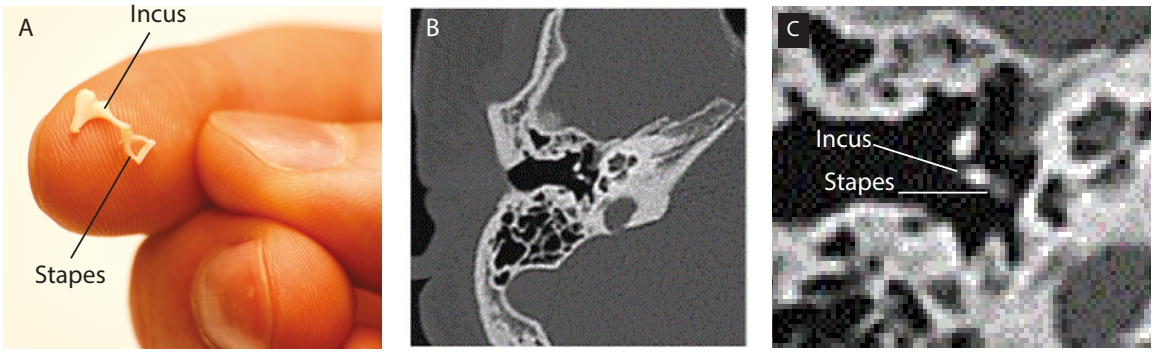

Figure 1.2: Resolution in CT. A, Magnified depiction of the incus and stapes. B, Example of the ossicles as imaged by high-resolution CT (taken from [2] with permission). C, Magnification of B to approximately the same scale as A to illustrate the resolution limitation of CT in otology

of 10ms to 100μs, $\approx 1000\times$ too fast for CT to directly sample. These limitations are the underlying reason why exploratory tympanotomy with direct optical microscopy using surgical microscopes or otoendoscopes is the current standard of care in otology. It is worth noting that, even with optical resolution, conventional microscopy in the OR remains unable to detect the nanometer scale, sound-induced vibrations of the ossicles.

1.2.4 Optical Coherence Tomography

Optical coherence tomography (OCT) is a rapidly developing interferometric imaging technique that produces depth resolved imaging of scattering biological samples using near-infrared (NIR) light, typically using wavelengths between 800 and 1700 nm [29]. Often thought of as an optical analog to ultrasonic imaging, the technique has the potential to generate extremely high resolution cross-sectional images of scattering tissue. Typical axial and lateral resolutions achieved in OCT are on the order of $\approx 10\mu$m, but sub-micron resolutions have been demonstrated [30].

There are three main topologies that are used in OCT, two of which are relevant to this research. Time-Domain OCT (TD-OCT) was the topology presented in the original article in 1991 [31]. In TD-OCT, a spatially coherent light source with low temporal coherence (*i.e.* a broadband light source like a super-luminescent diode,

SLD) is split into a reference beam (*i.e.* a stored copy of the light), and a sample-probing beam that is used to interrogate the sample's structure. Back-scattered light from sub-surface structures in the sample is collected and interfered (*i.e.* overlapped) with the reference beam on a photodetector. The sample beam is typically focused to a small spot size to provide lateral resolution (*i.e.* so that any measured interference arises from back-scattering structures located within the small cross-section of the beam). Since in low-coherence interferometry, interference fringe visibility is only high when the temporal delay between the two interfering beams is less than the source's coherence time, τ_c, or equivalently, when the relative path-length difference is less than the source's coherence length, z_c, a depth-reflectivity-profile of the sample can be obtained by variably delaying the light in the reference arm in time and measuring the generated interference fringes. Both τ_c and z_c are measures of the light's randomness-in-time, and are related by $z_c = \tau_c c$, where c is the speed of light. The conceptually simplest way of achieving variable delay is by folding back the reference beam with a sliding mirror as shown in Figure 1.3. It's the light source's low temporal coherence that provides *coherence gating* around the depth of equal delay between the two arms of the interferometer and that generates axial resolution in the measurement. The envelope of the interference pattern collected in time as the reference arm is variably delayed gives the reflection profile of the sample along the sample beam's axis, and is called an A-line, although in this work an A-line may also refer to an average of several individually measured A-lines. By raster scanning the beam across the sample, a 2D cross-sectional brightness-mode image (B-Mode) can be constructed from the stacked A-lines. Similarly, a 3D volumetric image can be constructed from stacked B-Mode images.

TD-OCT has the advantage of being simple and being able to provide long-range scanning since all that must be done to achieve greater axial ranging distance, z_D, is to increase the maximum delay introduced in the reference arm. TD-OCT fell out of favour because it necessitates moving-parts to generate adequate optical for most practical scenarios, and the required opto-mechanics are often bulky and tend to inertially limit achievable imaging speed.

Spectral-Domain OCT (SD-OCT) replaced TD-OCT because of an inherent sensitivity advantage that is well understood [32, 33]. In SD-OCT, instead of variably

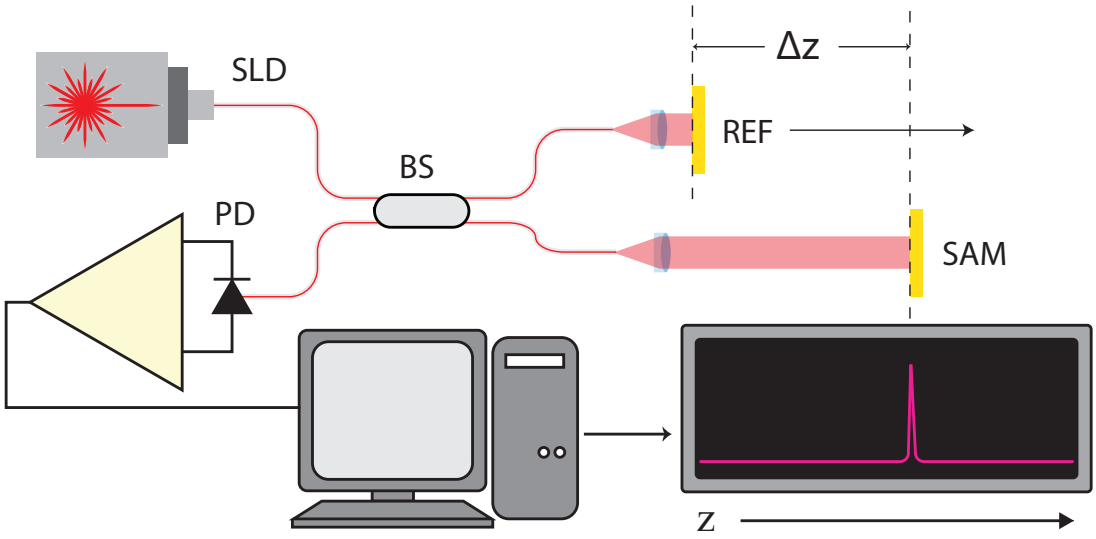

Figure 1.3: Basic Configuration of a TD-OCT system, illustrating the conceptual foundation for low-coherence interferometry with a variable length reference arm. **SLD** superluminescent diode, **BS** beam splitter, **PD** photo-detector, **REF** reference arm of interferometer, **SAM** sample arm of interferometer, $\boldsymbol{\Delta z}$ relative path length difference between reference and sample arms, **z** depth axis of the measurement referenced to the relative path length difference.

delaying the reference beam as in TD-OCT, the reference path remains fixed in length, and the light detector is replaced by a spectrometer that measures a spectral interferogram. Effectively, each sample in the spectrum measures the interference occurring at a single wavelength in the optical bandwidth of the light source. After re-sampling the collected interferogram to obtain linearly-spaced samples in optical frequency, taking a discrete-Fourier transform (DFT) of the collected spectral interferogram produces a complex A-line. SD-OCT is conventionally implemented using a CCD-based spectrometer, where imaging speed is usually limited by the read-out speed of the sensor, which can easily produce A-line rates ≈ 10 to $100\times$ faster than TD-OCT. However, because of the Fourier relationship between the sampled spectral interferogram and the desired A-line, SD-OCT is more susceptible to and affected by image artifacts arising from non-linearities in the system [34]. SD-OCT is not used in this work, but is in the related literature.

A related technique that is used in this work is Swept-Source OCT (SS-OCT, collectively with SD-OCT referred to as Fourier-Domain OCT, FD-OCT). It combines attractive features of both TD-OCT and SD-OCT by benefiting from the same sensitivity advantage as SD-OCT while avoiding the need for a complex spectrometer detector. Instead, the spectral interferogram in SS-OCT is measured by sweeping the optical frequency of a narrow-band source over an optical bandwidth equivalent to the broadband light sources used in TD-OCT or SD-OCT. The spectral interferograms are then detected serially on a photodetector and sampled in time before applying the DFT to get a complex A-line. The simplicity in detection in SS-OCT is a key advantage over the CCD detectors used in SD-OCT, since CCDs can't be made to use balanced detection and so their susceptibility to relative intensity noise is worse. The same susceptibility to artifacts in SD-OCT also exists in SS-OCT.

In FD-OCT topologies, the maximum axial ranging distance, z_D, is limited by the optical frequency resolution in the measurement of the spectral interferogram, and is determined by the relationship $z_D = \pi/2\delta k n_r$, where n_r is the local index of refraction in the sample, and δk is the optical frequency sampling resolution in wavenumbers [35]. In SD-OCT, the spectral measurement is made on a line-scan camera onto which the entire spectral width, Δk, must fit, and which has a finite number of pixels (typically ≤ 2048, although there is a trade-off between speed and density). Since

axial resolution is linked to overall spectral width via $\delta z = {}^{\pi}/_{\Delta k n_r}$ [35], there's a built-in trade-off between axial resolution and ranging. Since in SS-OCT, the spectral measurement is made serially in time on a simple detector and because very high speed sampling can be used to densely sample the spectral interferogram, the maximum achievable ranging distance is usually limited by the instantaneous coherence length of the source, z_c, *i.e.* the greatest path length difference over which interference will strongly occur between the reference and sample beams. For a light source with a Gaussian spectral shape, its coherence length is related to its instantaneous linewidth by:

$$z_c = \frac{2 \ln 2}{n_r \pi} \frac{\lambda_0^2}{\delta \lambda} \tag{1.1}$$

Where λ_0 is the instantaneous central wavelength, $\delta\lambda$ is the instantaneous line width around λ_0, and n_r is the local index of refraction [36]. With swept sources of conventional designs, this *unwanted* coherence gating has placed an upper limit on how large z_D can be made before measurement sensitivity rolls off in SS-OCT [37]. Additionally, poor sweep-to-sweep repeatability has historically lead to instability in the measured interferograms even with stationary samples [37]. In general, the history and advances in swept-laser development that pertain to OCT are well described in [37]. Appendix B contains an explanation of the importance of coherence length in long-range SS-OCT.

1.3 Literature Review

This section comprises a comprehensive review of the application of OCT and optical vibrometry to the ear, focusing on the human middle ear.

1.3.1 Laser Doppler Vibrometry

Laser Doppler Vibrometry (or velocimetry, LDV) is an interferometric technique that detects nano-scale displacements and velocities of optically scattering media. The area of LDV and its application to the ear is quite wide reaching, as it is itself a well-suited technique for quantifying the ear's physiological vibration response to sound. It works by measuring the phase shift imparted to a beam of spatially and temporally coherent

light that is back-scattered from a structure in motion using an interferometer. It does this at a single wavelength, unlike in SS-OCT where measurements are made at multiple wavelengths. If applied carefully, the amplitude and phase of sound induced vibrations can be quantified in biological samples, including the structures of the middle and inner ears. Additional background theory regarding the inner workings of LDV systems can been found in [38]. The LDV literature's relevance to this work lies in its demonstration of sensitivity to hearing physiology and pathology, the careful investigations of its potential clinical utility, and how it collectively provides several decades of rationale for the further development of optical vibrometry for otology.

LDV in the ear is best understood by, again, considering the middle ear as a linear impedance transformer between the airborne acoustic pressure-wave arriving at the TM and the fluid-loaded input to the cochlea in the inner ear. This vibrational behaviour is commonly described in terms of a *middle ear transfer function*, *e.g.* in [3, 39–41], and is typically expressed in terms of the frequency dependent ratio of velocity or displacement to the driving pressure at the TM at particular structures of interest, *e.g.* at the umbo or footplate of the stapes. Both the vibration amplitudes and the relative phases of motion of structures in the ear are studied and are of physiological interest, however results pointing towards LDV's diagnostic capabilities mainly rely on amplitude characteristics, and typically only at lower frequencies due to the observed increase in complexity of vibrational modes at higher frequencies [42–45].

Unfortunately, LDV has significant limitations in that it has no ability to resolve depth (*i.e.* no cross-sectional imaging is possible), and it does not conventionally provide depth gating of any practical use for biological samples. Effectively, only the vibration of the brightest scattering structure along the beam is captured by the LDV measurement. In the middle ear, this means one can only measure vibration at the TM, except in cases of perforation or during surgery. This severely limits the potential for clinical translation of much of the LDV research to a practical diagnostic tool. Experiments performed in prepared cadaver temporal bones to expose the ossicles either down the external ear canal with the TM removed (*i.e* transcanal) or through a mastoid approach (*i.e.* transmastoid) do not easily map to live patients. The literature involving *in vivo* intra-operative LDV measurements remains interesting and provides insight into relevant middle ear mechanics that could be probed by

OCT [45–51], and if nothing else, further illustrates the severity of the limitations of LDV's lack of depth resolution.

It's the reports of transcanal LDV measurements in a clinical or research lab setting (*i.e.* not in an operating room) with the TM and middle ear cavity intact and undisturbed that are of particular relevance to this work. Despite its limitations and inability to directly probe the ossicles without surgery, LDV's application in middle ear research and CHL is a natural one. While it has seen widespread use in bench-top experiments, its use in live humans has been surprisingly limited. In these cases measurements can be performed over the surface of the TM whenever the ear canal accommodates the required line of sight, limiting the set of accessible ossicular features to the manubrium and the umbo.

The mechanical behaviour at the exposed surface of the intact TM was first investigated with transcanal LDV by Goode et al. [52] and Stasche et al. [53]. From a clinical translation point of view, the most compelling works involve measurements of velocity along the manubrium of the malleus. More specifically, measurements are most commonly taken at the umbo, where the greatest amplitude mallear displacements occur. This location is commonly considered the *input* to the middle ear system and is thought to best represent the overall activation of the ossicular chain. It is also conveniently easy to locate and identify in most individuals as it is approximately at the apex of the TM's conical shape. The basic arrangement used in this type of measurement is shown in Figure 1.4, taken from [3].

Whittemore et al. [54] were able to establish the normal range of umbo velocity, and also to show that individuals with pure sensorineural hearing losses do not differ in umbo velocity from normals, implying that significant deviation from normal umbo vibration should be attributable to abnormalities of the middle ear, making LDV promising as a diagnostic tool for CHL (and by extension, optical vibrometry in general). Another interesting result of that work showed that non-zero static middle ear pressure produces significant variability in umbo velocity, suggesting aerated ears should produce more repeatable LDV results than those with eustachian tube dysfunction or static pressure differentials across the TM. Finally, it was demonstrated that the acoustic reflex did not produce significant effects on the measured umbo velocities, and that good long term repeatability existed in the measurements

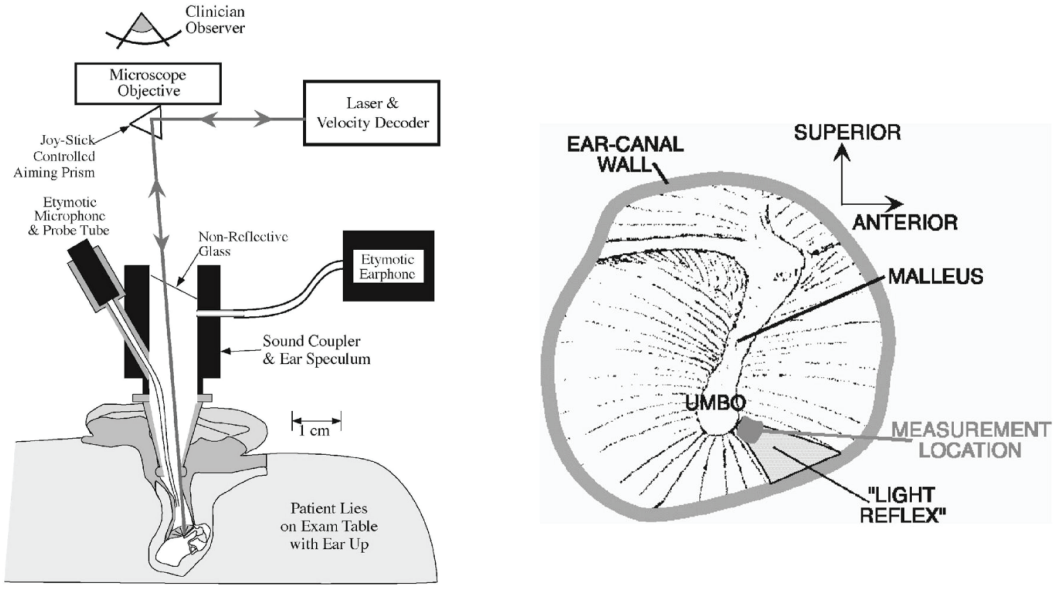

Figure 1.4: Typical configuration used in the literature for non-invasive LDV measurements down the ear canal, *in vivo*. A, A typical experimental setup with a sound source and microphone, and an open port to couple the LDV into the external canal. B, A sketch of the TM and the most common site of velocity measurement at the umbo (taken from [3] with permission).

performed, all supporting the notion of clinical utility for optical vibrometry in the middle ear.

A complementary set of experiments by Rosowski et al. [3, 55, 56] directly examined whether particular middle ear pathologies produced significant differences from normal in measured umbo velocities. Not surprisingly, it was shown that mallear fixation produced hypo-mobility due to increased stiffening of the ossicle being interrogated, and ossicular interruptions (discontinuities of the ossicular chain) produced hyper-mobility due to the uncoupling of the acoustically stiff cochlea from the chain. Particularly interesting, and of practical relevance to this work, is the fact that measured umbo velocity remains relatively unaffected by stapes fixation. Since the stapes fixation occurs at the opposite end of the ossicular chain, it is not surprising that it is not tightly coupled to umbo velocity. As a result, it was suggested that CHL due to stapes-fixation should have a signature of nearly-normal umbo velocty (i.e. ruling out mallear fixation and ossicular interruption), accompanied by significant ABG. This is notably similar to the way stapes fixation is diagnosed in-clinic, with a signature

of significant ABG in audiometry and with no convincing evidence for any other of the common CHL pathologies.

Rosowski followed this work in 2012 [26] with an attempt to determine if combining LDV with information from immittance testing could help to deduce more information about the state of the ear, and further supported that good pathology identification could be achieved with combined audiometry and umbo LDV. Rosowski's work [3,21] also highlights the potential to discriminate stapes fixation from SCD, by measuring slight hyper-mobility at the umbo, and inferring significant hyper-mobility at the stapes arising from the third-window effect (as well as hypersensitivity to bone conduction). In practice, SCD always needs confirmation on CT before proceeding to surgery.

In parallel, and in fact even prior to some of Rosowski's *in vivo* LDV work, Huber et al. carried out independent work with very similar goals and results [57]. Despite positive agreement with some cadaver experiments and negative agreement with others in terms of absolute response levels, the key conclusions support the notion that pathological deviations from normal middle ear vibration are more significant the closer the measured target is located to the site of the disease, and that mallear fixations and ossicular interruptions are readily distinguishable at the umbo, while stapes fixations produce more subtle effects. This is further supported by the reported compliance of the ossicular chain determined in cadaver experiments [58].

Despite the substantial evidence of clinical utility, widespread adoption of LDV has never happened. One contributing reason is that transcanal LDV measurements remain problematically challenging to carry out *in vivo*. Authors have noted the requirement for great skill on the part of the operator [26], requiring patience and practice. These are two obvious deterrents from clinical adoption. Rosowski also noted in [59] that their umbo velocity measurements required two trained operators to carry out. It would appear that LDV has simply not yet been engineered into the right device to achieve adoption. Polytec, who appear to have a dominant presence in middle ear vibrometry research, do not have a commercially available FDA cleared device [26], relegating its use to research labs.

Collectively, the LDV literature strongly supports the notion that optical vibrometry applied in the clinic can not only provide strong evidence for making differential

diagnoses of CHL causing diseases, but also suggests that even better clinical utility could be provided by an optical vibrometry technique like OCT that can probe beyond the TM and quantify vibration nearer to the sites of pathology, deeper in the middle ear. Furthermore, for an optical vibrometry device to become relevant to otology, there exists a clear need for the device to be well-suited to *in vivo* imaging. This implies a device that can not only obtain vibration measurements, but that has good ergonomics, can handle high patient throughput, that can provide real-time feedback, that is easy to align, and that can be operated by a single user in a clinical setting.

1.3.2 Anatomical OCT in the Middle Ear

The high optical resolution and ability to penetrate membranous tissue like the TM and round window for imaging makes OCT a very attractive imaging modality for otology, and is well-suited for clinical translation based on its non-contact nature, its non-invasiveness, and its lack of ionizing radiation. Feasibility studies for the application of OCT to the ear were first published by Pitris *et al.*, where cadaveric temporal bones were imaged transtympanically using a TD-OCT system of typical design for the time [60]. Their qualitative assessment of the resulting images eventually sparked research in several directions including inner ear imaging to study cochlear dynamics and physiology, limited to animals and cadavers [61–67]; intrasurgical OCT of the ear [68–70]; and tympanic membrane imaging, with specific focus on thickness measurements [71–74], the detection of biofilm on the medial surface of the membrane for the characterization of otitis media [75–80], and for the characterization of middle ear effusions [81, 82].

A commonality among much of the published literature is the use of OCT engines that are intended for use in highly scattering media, and where axial ranging of just $2 - 3$mm is all that is needed. Also, the optics that have been used for scanning the OCT sample beam have not been tailored to accommodate the human ear's anatomy. This has effectively resulted in images that do not capture the full depth or full width of the TM or middle ear space accessible from the external ear canal (a volume of interest of VOI $\approx 10\text{mm} \times 10\text{mm} \times 10\text{mm} = 1\text{cm}^3$). In this respect, a very relevant sub-field of OCT for anatomical imaging of the ear relates to the practical challenge

of light delivery to the ear and the design of suitable imaging probes. The ear's inconvenient location at the end of the variably narrow and curved ear canal makes the collection of data in live subjects technically challenging. This is very much the same problem described in Section 1.3.1 that evidently limited the adoption of LDV as a clinical tool. While cadaver studies benefit from drilling away of the bony ear canal to provide optical access on the benchtop, the recent progression to live-animal and live-patient imaging has come with varied approaches including bolt-on-OCT to surgical microscopes or similar form-factor contraptions [83, 84], the development of miniature, minimally invasive endoscopes [85, 86], and hand-held pistol grip or otoscope-like devices [73, 77, 82, 87, 88].

1.3.3 Optical Coherence Tomography Doppler Vibrography

Beyond the basic anatomical imaging capabilities described in Section 1.2.4, OCT also has the potential to provide functional information about the ear's vibrational response to sound. In a fashion very similar to that of LDV, moving structures in samples being probed by OCT introduce Doppler shifts to the detected light, appearing as relative phase shifts between OCT A-lines collected in time. The key difference to LDV in OCT based velocimetry is that coherence gating (i.e. the use of broadband illumination instead of narrowband) provides the additional information required to spatially reject the phase modulation generated by the bright reflectors, and isolate phase modulations arising from the movement of less strongly reflecting structures at other depths. When applied to miniscule, oscillatory displacements like those that occur in hearing physiology, the set of OCT-based velocimetry techniques is collectively referred to herein as Optical Coherence Tomography Doppler Vibrography (OCT-DV). This provision for the spatial rejection of bright reflectors like the TM makes OCT-DV an ideal tool for non-invasive functional imaging and diagnostics of the middle ear and the ossicles.

A number of variants of the OCT-DV technique have been demonstrated, explained with the greatest clarity using a vibrating phantom in [89]. In its application to mammalian hearing, OCT-DV's earlier and greater use has been for investigating inner ear and cochlear dynamics, where it was first applied in *ex vivo* studies [90–92] and then *in vivo* in animal studies [93–104], albeit with the subjects anesthetized.

OCT-DV's use in transtympanic measurements of the middle ear (*i.e.* without disturbing the TM) are at the heart of this work. Its potential to diagnose pathologies that are not evident in purely anatomical images by looking for deviations from normal functional response has long been recognized since the early OCT-DV measurements in the mouse TM [105]. Other *ex vivo* studies in non-pathological samples have been accumulating ever since, helping to describe hearing mechanics [106–109]. The simplest example of the rationale for OCT-DV's hypothetical utility in the diagnosis of middle ear pathology is as follows: in a patient suspected of having erosion of the long process of the incus, OCT-DV could reasonably be expected to detect above-normal vibration of the malleus and incus since they have been mechanically unloaded, and below-normal vibration of the stapes since it is no longer mechanically driven. By contrast, in a patient with stapes fixation, one would expect to observe reduced vibration of all three ossicles since the entire ossicular chain has been stiffened, but with the greatest reduction seen at the stapes. This rationale is very much supported by the LDV literature in Section 1.3.1, and by the limited *ex vivo* animal and human studies where OCT-DV has been applied to simulated pathologies [110–112] (and to accidentally encountered real ones! [113]).

The most closely related and exciting literature with direct relevance to this research are [84, 88], which are both very much directed at solving the practical challenges of performing high-fidelity middle ear OCT-DV measurements in live, unaltered human ears. In [88], a patient compatible, hand-held otoscope-like device was developed with integrated sound stimulus and OCT-DV capabilities. They used the prototype device for wide-field vibrography images of the TM, although oddly they did not publish images in live patients. In [84], the work demonstrated the first full TM-width vibrography in live patients, with exciting new analyses including variance imaging that is sensitive to blood flow in the TM, and the detection of distortion product otoacoustic emission (DPOAE) induced vibration at middle ear structures, which quantifies a non-linear, physiological amplification process that occurs in the inner ear, an extension to an existing objective audiometric test.

1.3.4 Otological High-Frequency Ultrasonography

A competing imaging technology, high-frequency ultrasound, has been used to generate middle ear images comparable to those obtainable with OCT, *ex vivo* [114, 115]. While US has a penetration advantage as compared to OCT, it has a significant disadvantage in that, unless there already exists a middle ear effusion, it must be filled with an acoustic coupling medium, *e.g.* saline, in order to generate useful results [116]. While not technically unfeasible for *in vivo* imaging, it is a very strong deterrent. Additionally, fluid-filling of the middle ear cavity and external ear canal completely alters the dynamics of the system and would render any functional measurements akin to Doppler Vibrography, perhaps, non-physiological.

1.4 Format of this Thesis

This thesis is divided into three key chapters and one discussion section, each of which presents significant contributions. Deeper motivations for each section of work are detailed in their respective chapters, but a brief description is given here to provide context within the overall scope of my work.

Chapter 2 - Requirements Discovery for Optical Coherence Tomography Imaging of the Human Middle Ear

There exist inherent trade-offs in the design of an OCT system: Lateral resolution, depth-of-field, signal-to-noise-ratio, and frame rate are all inter-dependent. Transtympanic imaging of the entire middle ear represents a relatively large VOI to be interrogated with OCT, particularly in the axial ranging direction. With very few reference images available in the literature, with no prior examples of systems appropriate for real-time middle ear imaging *in vivo*, and since all of the OCT system design trade-offs tend to degrade detection sensitivity in favor of other performance characteristics, it remained unclear how challenging it would be to build an OCT system that provides subjectively acceptable images of the middle ear for useful diagnostics. This component of my research aimed to determine what level of performance was needed in a clinical system by building and characterizing a long-range TD-OCT system, and imaging cadaver ear specimen in bench-top experiments to quantify engineering

requirements that, if met, will result in acceptable image quality.

Chapter 3 - The Development of a Swept-Source Optical Coherence Tomography Imaging System with Doppler-Vibrographic Sensitivity at the Ossicles, *in vivo*

This component of my research entailed designing and building a second system that provided the desired level of image fidelity at speed, and that also addresses immediate usability and ergonomic issues so that the device could be used on live patients by clinicians. Bridging this gap from controlled bench-top experiments to clinical use on volunteers is a significant undertaking, and the completed swept-source OCT design represents the first system in the literature designed from the ground up to simultaneously meet all of the imaging requirements for full human middle ear imaging by taking advantage of very recent advances in high-speed swept-laser technology. The work also produced the first published *in vivo* middle ear OCT-DV measurements in humans and addresses the substantial computational complexity of extracting the OCT-DV signal in real-time with a GPU-accelerated lock-in detection scheme.

Chapter 4 - Applying Optical Coherence Tomography Doppler Vibrography to Clinical Otology: Discriminating Stapes Fixation from Normal

With a sufficiently usable OCT-DV system available following the work of Chapter 3, I proceeded to apply it to a group of live patients, otherwise clinically diagnosed with stapes fixation, and compared them to a group of normal controls. This was done in an effort to produce the first direct evidence of OCT-DV's sensitivity to changes in middle ear dynamics arising from pathology, *in vivo*, and represents the first published results of OCT-DV being applied to a real patient population with CHL.

Discussion

Beyond each of the preceding chapters' respective discussion sections, an overall discussion section details known issues and limitations of the technology, and our continued efforts to improve it. Most excitingly, it also presents unique patient imaging

cases with analyses of imaging results that illuminate possible roles for OCT and OCT-DV in practical otology, and compelling directions for future research.

Chapter 2

Requirements Discovery for Optical Coherence Tomography Imaging of the Human Middle Ear

Dan MacDougall,[a] James Rainsbury,[b] Jeremy Brown,[a] Manohar Bance,[a,b] Robert Adamson[a]

[a] School of Biomedical Engineering, Dalhousie University, Halifax NS, Canada

[b] Division of Otolaryngology Head and Neck Surgery, Department of Surgery, Dalhousie University, Halifax NS, Canada

2.1 Author Contribution Statement

D. MacDougall and R. Adamson conceived the experiments and analyses. M. Bance and J. Rainsbury provided the rationale for clinical relevance. J. Rainsbury prepared cadaver specimens for imaging sessions. J. Rainsbury and D. MacDougall carried out imaging and measurement procedures. D. MacDougall designed, assembled, and programmed the system used for data collection; carried out analysis of the measurements; and was the lead and corresponding author on the journal submission.

2.2 Preamble

This chapter is based on my first peer reviewed publication [117]. Its contents remain, largely, unaltered. However, introductory information that would duplicate the contents of Chapter 1 have been omitted or otherwise changed for conciseness. Some additional, unpublished experimental details have been opportunistically added. Some modifications have been made to lend context and render this document, as a whole, self-consistent in terminology and style, and to better formulate the results. Specifically, the introductory section has been altered to provide better insight into the motivation and novelty for the work at the time the original manuscript was

submitted for peer review, and to explain the work's fit into the overall story of my thesis; descriptions of pathologies and surgical interventions have been reduced in detail, and the reader is directed to Section 1.2.2 for those details; discrepancies between the analysis of the optical losses theorized and measured in the TM have been rectified; and discussion points have been expanded and altered to better reflect insights that have been gleaned since the paper was published.

2.3 Abstract

Non-invasive middle ear imaging using optical coherence tomography presents some unique challenges for real-time, clinical use in humans. In this paper we present results from a 2D/3D OCT system built to assess the imaging requirements of clinical middle ear imaging, and the technical challenges associated with them. These include the need to work at a low numerical aperture, the deleterious effects of light scattering and signal attenuation in the tympanic membrane, sensitivity requirements for clinical fidelity of images at real-time rates, and the high dynamic-range requirements of the ear. We validated the system by imaging cadaveric specimens with simulated disorders to show the clinical applicability of the images. We also provide additional insight into the likely role of OCT in clinical otology.

2.4 Introduction

2.4.1 Motivation

As compared to the animal models that were being investigated with OCT at the time, human middle ears are quite large, and motion artifacts related to breathing and heartbeat can only be avoided at real-time acquisition and display speeds of $\approx$ 20FPS. Furthermore, system operators, who may be clinicians and whose time is limited, do not welcome long acquisitions times nor complicated contraptions to steady subjects. The task at hand was to assess the operating constraints surrounding how a real-world OCT system would need to be used in a practical scenario, and determine what performance requirements that places on the OCT engine at the heart of the system.

In 2012, while the use of OCT for anatomical trans-tympanic middle ear imaging

had already been demonstrated at a feasibility level in cadavers [60], those original images of the middle ear were collected at very low speed ($\approx$ 0.1 to 0.03FPS), captured a volume of only $\approx$ 5mm $\times$ 5mm $\times$ 5mm, and were of relatively poor quality. These are all major inadequacies that needed addressing before a clinical OCT system could be of any practical use for diagnostics in otology. These issues were attributable to the demonstrated system being of a TD-OCT topology, and the fact that speed was not of concern in that study. Research published as my work was commencing [113] did a better job of presenting high-fidelity anatomical images in cadavers, but were also limited in speed (0.05FPS), and even more drastically in image depth to just z_D = 3mm because it used a SD-OCT topology of conventional design (*i.e.* with penetration depth appropriate for retinal imaging). In [110], cadaver chinchilla experiments were carried out over 7mm $\times$ 7mm $\times$ 3mm, which is still insufficient to capture the entire human middle ear. While the data was acquired at an acceptable rate of $\approx$ 4FPS, the data was processed and visualized off-line.

The hope that middle ear OCT would prove useful for diagnostics was already present in the literature. We felt that the most compelling application was transtympanic OCT for better pre-operative and post-operative assessment of the middle ear's state, to either reduce the number of unnecessary ear surgeries being performed, or better inform the the surgeon about what will be encountered in the OR so that they may be best-prepared for it. For OCT to be useful in this regard, some minimum level of image fidelity would be necessary, and since no system yet proposed or demonstrated appeared to be suitable for real-time transtympanic imaging of the middle ear in live humans, it remained unclear what level performance was needed. Answering this question formed the crux of this part of my thesis work, and was the logical first step in answering the overarching question of how to make trans-tympanic OCT useful to an otologist.

2.4.2 Anatomical Constraints

The distance from the entrance of the external ear canal to the distal side of the middle ear cavity is $\approx$ 40mm and the diameter of the ear canal is typically 7mm. If the middle ear is to be imaged from outside the ear canal, then the canal geometry restricts the numerical aperture (NA) of ear imaging systems to be $<$ 0.09. Reducing NA also

reduces lateral resolution, increases depth-of-field, and importantly for imaging the middle ear, reduces light-gathering ability and therefore the achievable shot-noise-limited signal-to-noise ratio (SNR) and penetration through the TM. In a non-invasive middle ear imaging system the amount of optical power reflected from internal middle ear structures like the ossicles is further reduced by the need for the light to pass twice through the scattering tissue of the TM, thereby degrading image quality. This is clearly pointed out in [60], but not quantified. Moreover, simultaneous imaging of the relatively bright TM and the much dimmer middle ear structures requires that the imaging system have a large dynamic range (DNR, simultaneous ability to resolve dim reflections in the presence of strong ones).

From a clinical perspective, any proposed OCT system must fit well within the existing clinical work-flow, provide the clinician with obvious diagnostic advantages, and produce images at real-time frame rates. Unlike more commonplace applications of retinal and dermatological OCT, the structures of interest in the middle ear are millimeter sized and so do not require exceptionally high resolution to visualize. However, the fact that they are located behind the eardrum, the fact that they are distributed throughout approximately 1cm^3 of air-filled space and the fact that, if they are to be imaged from an external microscope, the usable NA will be very low, conspire to create a set of requirements unlike other OCT applications, and point towards the need for an application-specific system designed with imaging parameters significantly different from typical.

In the following sections, we present 2D and 3D imaging results obtained from a TD-OCT system developed specifically to assess how these anatomical constraints map to imaging requirements. While it is well known that TD-OCT suffers from, typically, inertially-limited acquisition rates and low sensitivity, it has advantages over FD-OCT in terms of simplicity, dynamic range and maximum axial ranging, in that it is unaffected by complex-phase ambiguity and spatial aliasing, and is immune to DNR limiting image artifacts [118]. Realistically, I now recognize that TD-OCT is unlikely to form the basis of any real-time clinical system due to the associated difficulties in achieving high frame rates, but TD-OCT presented an excellent vehicle for pre-clinical imaging aimed at understanding the requirements a system need meet to produce acceptable images. Additionally, at the time this study was performed,

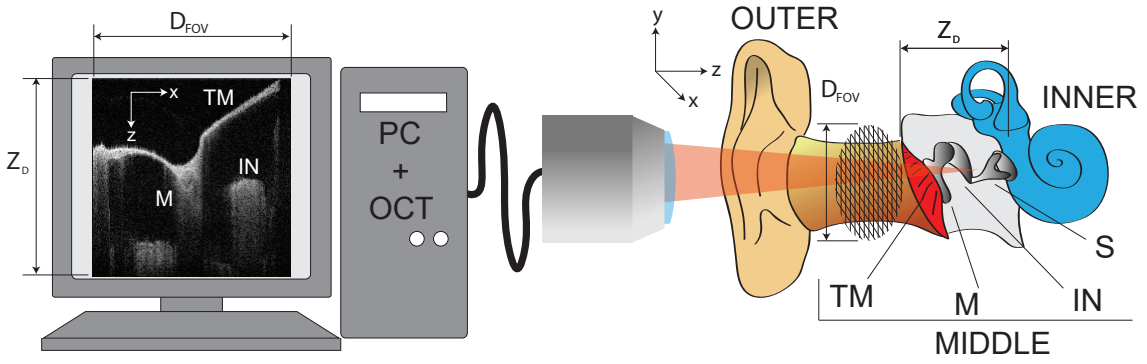

Figure 2.1: Diagram of the desired OCT system for transtympanic imaging of the middle ear showing the coordinate axes, x,y,z, used throughout the work, the basic imaging configuration down the ear canal, and the lateral and axial extents of the VOI, defined by z_D and D_{FOV}. **TM** tympanic membrane, **M** malleus, **IN** incus, **S** stapes, **OCT** optical coherence tomography.

SS-OCT systems lacked the phase stability needed for Doppler imaging and the range needed to image the full middle ear volume. It would not be until the work presented in Chapter 3 that SS-OCT would become a viable option for this application.

2.4.3 Key Challenges of OCT-Based Middle Ear Imaging

In conventional OCT systems, a focused beam with a DOF roughly equal to the collected range of depths is scanned laterally across the field of view (FOV), shown as a grid in Figure 2.1. To image the full axial extent of the middle ear from the TM to the cochlear promontory (*i.e.* along z in Figure 2.1), our experiments in cadavers suggested that axial ranging of at least $z_D = 10$mm is required, necessitating an equivalent DOF in the configuration of the scanning optics. Our experiments also suggested that a circular field of view of diameter $D_{FOV} = 10$mm (*i.e.* along $x \times y$ in Figure 2.1) is sufficient to capture the full lateral extent of the TM and the portion of the middle ear cavity with direct line-of-sight from the ear canal. This implies that the target system should allow an accessible VOI of a $\approx 1\text{cm}^3$, significantly larger than any previously demonstrated systems.

While broadband light sources are available down to visible wavelengths that could be used to provide extremely high resolution, because it is the middle ear and ossicles that are of key interest to this work, and the fact that scattering losses in tissues presumably similar to the TM are lower at longer wavelengths, like in dermis or

epidermis [119], operation at the longest available wavelengths in the NIR is desirable. For our system we used a center wavelength of $\lambda_0 = 1310$nm to take advantage of the high-powered, low-noise SLDs available at that wavelength. Even longer wavelengths could be used to further reduce scattering losses in the TM, but at the expense of lower resolution and a poorer availability of high-powered, broadband optical sources.

For generic OCT sample arm optics, the axial DOF of the scanning beam is related to the system NA by [6]:

$$DOF = \frac{0.565\lambda_0}{\sin^2\left(\frac{\sin^{-1}(\mathrm{NA})}{2}\right)} \tag{2.1}$$

For the low-NA scenario of trans-tympanic imaging, the small angle approximation applies and so the numerical aperture required to avoid limiting axial scanning range due to confocal gating can be approximated by:

$$\mathrm{NA} < \sqrt{\frac{2.26\lambda_0}{z_D}} \tag{2.2}$$

For $z_D = 10$mm at a wavelength of $\lambda_0 = 1310$nm, NA is limited to < 0.017. We found that acceptable sharpness in the images could be obtained with an NA < 0.022, but further increase lead to noticeable levels of defocusing at the proximal and distal ends of the images, i.e. at the TM and the cochlear promontory, respectively. This NA is an order of magnitude lower than those typically used in opthalmic OCT scanners [120]. With a NA this low the resulting decrease in lateral resolution may be acceptable in the ear, but the associated loss in light-gathering ability leads to challenges in collecting sufficient back-scatter to form an image with adequate SNR for clinical fidelity. This is particularly true in TD-OCT which is at a sensitivity disadvantage relative to FD-OCT methods.

It is important to consider the metrics of the imaging system's performance that matter most to clinician; contrast, frame-rate and resolution. Because all important anatomical structures in the middle ear are suspended in air, contrast in otological images is equivalent to SNR. If we also reasonably assume that the FOV is sampled

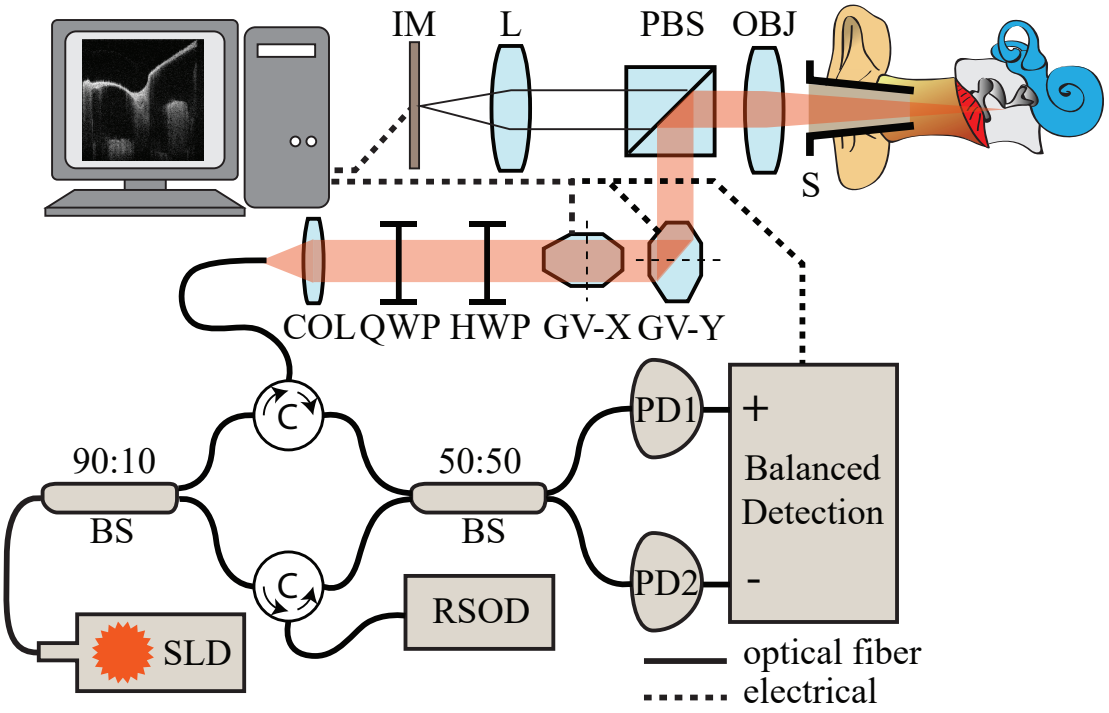

Figure 2.2: Detailed schematic of the TD-OCT imaging system assembled for this work. **IM** image sensor, **L** en-face imaging lens, **PBS** polarizing beam splitter, **OBJ** objective lens, **S** speculum , **COL** collimating lens, **QWP** quarter-wave plate, **HWP** half-wave plate, **GV** galvanometer mirror, **BS** fiber beam splitter, **C** fiber circulator, **PD** photodiode, **SLD** supler luminescent diode, **RSOD** rapid scanning optical delay line.

laterally in steps roughly equal to the focused beam's spot size, then following a derivation similar to that in [6] but re-writing in terms of the parameters of interest, the SNR at a feature within a shot-noise-limited TD-OCT image using a Mach-Zehnder interferometer with balanced detection and optimal measurement bandwidth, like the system described in Section 2.5 and shown in Figure 2.2, is given by:

$$\mathrm{SNR} = \frac{P_0 \alpha R_s \rho \pi}{q \Delta k z_D f_r N_l} \tag{2.3}$$

where P_0 is the total available optical power, α is the fraction of light sent to the sample arm, R_s is the reflectivity of a feature in the sample, ρ is the detection responsivity, q is the charge of an electron, Δk is the full-width half-maximum bandwidth of the optical source in wavenumbers, z_D is the axial scan-range of the measurement, f_r

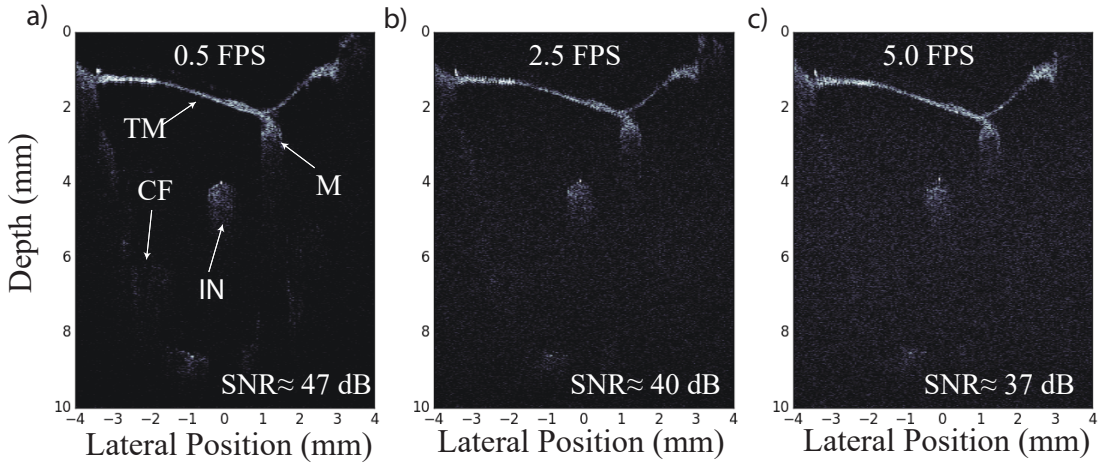

Figure 2.3: SNR comparison of transtympanic 2D B-mode images of a normal cadaveric ear at different framerates. SNR at the incus is indicated in each image. All three images are displayed with 35 dB dynamic range starting 5 dB above the RMS noise floor for the $f_r = 0.5FPS$ configuration. **IN** incus, **M** malleus, **TM** tympanic membrane, **CF** cochlear floor.

is the image frame-rate and N_l is the number of lines in the image. This equation highlights the fundamental SNR trade-off in TD-OCT, since SNR is inversely proportionality to z_D, f_r and N_l implying that sensitivity must be sacrificed in order to scan faster or over a longer range. In general, this is due to the fact that faster scanning requires a wider analog detection bandwidth. This fact is particularly problematic for real-time imaging of the middle ear's large VOI. This effect can be seen in Figure 2.3 which shows 2D images containing $N_l = 200$ lines and acquired at frame rates of $f_r = 0.5$ FPS, 2.5 FPS and 5.0 FPS. This trade-off holds even for non-shot-noise-limited imaging so long as the noise is white. Throughout this work, we specify SNR as

$$SNR = 10 \log \frac{i_i^2}{i_n^2} \tag{2.4}$$

Where i_i is the peak interference photocurrent produced by the backscatter from a particular structure within the sample, and i_n is the root-mean-squared (RMS) noise level in the measurement (*i.e.* the root-mean-squared photocurrent measured with no sample in place, or in a region where there is no backscatter). Images in this chapter are displayed with the minimum greyscale value situated 5 dB above i_n and with a 35 dB DNR in order to enhance contrast (*i.e.* reflections brighter than 5dB + 35dB = 40dB above RMS noise are clipped and displayed as the maximum

brightness level).

With a total of 220 μW arriving at the detector from the reference arm of the interferometer, and 9.2mW available at the sample, we have measured our system sensitivity to be $S_i \approx 100$dB at the center of the image when imaging at an A-line rate of $f_l = 50$LPS over $Z_D = 10$mm (i.e. a reflection in the sample of -100 dB will give SNR = 0dB). System noise was measured at 3.6 dB above the expected shot-noise floor. With this system, we are able to generate images with SNR $\approx$ 50dB at the incus through the TM. However, for an image containing $N_l = 100$ image lines, this sensitivity is only achievable at a frame rate of $f_r = 0.5$FPS, significantly slower than real-time. If the frame rate is increased to $f_r = 5$FPS, the sensitivity decreases to approximately $S_i \approx 87$dB with an SNR at the incus of just 37dB.

2.5 Methods

Images were obtained in two cadaveric human temporal bones taken from the same head. The bones were obtained fresh-frozen (unfixed) from Anatomy Gifts (Hanover, MD), and thawed to room temperature before use. The bones were stored in a refrigerator overnight at $4°C$. They were allowed to come up to room temperature before imaging each day and kept moist by periodic spraying with saline. The external ear canal and soft tissue were removed from the bones for convenience, but images were acquired along a line of sight representative of that available to clinicians, *i.e.* along the ear canal. All procedures were undertaken under the oversight of the Dalhousie University Research Ethics Board.

The overall system topology is shown in Figure 2.2. The light source is a Denselight Semiconductors (Singapore) DL-CS3504A fiber coupled InP SLD. Its emitted power was measured to be $P_0 = 54.3$mW with a nominal FWHM bandwidth of $\Delta\lambda = 56$nm centered at $\lambda_0 = 1310$nm. The source was guided to a 90/10 non-polarizing beamsplitter which directed $\alpha = 90\%$ of the optical power to the sample arm and the remaining 10% to the reference arm of the custom-assembled, Mach-Zehnder fiber interferometer. Optical circulators directed incident light to the sample and reference arms and the reflections to a 50/50 fiber beamsplitter with a balanced detector [121].

Variable time-delay of the sample-arm light required for axial scanning in TD-OCT was generated using a diffraction-grating based rapid-scanning optical delay-line (RSOD) [122]. Its design was based on one used previously using polarizing elements to perform double-pass beam de-scanning [123]. In our system, we achieved $z_D = 12$mm of useful scanning range in air using a lens with a focal length of 100mm, at an A-line rate of $f_l = 1$kLPS. Total RSOD insertion-loss was limited to just 6.9 dB at mid-delay-range by operating the diffraction grating near the Littrow condition (*i.e.* by using an incidence angle of 3°, with a grating pitch of 500 grooves/mm and a blaze angle of 20°). By relocating the quarter-wave-plate (QWP) beyond the diffraction grating, it ensured that only pure horizontally or vertically polarized light was incident on the grating, rather than circular, avoiding the polarization-dependent losses that would have been present in [123]. The RSOD was adjusted for dispersion compensation to minimize the width of the axial point-spread-function (PSF) [124].

In the sample arm, light exited from a fiber collimator (Thorlabs TC18APC-1310) with a 3.2mm $1/e^2$ beam diameter. A two-axis galvanometric mirror provided lateral scanning across the 10 mm × 10 mm FOV. The centroid of the two mirrors' axes was located at the back focal plane of a 100mm achromatic doublet objective lens for approximate telecentricity (Thorlabs AC254-100-C). The overall system NA was limited by the size of the collimated beam to $NA \approx 0.016$. The beam profile at the focus (on-axis) was measured to be 52 μm in diameter which agreed with the diffraction limited value to within experimental error. Quarter-wave and half-wave plates (HWP) were used to control the polarization in the sample arm and maximize fringe visibility.

To aid with imaging around the curvature of the human ear canal, a fixture for rigidly mounting a speculum to the front of the objective was provided, but due to the telecentricty of optics significantly limiting the achievable field of view through the 4mm speculum aperture, it was not used for the final measurements presented in this chapter. Instead, access to the full lateral extent of the TM was provided via drilling away of the boney ear canal. This is a limitation of the experiment that highlights the practical need for imaging probes specifically designed to accommodate the human anatomy.

Simultaneous conventional en-face imaging of the TM was incorporated into the

system using the CMOS sensor from a Logitech c270 HD webcam. Available thin-element dichroic mirrors were found to cause significant ghosting in the OCT image due to multiple internal reflections, so a thick-element polarizing beam splitter was used to separate the NIR and visible light. No visible light source was integrated into the optics, and so the en-face images were useful only during alignment of the sample since ambient light was available, but not once final alignment of the sample was achieved. In this setup, the optics were fixed in place, and alignment of the TM to the imaging axis was accomplished by mechanical manipulations of the specimen and clamping it in place.

The differential optical signal from the interferometer was guided to a Thorlabs PDB145C balanced detector with a transimpedance gain of 51 $k\Omega$. A coarse analog bandpass filter with a mid-band gain of 10.2 V/V for DC blocking and anti-aliasing provided signal conditioning before digitization of the image line data with a 16-bit PCIe digitizer (Alazar ATS9462). The sampling rate for digitization was locked to the A-line scan rate so that 9760 points were acquired for each A-line regardless of the scan rate. Final filtering of the acquisition data was performed digitally with an 8th order Butterworth zero-phase-delay bandpass filter with a center frequency and passband-width that also scaled with A-line rate. Image lines were generated from the filtered A-line data by decimation of the absolute value and plotting on a logarithmic scale. Synchronization of the RSOD, lateral scanning mirror control and acquisition triggering was accomplished using a multi-functional data acquisition board (National Instruments NI-USB-6259) and controlled using custom scripts written in Python. Scanning parameters were controlled using a custom interactive graphical user interface (GUI) that provided real-time display of both the OCT imaging and an en-face view of the TM from the CMOS camera.

We used this system to investigate the required sensitivity and dynamic range, and the impact of transtympanic acquisition on imaging at the ossicles.

2.6 Results

2.6.1 Optical Loss Across the Tympanic Membrane

The set of photons that are desired for measurement in OCT are "ballistic photons" [125], *i.e.* photons that only experience a single back-scattering event before re-entering the transverse spatial mode of the interferometer. All other photons either experience multiple scattering events before re-entering the transverse mode (leading to multiple scattering effects), or experience scattering or absorption events that lead to the photon never re-entering the mode, and are lost and don't contribute to the measurement. While tomographic imaging of the TM itself can provide clinical value [71], the present system is designed primarily to image the middle ear, to which the TM presents an impediment in two ways: not only does the TM scatter photons that never reach the ossicles and effectively introduces an optical loss in the system, it also creates a strong reflection in every A-line that can obscure the weaker reflections of the structures in the middle ear if dynamic range limitations are present, irrespective of sensitivity.

One can obtain an estimate of the two-way optical power transmittance through the TM, T_{TM}, by considering its optical properties. While the scattering coefficient in human TM tissue has not been measured to our knowledge, other authors have made the reasonable assumption that scattering in the TM will be similar to scattering in dermis [126] which has been characterized in a number of studies [119, 127]. However, approximating the TM as epidermis produces better agreement with our experimental measurements. The scattering coefficient of epidermis at $\lambda_0 = 1310$nm is $\sigma_s \approx 12.5\text{mm}^{-1}$, and the absorption coefficient is $\sigma_a = 0.1\text{mm}^{-1}$ [119]. The probability that a photon incident on the TM will not be scattered in passing through tissue of thickness d is $T_s = \exp\{-\sigma_s d\}$. In a TM of thickness $d = 100\mu$m, $T_s = 29\%$ of the incident photons will pass through without scattering. By a similar calculation, the expected transmittance due to absorption in the TM is approximately $T_a = \exp\{-\sigma_a d\} = 99\%$. With an index of refraction $n_r \approx 1.4$, the Fresnel transmission coefficient for the TM in air is $T_F = 1 - \left({}^{n_r-1}/_{n_r+1}\right)^2 \approx 97\%$. One would then reasonably expect the TM to have an overall transmittance given by $T_{TM} = T_s^2 \times T_a^2 \times T_F^4$, where T_s and T_a are raised to the second power because of the two-way transit, and

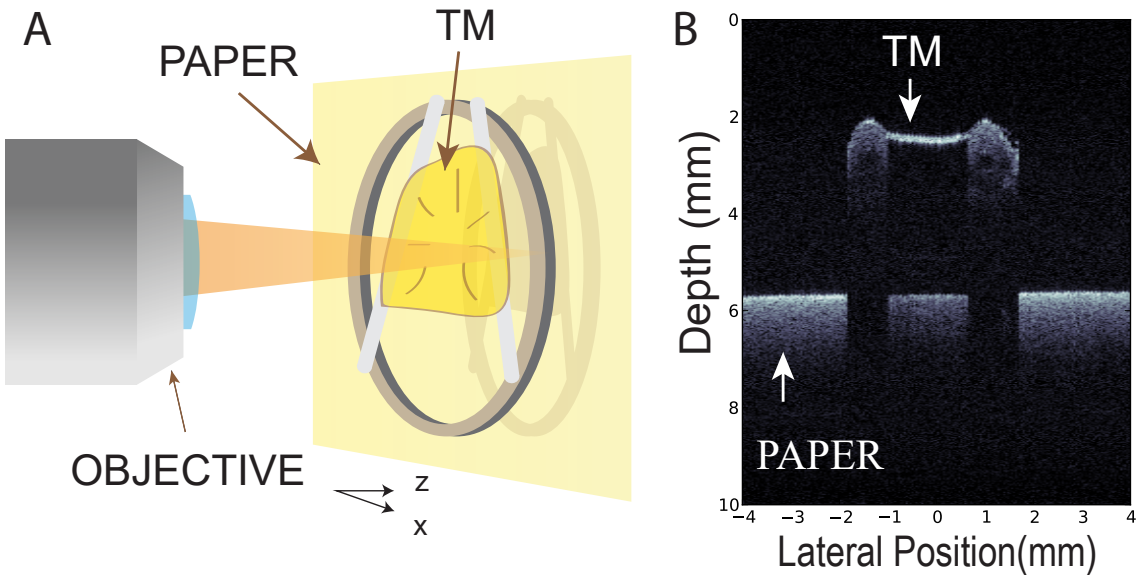

Figure 2.4: Experimental setup used for measurement of the transmittance of the TM. A, A diagram of the physical arrangement where paper was used as an OCT reference reflector behind a section of excised human TM over a clear aperture. B, OCT image of the arrangement described in A. **TM** tympanic membrane.

T_F is raised to the fourth power because because of the four tissue-air interfaces encountered in the two-way transit. This gives an expected overall transmittance of $T_{TM} \approx -11.4$dB, nearly completely accounted for by scattering.

We measured T_{TM} by harvesting a section of cadaveric TM and mounting it over a clear aperture placed in front of plain white paper used as a reference reflector, as shown in Figure 2.4A. This entire assembly was then imaged with the OCT system, ensuring sections of both the unobstructed paper and the TM-obstructed paper were within the FOV, and at constant depth, z, in the images to ensure matched sensitivity across all regions of the paper. The two-way optical loss across the TM was calculated by taking the ratio of the averaged peak fringe amplitude in each line within the two areas of interest, giving a measured transmittance of $T_{TM} = -13.5$dB. This is in very good agreement with the estimate, considering the thickness of the TM sample appeared slightly thicker than 100μm in the A-line data ($d \approx 112\mu$m). Assuming the scattering properties of dermis ($\sigma_s \approx 7.5\text{mm}^{-1}$) would estimate $T_{TM} \approx -7$dB, and suggests that the TM's optical properties more closely resemble those of epidermis.

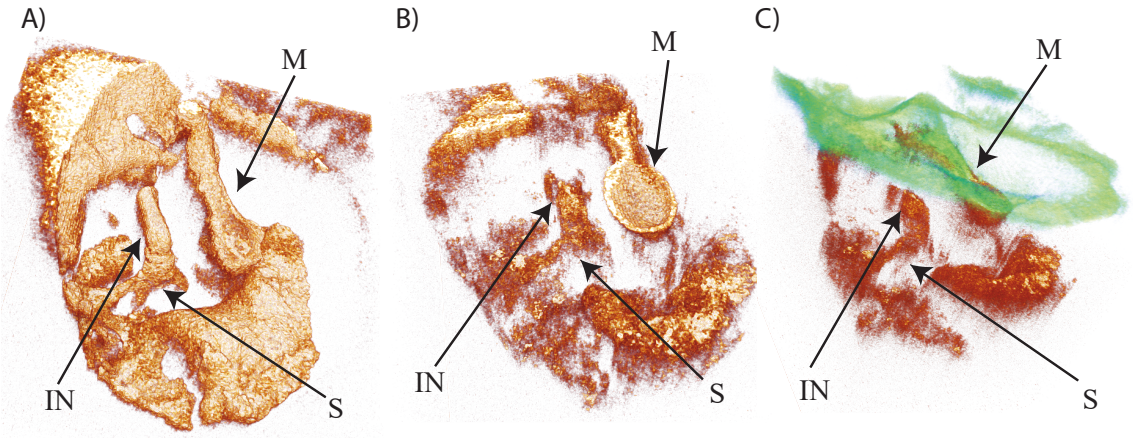

Figure 2.5: 3D reconstructions of a normal cadaveric middle ear. A, With the TM surgically lifted. B, With the TM in placed but removed by digital tympanotomy. C, With the TM shown in transparent green. **M** malleus, **IN** incus, **S** stapes.

2.6.2 Digital Tympanotomy

Despite the increased use of imaging technologies such as CT and MRI in middle ear imaging, the gold standard for diagnosis in the middle ear remains exploratory tympanotomy [128]. With OCT's ability to image structures medial to the TM non-invasively, it offers the potential to reduce the need for exploratory tympanotomy by providing 3D images of middle ear anatomy without disturbing the TM or the need to take the patient into surgery to make an accurate diagnosis. Figure 2.5A shows a very high fidelity rendering of the middle ear and ossicles acquired with the TM lifted out of place, mimicking the surgical scenario. More excitingly, trans-tympanic OCT can be thought of as enabling a type of *digital tympanotomy* in which the TM is removed via post-processing of a volumetric scan of the intact ear, as shown in Figure 2.5B, providing a view very much similar to that seen in the OR. The image in Figure 2.5B displays all the same features of the middle ear as Figure 2.5A, but with only somewhat degraded image quality due to the presence of the TM. Figure 2.5C shows an alternative approach to visualizing the same data in which different color schemes are used for displaying the TM and middle ear. This could be useful in surgical planning, for highlighting anatomical landmarks, and for effectively communicating with a patient during the consenting process.

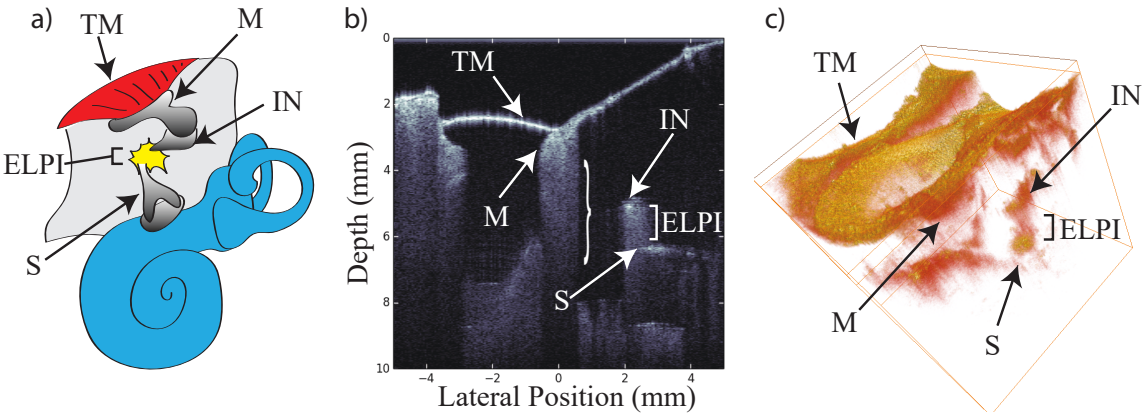

Figure 2.6: Images of ELPI. A, Diagram, B, 2D B-Mode image and, C, 3D volumetric image of a cadaveric ear in which a surgical manipulation has been made to the incus to simulate erosion of the long process. The curly brace highlights a region containing significant multiple scattering artifact within the bony ossicles. **TM** tympanic membrane, **M** malleus, **IN** incus, **S** stapes, **ELPI** erosion of the long process of the incus.

2.6.3 Diagnostic Validation

While the notion of OCT as a diagnostics tool for otology already existed in the literature, there lacked any examples of what images of commonly encountered pathologies of the middle ear may look like in an anatomical B-Mode image. For the purposes of a preliminary demonstration of potential areas of clinical relevance for whole-middle ear imaging, the two temporal bones were prepared so as to simulate relevant conditions, and were subsequently imaged with OCT. In both cases the temporal bones were prepared by lifting the posterior edge of the TM, making the surgical manipulation to the middle ear, and then replacing the TM so that the middle ear could be imaged through it.

In the first preparation, shown diagrammatically in Figure 2.6A, simulation of an erosion of the long process of the incus was made. The resulting 2D and 3D images are shown in Figures 2.6B-C.

In the second preparation, shown diagrammatically in Figure 2.7A, we simulated an unsuccessful PORP placement. In this scenario, a residual gap was left between the TM and the prosthesis, simulating a situation that would result in a residual, post-operative conductive hearing loss due to an incorrectly assessed anatomical distance

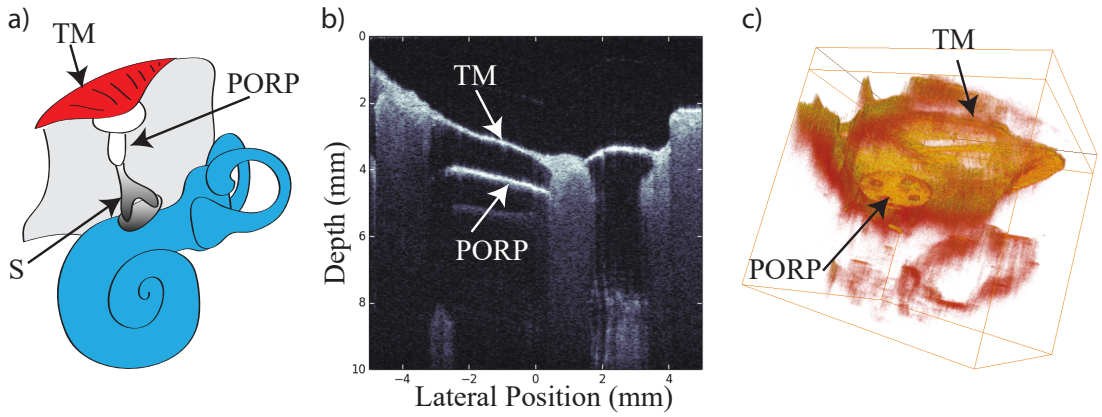

Figure 2.7: Images of a PORP. A, Diagram, B, 2D image and, C, 3D volumetric image of a cadaveric ear in which a partial ossicular reconstruction prothesis was implanted correctly at the stapes but deliberately left unattached to the tympanic membrane to simulate migration. Both the prosthesis and the gap between it and the TM are visible in the images. **TM** tympanic membrane, **S** stapes, **PORP** partial ossicular replacements prosthesis.

between the head of the stapes and the eardrum, which varies from case to case.

2.7 Discussion

2.7.1 Multiple Scattering in the Ossicles

The images shown in Figures 2.5, 2.6 and 2.7 all exhibit prominent artifacts related to multiple scattering. The photons that are multiply-scattered take long paths through tissue and so appear to originate from a deeper depth than their singly-scattered counterparts, often from a depth completely beyond the structure being imaged. While multiple scattering is commonly observed in soft-tissue OCT where it can be the limiting factor on contrast at deeper depths, in middle ear images it appears to be a particularly prominent artifact around bony features, owing to their high scattering. It is the multiple-scattering within the ossicles that is the source of the speckle-filled tails that appear behind them in Figures 2.6 and 2.7. The effect is to such a degree that it prevents the ability to resolve the medial-side air-bone boundaries within the middle ear, and is enough to obscure fine detail in nearby structures. In the specific case of Figure 2.6B, where an example of the artifact has been identified trailing behind the malleus, the multiple scattering is sufficiently strong to partially camouflage

the discontinuity in the ossicular chain between the incus and stapes. The missing bone-mass is more obvious in Figure 2.6C in 3D, suggesting 3D renderings of middle ear anatomy may be particularly useful for identifying structural abnormalities.

There are a few strategies that could potentially be pursued for reducing the multiple scattering. Some improvement can be obtained through spatial compounding [129] and polarization-mode OCT can also be used to separate the singly and multiply scattered light [130]. Another approach to improving the system would be to increase the NA [131]. Endoscopic imaging has been used at higher NA for TM imaging [71], but has disadvantages as compared to a free-space approach in terms of comfort, the need for inter-subject sterilization, and the required skill of the operator. Moreover, moving to higher NA would necessitate dynamic focusing [85, 132] or synthetic aperture techniques [133] to maintain depth-of-field.

2.7.2 Design Considerations

Taking the image in Figure 2.3A as a representative example of the desired level of image fidelity for real-time diagnostic use, and given the losses present in the TM, estimates of the S_i and DNR required for a clinical otological OCT system can be made. Firstly, satisfactory bone-to-air contrast can be expected at the osscicles if $S_i > 97$dB, which is a challenging but theoretically achievable goal at real-time rates, assuming the full sensitivity advantages of FD-OCT methods can be realized [134]. Perhaps a more challenging requirement to meet in an FD-OCT system is the required DNR. Given $T_{TM} \approx 13.5$dB of loss incurred by transiting the TM and SNR ≈ 47dB desired at the ossicles, DNR > 60.5dB is required. TD-OCT is tolerant to saturation from bright reflectors at isolated depths in an A-line since it does not prevent valid data being obtained from dim reflectors at other depths, *i.e.* since they are rejected by the coherence gating, making it relatively easy to produce high DNR images. The system described in this chapter achieves DNR = 70dB. By comparison in FD-OCT methods, at any one point in time light from all depths contributes to the measurement, and by the Fourier-relationship that exists between the measured quantity and the displayed A-line, any non-linearities present in the measurement (*e.g.* saturation), or if there exist any deviations from linear-in-optical-frequency sampling of the spectral interferogram processed via DFT, it produces artifacts that

can corrupt large regions of the images [118]. This is a factor worth considering when attempting to design an OCT system for imaging the ossicles transtympanically.

2.7.3 Clinical Relevance

At the time of publication, the images of Figure 2.6 were very exciting as the pathological gap between the incus and stapes was resolvable and had not previously been demonstrated. The images in Figure 2.7 were also very exciting in that the head of the titanium prosthesis that couples to the TM is clearly visible with very sharp definition, as is the problematic gap separating the prosthesis from the TM, suggesting the ability to image prostheses with ease following surgery. Notionally, this simulated case suggested that OCT could help address a concern surgeons often have when bringing an ossiculoplasty patient out of anesthesia, since there is always residual uncertainty about the integrity of the reconstruction and how successful the ABG closure will ultimately be. Realistically, however, standard practice in this type of PORP surgery has come to entail reinforcement of the TM using a cartilage or otherwise autologous grafting material to prevent extrusion of the prosthetic. The reality is that the additional thickness resulting from the graft-reinforcement, effectively, precludes OCT penetration to the middle ear. Since publication, a significant area of research within our group has been sparked to address the difficulties in obtaining acceptable transtympanic imaging following tympanoplasty (*i.e.* in the presence of graft materials over the TM). Specifically, work is underway to investigate whether a combination of optical clearing agents [135] and moving to thinner grafts will enable OCT penetration in this patient group. An example of the impact of tympanoplasty on transtympanic OCT is provided in Chapter 5.

It is worth understanding that, at the time that this work was published, it remained an open question whether trans-tympanic OCT for middle ear diagnostics could be useful for detecting anything of clinical relevance in a practical scenario. The images presented in this chapter represent a set of identifiable scenarios that are demonstrative only of the clinical potential of anatomical transtympanic OCT. No such OCT images of real-world, gross-anatomical pathologies had been previously published. While the published work only specifically addressed the two cases of ELPI and PORP misplacement or migration, the images convincingly demonstrated

the ability to resolve structural defects, although admittedly only in contrived scenarios. Nonetheless, this was sufficient evidence to support the notion of clinical utility in other commonly encountered scenarios including:

1. In patients with persistent conductive hearing loss following ossiculoplasty, the ability to visualize the reconstruction could allow a surgeon to decide whether any improvement is possible with revision surgery

2. Confirmation of the presence of otosclerotic plaque formation around the footplace of the stapes via direct visualization of the structural defect could provide added pre-operative confidence of the pathology's presence without needing CT, which is not always effective [2]. After gaining experience with live patient imaging, it is now recognized that anatomical imaging of the stapes footplate is not possible in most ears, and that an alternate approach to detecting stapes fixation is more suitable (See Chapter 4)

3. The direct visualization of tympanosclerotic plaque formation could provide evidence to support tympanosclerosis as the root cause of CHL

4. Structural anomalies in cases of congenital ossicular malformation could be resolvable and inform decision making about surgical versus conservative treatment. While OCT likely provides sufficient resolution to observe structural abnormalities of this type at the ossicles, the line-of-sight to the middle ear available transtympanically and the fact that OCT cannot penetrate to resolve the medial surfaces of the ossicles could limit usefulness in this regard.

5. Traumatic injury to the ossicular chain leading to macro fractures or dislocations of the joints could be directly visualized.

Our set of hypothesized use cases for anatomical trans-tympanic OCT remain largely unchanged. The surgical management of each of these conditions differs and carries different success rates and risks. Surgeons are routinely forced to improvise solutions and face problems in the OR that may not have been discussed as a likely scenario with the patient. The ability to make more accurate diagnoses in the clinic would allow the surgeon to better counsel patients pre-operatively about the risks

and benefits of intervention and to aid them in their decision-making, and possibly to reduce the number of unnecessary surgeries. Benefits surrounding the careful navigation of the consenting process when limited pre-operative information is available have become increasingly potent motivators for the continued development of the technology, and has proven to be a helpful measure for identifying the areas of otology that could most benefit from trans-tympanic OCT imaging.

2.8 Conclusions

In this chapter's work, we demonstrated a TD-OCT system to asses the design challenges faced in developing clinically useful trans-tympanic OCT of the human middle ear. We investigated the deleterious effects of being forced to image at low NA (NA <0.022) and from outside the TM ($T_{TM} \approx$ 13.5dB). We also quantified requirements for system sensitivity ($S_i \approx 97$ dB) and dynamic range (DNR ≈ 60.5 dB) needed to obtain acceptable image quality. Preliminary validation in human temporal bones showed that images obtained with our TD-OCT system provide diagnostically useful information in erosion of the long process of the incus and in prosthesis migration, highlighting how OCT may fit within clinical otology and outlining new motivations for bringing OCT into the otological clinical space.

The underlying commentary behind the work in this chapter, collectively, was that if trans-tympanic OCT is going to succeed and develop to positively impact clinical practice, off-the-shelf OCT engines impose limitations that are worth addressing, but that the required level of performance is achievable using known methods. As the original intent for this portion of work was to determine system requirements and to reaffirm that clinically relevant information would be accessible, the TD-OCT system, shown in Figure 2.8, was promptly retired and dismantled, having successfully served its purpose.

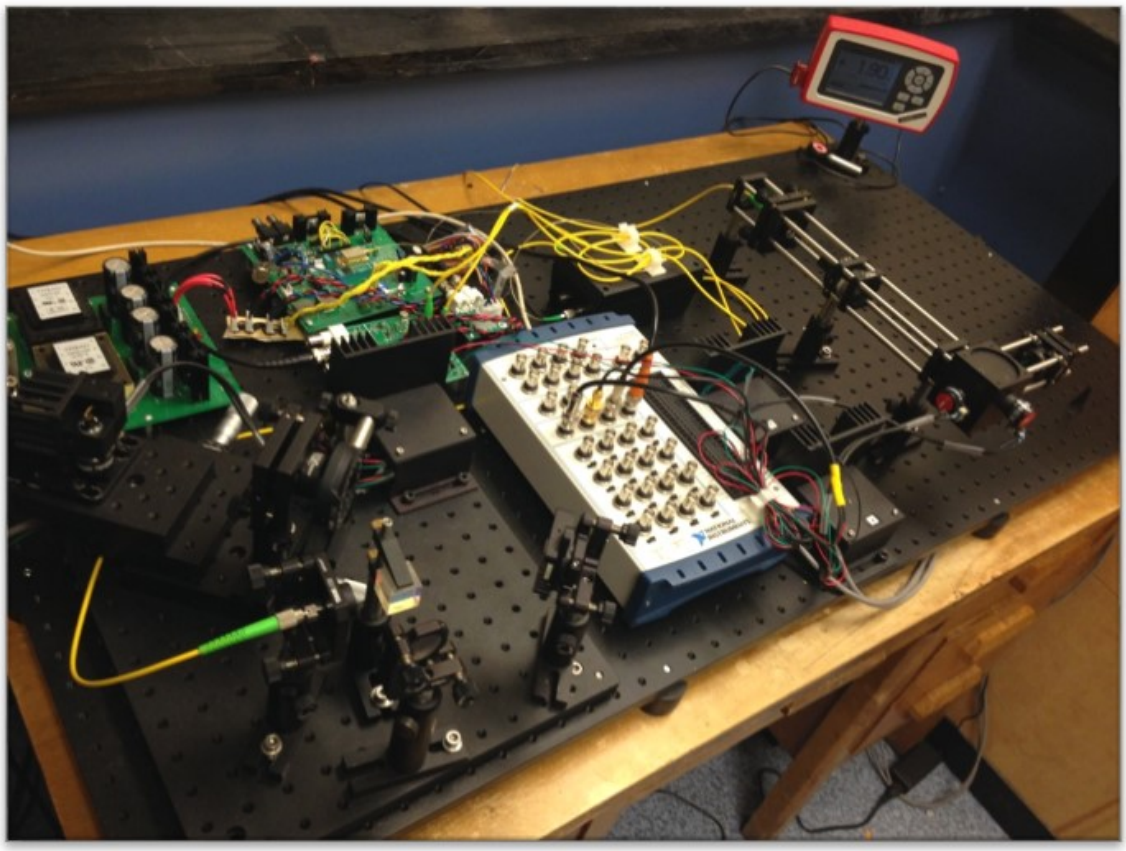

Figure 2.8: The benchtop TD-OCT system used during (and retired immediately following) the work in Chapter 2

Chapter 3

The Development of a Swept-Source Optical Coherence Tomography Imaging System with Doppler-Vibrographic Sensitivity at the Ossicles, *in vivo*

Dan MacDougall,[a] Joshua Farrell[a], Jeremy Brown[a,b], Manohar Bance,[a,c] Robert Adamson[a,b]

[a] School of Biomedical Engineering, Dalhousie University, Halifax NS, Canada

[b] Department of Electrical and Computer Engineering, Dalhousie University, Halifax NS, Canada

[c] Division of Otolaryngology Head and Neck Surgery, Department of Surgery, Dalhousie University, Halifax NS, Canada

3.1 Author Contribution Statement

D. MacDougall and R. Adamson conceived the experiments and analyses. J. Farrell contributed to mechanical design and 3D rendering software development. J. Brown and M. Bance provided technical and clinical support. D. MacDougall was responsible for optical, electronic, mechanical, and software design of the imaging system; execution of the *ex vivo* and *in vivo* imaging experiments; analysis of the imaging results; and was the lead and corresponding author on the journal submission.

3.2 Preamble

This chapter is based on my second peer reviewed publication [83]. Its contents remain, largely, unaltered. However, introductory information that would duplicate the contents of Chapter 1 have been omitted or otherwise changed for conciseness. Some additional, unpublished experimental details have been opportunistically added, and some modifications have been made to lend context and render this document, as a whole, self-consistent in terminology and style. Specifically, the introductory

section has been altered to provide more insight into the motivation and novelty for the work at the time the original manuscript was submitted for peer review and to explain the work's fit into the overall story of my thesis; the mathematical description of the Doppler extraction algorithm has been simplified and the variables renamed to avoid confusion with coordinate systems used elsewhere in the text and to provide a clearer understanding of the processing steps; descriptions of pathologies and surgical interventions have been reduced, and the reader is directed to Section 1.2.2 for those details; discussion points have been expanded and altered to better reflect insights that have been gleaned since the paper was published.

3.3 Abstract

We present the design, implementation and validation of a SS-OCT system for real-time imaging of the human middle ear in live patients. Our system consists of a highly phase-stable Vernier-tuned distributed Bragg-reflector laser along with a real-time processing engine implemented on a graphics processing unit. We use the system to demonstrate OCT-DV measurements of the middle ear's vibrational response to sound in cadavers, and *in vivo* for the first time. We also show the first *in vivo*, full middle ear transtympanic OCT images with video rate 2D B-mode, and 3D volumetric B-mode imaging. All measurements were performed non-invasively through the intact TM, demonstrating that the technology readily translates to the clinic.

3.4 Introduction

Section 1.3 provided a complete review of the relevant anatomical and OCT-DV literature in the ear, detailed the rationale for its potential as a diagnostic tool in the middle ear, and referenced the similar work that was ongoing in parallel to ours at other academic institutions, most notably at the time were [88, 113] which were both limited to only cadaveric imaging, and were both limited in accessible volume of interest (VOI).

3.4.1 Motivation

With the system requirements for clinical utility established and understood in Chapter 2, the next significant task was to develop a system that addressed all of the practical challenges associated with live-patient imaging; to speed up imaging to real-time rates; to extend functionality and incorporate functional OCT-DV capabilities into the system; and to use the system in *in vivo* OCT-DV measurements. To re-iterate and expand upon the challenges that we faced and aspects that would differentiate this second system design from the first:

1. To achieve sufficient suppression of motion-related image artifacts (i.e. blurring and distortions due heart beat, breathing, normal tremor), frame rates would need to be significantly faster than the TDOCT system of Chapter 2, with fully sampled 2D B-Mode imaging acquired, processed and displayed at $f_r \approx 20$FPS. There were no previous examples of real-time transtympanic OCT imaging of the human middle ear being performed in the literature at the time. While the TD-OCT system of Chapter 2 could do real-time imaging and produce clinically acceptable images, it could not do both simultaneously.

2. Adequate image fidelity was needed with the OCT engine operating at speed, and with imaging results displayed in a manner appropriate for an operator to be able to control the system with relative ease. This necessitates some degree of automation, and user-interface and workflow design. In other words, some minimum level of usability was needed.

3. The presence of the ear canal in live subjects significantly complicates achieving acceptable FOV. The Boppart group *et al.* previously published work in otitis media characterization and were already performing *in vivo* anatomical OCT measurements of the ear [73, 76–78, 82, 87] but their focus remained on small portions of the TM surface, and only over the narrow depth range where the TM resides. Our motivation was to produce full middle ear images, in real-time, as this hadn't been previously demonstrated. Accommodating the external ear canal necessitates the design of scanning optics specifically tailored to the desired VOI to minimize clipping in the ear canal and for subject comfort.

Additionally the OCT engine would still need to meet the relatively long axial ranging specification of $z_D = 10$mm.

4. The incorporation of a means to rapidly align the optics to the ear canal of a live subject in an acceptably comfortable fashion, without introducing motion artifacts.

5. The development of a real-time OCT-DV processing sub-system and a mechanism to display and immediately interpret the quality of functional results. The signal processing required to perform imaging and Doppler processing in real time represents a significant computational challenge. While it's sometimes difficult to infer the processing capabilities and speeds in the OCT-DV literature, the previously demonstrated benchtop OCT-DV experiments were generally of designs that used off-line processing to generate results. This kind of approach is incompatible with collecting data in a clinic with realistic patient throughput and willingness to participate in a study, and where you must have the ability to quickly confirm the quality of the measurements while the patient is still present. Other authors had noted the lack of a sufficiently fast Doppler processing engine as a key barrier to clinical deployment of the technology [88]

6. The incorporation of an integrated sound stimulus system that can excite the ear into a physiological response while conducting the OCT-DV measurements.

Our overarching motivation for taking on the development of a system that addresses all of these issues was to enable a research program where the execution of scientific studies on live patient populations using OCT-DV would be possible.

3.4.2 Background

3.4.3 Vernier-Tuned Distributed Bragg Reflector Lasers: the Enabling Technology

At the time of this work, *in vivo* OCT systems used in the ear had very limited depth range of a few millimeters and had not been able to image deep middle ear structures such as the stapes and cochlear promontory. This is owing, in part, to the inherent difficulties and trade-offs in achieving long axial ranging in OCT, regardless

of topology (TD-, SD-, SS-OCT), and generally the use of SD-OCT engines optimized for shorter ranging. Recall from Chapter 2 that long-range is technically feasible on its own in TD-OCT, but it comes at the cost of speed and sensitivity. Also recall from Section 1.2.4 that historically in SS-OCT, the practical limit for axial depth range has been the instantaneous coherence length, z_c, of the available sources, since it physically represents the maximum relative delay between the two arms of the interferometer where the beams remain temporally coherent and produce fringes when interfered.

Reliable and fast swept-lasers with the desired combination of tuning-range, coherence-length and sweep-rate had only recently become available as the work of this chapter was beginning. Earlier wavelength tuning mechanisms relied on moving parts like rotating polygons, galvanometers, and piezo-electrics which also would tend to degrade stability of the measured interference fringes due to poor sweep-to-sweep repeatability. The relatively recent arrival of the commercially available MEMS-tuned vertical-cavity, surface-emitting diode laser (MEMS VCSEL) and the akinetic Vernier-tuned distributed Bragg reflector lasers (VT-DBRL), while still very expensive and not yet very accessible, is revolutionizing OCT capabilities in terms of speed, range, and repeatability. Coherence length in Fourier domain mode locked lasers has also been demonstrated up to $z_c = 21$mm [136].

Our selection of SS-OCT as the best-suited topology for the desired OCT imaging system is owing largely to the unique nature of the VT-DBRL, as it had been shown that it could achieve SNR within 4.8dB of the shot-noise detection limit and simultaneously achieve coherence length sufficient to allow axial ranging in excess of $z_D > 17$cm [137]. While this much range is of limited use in soft tissue OCT applications (*i.e.* where imaging penetration becomes limited by scattering losses or multiple scattering), the long, transparent and air-filled middle ear requires it! The VT-DBRL was also capable of A-line rates$f_l > 100$kLPS, $\approx 100\times$ faster than than the TD-OCT system of Chapter 2, and more than adequate to accomplish the desired type of middle ear imaging.

The other tremendously useful aspect of the newly available VT-DBRL was its

remarkable sweep-to-sweep repeatability, and because the underlying system is completely electro-optically driven [137], it is readily synchronizable to sampling electronics without the need for complicated k-clocking or other phase referencing techniques [138]. In simple terms, the nature of this source leads to extremely stable-in-time interference fringes in the spectral interferogram, and so changes observed in the measured interference patterns are correctly attributable to relative motion between the arms of the interferometer. A mathematical treatment of the signals involved in phase-sensitive SS-OCT is provided in Section 3.5.3, but it is important for the reader to understand that in SS-OCT, by the Fourier-transform relationship between the interferogram and the depth-resolved reflectivity, depth information is encoded in the frequency of the measured signal. It is helpful to consider macroscopic displacements of structures in the sample (i.e. $>$ the size of a pixel) as resulting in frequency-shifting of the interference signal, whereas micro- and nano-scale displacements (i.e. $<$ the size of a pixel) result in phase-modulations without introducing frequency shift. Of course, in reality, both effects are simply the byproduct of phase accumulation in the reference arm, but it remains a helpful way of understanding the signals and why the VT-DBRL is so useful for this application. This breakthrough source's "phase repeatability", or as it is often called "phase stability", refers to its ability to produce optical frequency domain measurements that contain no phase-modulation when there is no relative motion between the arms of the interferometer. This performance characteristic is captured by the VT-DBRL's wavelength repeatability (RMS wavelength jitter $<$ 20 pm) that ultimately enables vibrational sensitivity within 6dB of the shot-noise detection limit [106, 137], and is the enabling feature for OCT-DV.

In parallel with the VT-DBRL, the MEMS-VCSEL continues to proliferate in the OCT literature as well. Since the work for this chapter was carried out, complex experimental SS-OCT systems using the VT-DBRL [139] and MEMS-VCSEL [140] have been demonstrated with ultra-long-range imaging capabilities and that take advantage of the coherence length breakthrough to an extent even greater than the otological OCT imaging described in this chapter.

3.4.4 Relevant Imaging Probes/Heads

As described in Sections 1.3, there have been a variety of proposed approaches to accommodating the ear canal for *in vivo* OCT of the middle ear, and each approach has distinct advantages and disadvantages. At the time of publication of this work:

1. **Endoscopes** previously demonstrated were most notably used to perform TM-only imaging *in vivo* [86]; and in the middle ear *in vivo* in [85], but only in a mouse model and with an extremely small field of view. Endoscopes have the advantage of insertion past the curvatures of the ear canal, but they require sterilization between patients, and an extremely skilled operator to use safely.

2. **Otoscopes** previously demonstrated were most notably used in the niche area of otitis media characterization where only small sections of the TM are of interest [76–80]; and in work very similar to that of this chapter, however with limited axial ranging, requiring stitching of multiple SD-OCT images in a cadaver model to capture the entire ossicular chain [88]. Otoscopes have the advantage of being very easy to manipulate, being safe to use with minimal training, and accomplishing inter-subject sterility via disposable specula. However, their hand-held nature presents the risk of introducing additional motion artifact into the images, and possible corruption of the OCT-DV signal.

3. **Surgical Microscopes** previously demonstrated hadn't been used for transtympanic middle ear imaging [69], although since the work of this chapter, very exciting microscope integration for this application has been demonstrated [84]. While mounted microscopes can provide excellent stability (i.e. hands free), one does not have the freedom to place the system's entrance pupil inside the ear canal, and simultaneous access to the entire surface of the TM is usually not possible.

3.5 Methods

Our system generated B-mode images at a nominal frame-rate of $f_r = 20$FPS, and could acquire individual OCT-DV measurements (*i.e.* at a single transverse coordinate in x and y, but at all points along z) in approximately 5s, at a safe sound

stimulus presentation level of $P_a \approx 100\text{dB}_{\text{SPL}}$ with acceptable sensitivity for making physiological measurements. Real-time OCT-DV processing is performed using a digital lock-in detection technique implemented on a graphics processing unit (GPU) in parallel with standard B-mode image processing. The system was deployed clinically and both anatomical and functional results were obtained with the system in cadavers and live subjects, including a patient with a stapes piston prosthesis. This was to our knowledge, the first report of OCT imaging of the entire middle ear volume and of middle ear OCT-DV in live subjects, as was recognized in [141].

3.5.1 OCT Engine Design

Our imaging system, shown diagrammatically in Figure 3.1 is built around the VT-DBRL akinetic swept laser (Insight Photonics Solutions, Model: SLE-101, central wavelength λ_0= 1550 nm, tuning bandwidth $\Delta\lambda$= 40 nm, nominal power P_0= 20 mW). This laser's fast sweeping (nominal sweep rate f_s = 100kHz) and extremely long coherence length (measured $z_c > 200$mm) makes imaging of the full depth of the human middle ear possible in real-time.

A Mach-Zehnder fiber interferometer was designed for use with this laser and a Thorlabs PDB-470C balanced detector. $\alpha = 90\%$ of the laser output is directed to the sample and a circulator directs the collected backscatter for 50:50 interference with the remaining 10% in the reference fiber. The measured reference arm power was 300μW at each detector element, which is adequate for shot-noise to theoretically dominate over receiver noise. With the laser configured to output P_0 = 13mW, after optical losses a total of 4.2 mW of power was incident on the sample. The interference signal is sampled at 12 bits and 400 MSPS on a high-speed data acquisition card (ATS9351, Alazar Technologies), with the acquisition card clocked and triggered directly from the laser's sample-clock and sweep-start signals, respectively. When configured for $f_l = 100$kLPS, a system of this configuration has a theoretical ideal sensitivity, derived from Equation 10 in [32] by setting $SNR = 1$, $\Delta t = {}^1/_{f_l}$, $S = P_0$, $\rho = 1{}^{\text{A}}/\text{w}$, and solving for R_s

$$S_i = -10 \log \left(\frac{2qf_l}{\rho P_0} \right) = 116\text{dB} \tag{3.1}$$

Easily meeting the sensitivity requirement $S_i > 97$dB from Chapter 2.

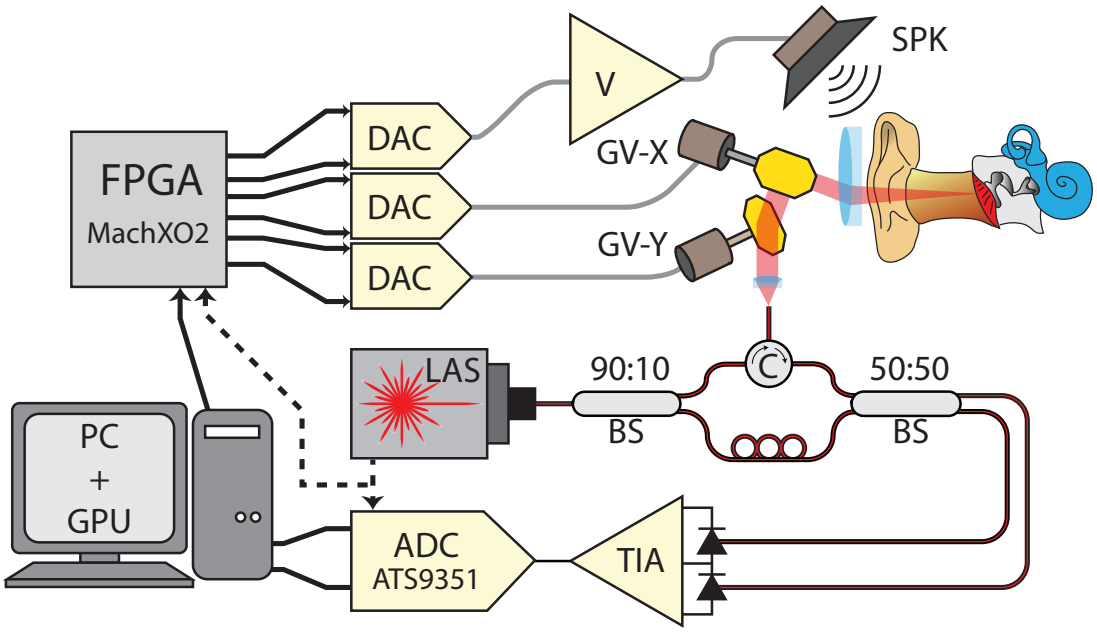

Figure 3.1: Diagram of the SS-OCT system designed for real-time, transtympanic human middle ear imaging *in vivo*. **FPGA** field programmable gate array, **DAC** digital-to-analog converter, **ADC** analog-to-digital converter, **LAS** wavelength swept laser, **TIA** trans-impedance amplifier, **V** voltage amplifier, **SPK** speaker, **GV** galvanometer mirror, **BS** fiber beam splitter, **PC** personal computer, **GPU** graphics processing unit.

3.5.2 Synchronization of the VT-DBRL

The SLE-101 operates in a free-running mode and cannot be triggered externally. During sweeping operation, the laser generates light of stepwise-linear increasing optical frequency in time, but containing a discrete number of brief mode-hopping events during which the laser behaves unpredictably. Since the timing of these events is highly repeatable from sweep-to-sweep and the affected time-points can be identified during calibration, the corresponding invalid data samples can be removed from the collected interferograms and the piece-wise segments of the desired linear sweep can be "stitched" together [137] to produce an, approximately, linear-in-optical-frequency sweep. This circumvents the need for re-sampling of the measured spectral interferogram prior to Fourier transformation, as is required in SD-OCT where conventional spectrometer designs produce approximately linear-in-wavelength measurements that require interpolation. This stitching process is described in great detail in [137] and is not reproduced here.

To maintain phase locking between the laser frequency-sweeping, the beam-scanning optics and the generation of the acoustic tone stimulus needed to excite a physiological response in the ear, we generated drive signals for the speaker and scanning mirrors using a set of digital-to-analog converters controlled by a field-programmable-gate-array (FPGA, MachXO2 by Lattice Semiconductor) that is clocked directly by the sweep-start signal output of the VT-DBRL. A custom printed circuit board with custom firmware and serial communication to the host computer was designed for this purpose (a descendant of which exists at the heart of the current version of the system described briefly in Chapter 5!). This approach provides system-wide synchrony and avoids timing errors that could arise with the invalid, mode-hopping sample points of the VT-DBRL. The laser's $f_s \approx 100$kHz sweep rate is sufficiently fast for adequate sampling of acoustic tones at any frequency in the human range of audibility (20Hz to 20kHz).

Because of the presence of invalid points in the VT-DBRL sweep, more samples must always be collected than will ultimately be used to form an A-line. As a result in this system, the actual sweep rate, f_s, was always reduced by the fraction of invalid samples in a particular calibration run. This time-scaling increased with sweep-rate as larger fractions of the sweep were spent in invalid states. This effect is captured

by the VT-DBRL's duty cycle specification in [137]. Because the laser sweeping controlled all timing in the system, the A-line-rate, f_l, was always reduced by this same factor. The same effect also had implications for frequency accuracy in OCT-DV measurements. While the system's architecture ensured synchronization of the acoustic stimulation's phase accumulation-in-time to the VT-DBRL, the byproduct of this synchrony was calibration dependent frequency scaling of f_a, the absolute frequency of the acoustic stimulus tone used to excite the ear. In the two SLE-101 units we had available in this work, we observed typical f_l and f_a reductions of 11% and 18% when operating at full speed. Additionally, in order to guarantee reliable sweep trigger recognition by the ATS-9351, 256 sweep points were ignored at the end of each sweep, artificially reducing the duty cycle of the laser. While this had no effect on f_l or f_a, it did reduce the number of useful sample points in the measured spectral interferograms, and represented a larger fraction of the total sweep at higher sweep-rates as well.

For simplicity in what follows we ignore these effects and give the nominal values of f_s, f_l, f_r, and f_a that would be obtained if all the samples in the sweep were valid. In reality, though, these parameters all change from one calibration run to the next and are always less than their nominal values.

3.5.3 Extraction of Doppler Vibrographic Information

In SS-OCT of biological tissue, the measured optical phase ψ at any location in the sample is random, owing to the random micro-structure of the sample. In this context, ψ refers to the angle of the complex-valued A-line obtained through DFT of the measured spectral interferogram. Although random, when the sample is set into periodic motion at an acoustic frequency f_a, the phase at that location oscillates periodically about the value it has when the sample is stationary. Neglecting noise, the optical phase measured at time t, as a function of axial depth, z, is described by:

$$\psi\left(z,t,f_a\right)=\frac{4\pi A(z,f_a)}{\lambda_0}\sin\left[2\pi f_a t+\phi\left(z,f_a\right)\right]+\psi_0\left(z\right) \tag{3.2}$$

where $A(z,f_a)$ is the displacement amplitude of acoustic vibration at frequency f_a, $\phi(z,f_a)$ is the acoustic phase shift of the reflector at f_a, and $\psi_0\left(z\right)$ is the optical phase

that would be measured with the sample at rest, all of which are functions of axial depth.

If it can be assumed that motion associated with the acoustic stimulus occurs on time scales much longer than the sweep time of the laser, then all structures are approximately stationary during each sweep and approximately no phase change occurs over the sweep time. Under this assumption, time t in Equation 3.2 can be discretized into the number i of sweeps that have elapsed since $t = 0$. We index M individual data frames (*i.e.* collections of small numbers of A-lines) by m and each of the N A-lines within each frame by n. In this scenario, a total of $M \times N$ A-lines will contribute to the overall OCT-DV measurement. Each of the A-lines contains Z axial pixels, indexed by z. Considering the A-lines as an incoming stream, the index i of the current laser sweep is simply calculated by:

$$i = (n + mN) \tag{3.3}$$

The amount of acoustic phase accumulated between two successive laser sweeps is, in radians:

$$\Delta\phi = 2\pi \frac{f_a}{f_s} \tag{3.4}$$

And so the total acoustic phase accumulated since the measurement began at time $t = 0$, $i = 0$, or $(n, m) = (0, 0)$ can be written:

$$\phi(t) = 2\pi f_a t \tag{3.5}$$

$$\phi_i = 2\pi f_a \frac{i}{f_s} \tag{3.6}$$

$$\phi_{nm} = 2\pi \frac{f_a}{f_s} (n + mN) \tag{3.7}$$

Substituting in to Equation 3.2, the measured optical phase, *i.e.* the phase of the DFT of the spectral interferogram of a vibrating reflector located at pixel z of A-line at indices n, m is therefore given by:

$$\psi_{nmz} = \frac{4\pi A\left(z, f_a\right)}{\lambda_0} \sin\left[2\pi \frac{f_a}{f_s}(n + mN) + \phi\left(z, f_a\right)\right] + \psi_0\left(z\right) \tag{3.8}$$

$A(z, f_a)$ and $\phi(z, f_a)$ represent the magnitude and phase of the steady-state vibrational response of the pixels along z. Both are of diagnostic significance for middle ear structures, and the response at the frequency of interest can be extracted from the measured optical phase data by cross-correlating ψ_{nmz} with a phasor oscillating at the normalized frequency f_a/f_s, *i.e.* $e^{j\phi_{nm}}$. They can be estimated from the following:

$$A(z, f_a)\, e^{j\phi(z,f_a)} = \frac{\lambda_0}{4\pi} \frac{1}{NM} \sum_{m=0}^{M-1} \sum_{n=0}^{N-1} e^{j2\pi \frac{f_a}{f_s}(n+mN)} \psi_{nmz} \tag{3.9}$$

Equation 3.9 is well suited for evaluation in parallel on a GPU. This digital lock-in approach can be used for arbitrarily long continuous averaging of the OCT-DV data across m in real-time, providing arbitrarily narrow effective detection bandwidth (*i.e.* by making M large and allowing many frames to contribute to the measurement). Because OCT-DV measurements use the same interferogram data as is used to generate B-mode images, the processing approach described here is amenable to real-time, simultaneous OCT-DV and B-mode imaging. Equation 3.9 is equivalent to the calculation of the single frequency coefficient of interest in an $N \times M$-point DFT along i, however with the calculation broken into sums across multiple dimensions to provide an opportunity to operate on smaller portions of the data, and to reduce the amount of calculations necessary to extract the OCT-DV signal of interest, discussed further in Section 3.7.

3.5.4 Real-Time Acceleration on a Graphics Processing Unit

GPU acceleration is widely used to accelerate OCT B-mode data, for example in [142, 143], but to our knowledge this work represented the first demonstration of GPU-accelerated real-time OCT-DV processing. We implemented the processing in NVidia's parallel programming platform, the Compute Unified Device Architecture (CUDA) which allows arrays of thousands of threads of execution (called a *grid* in CUDA) to execute simultaneously, providing a massive speed-up for appropriately formulated, highly parallel algorithms. In general, processing throughput with CUDA can be limited either by the number of operations being carried out or by the memory bandwidth of the device, *i.e.* the device's ability to read and write data to and from its own internal memory. Execution speed-up is achieved by identifying and leveraging

the parallelism in the problem, by minimization of redundancy, and through carefully orchestrated memory access, *e.g.* coalescing logically adjacent threads in the grid to access physically adjacent memory locations simultaneously. We now describe the logical implementation of our CUDA OCT-DV processing kernels.

Pre-Discrete-Fourier-Transform Processing

Our processing pipeline incorporated a normalization stage that can be used to flatten systematic amplitude ripple due to wavelength-dependent transmission of optical components and non-constant sweep profiles by scaling the collected interferograms by a pre-measured amplitude profile. This normalization can be helpful for suppressing unwanted broadening of the axial point-spread function (PSF) due to amplitude errors in the interferogram. Previously demonstrated numerical dispersion compensation capabilities [144] have also been incorporated that apply a complex multiplication vector of phase correction factors to the interferogram. This phase vector can be made to conjugate unwanted wavelength-dependent phase accumulations between the two arms of the interferometer that arise due to dispersion imbalance, and can prevent unwanted broadening of the PSF. Following stitching, these normalizations are applied to the measured interference pattern, and the intermediate result is then multiplied by a Hanning window function to control DNR and PSF width in the image prior to calculating the DFT. Since the normalization steps (ripple-rejection, dispersion-compensation, windowing) are all multiplicative in nature, by associativity, they could be pre-multiplied into a single complex normalization vector and stored in the GPU's constant memory.

These processing steps can be applied efficiently by grouping them into a single kernel of execution to minimize memory accesses and by structuring the CUDA grid of threads to maximize coalesced memory access. Since the VT-DBR's raw interferograms must first be stitched to eliminate invalid data in a way that depends on the laser's most recent calibration, the unpredictable pattern of memory accesses prevents perfectly coalesced reading of the raw interference pattern into the grid. However, since invalid data tends to be sparsely distributed with each sweep consisting of long sections of valid points interspersed with short blocks of invalid ones, sufficient data locality remains to get significant speed improvement through coalescing.

In CUDA we implemented a 1D grid of threads where each thread corresponds to a single valid point in the laser sweep, as shown diagrammatically in Figure 3.2A. When operating at maximum speed, our system acquires interferograms containing 4000 valid samples over $\Delta\lambda$, and so uses a grid of 4000 threads to execute the kernel. With the sweeps being sampled at 400MHz, this corresponds to a nominal sweep rate of $f_s = 100$kHz. Referring to Equation 3.9, each of the 4000 threads loops across and operates on N laser sweeps, *i.e.* data frames containing N interferograms are transferred and pre-processed on the GPU together, which is the amount of data required to carry out the inner sum of Equation 3.9. Writing of the result back to global memory is also coalesced and efficient.

This approach is compatible with using CUDA streams for concurrent data transfer and execution for pre-processing of multiple A-lines simultaneously. However, the Microsoft Windows drivers for our GPU (NVidia GTX660) lacked the ability to disable batched dispatching of asynchronous CUDA operations making it impossible to take full advantage of CUDA streams. Use of a newer GPU or the NVidia Linux driver would lift this limitation.

Following pre-processing, an optimized single-precision, complex-to-complex Fast Fourier Transform (FFT) is executed using the CUDA library, cuFFT.

Post-Discrete-Fourier-Transform Processing

Following the FFT, we simultaneously perform sweep averaging for SNR improvement in B-mode imaging and extraction of OCT-DV information through digital lock-in detection. Throughput is maximized by minimizing and coalescing global memory accesses, and by grouping B-mode averaging and Doppler processing into a single kernel of execution. This is achieved by creating a 2D grid of CUDA threads, each of which operates along i on a single N-wide data frame. While all of the threads need not be launched simultaneously, at the end of calculation $Z \times M$ threads have operated on the contributing data, as is shown in Figure 3.2B. Simultaneous transfer and execution can also be done using a separate processing stream for each column of threads along m with memory coalescing.

A key feature of this approach is that it enables a running calculation of the inner sums over n in Equation 3.9 as the A-lines become available, *i.e.* before the full

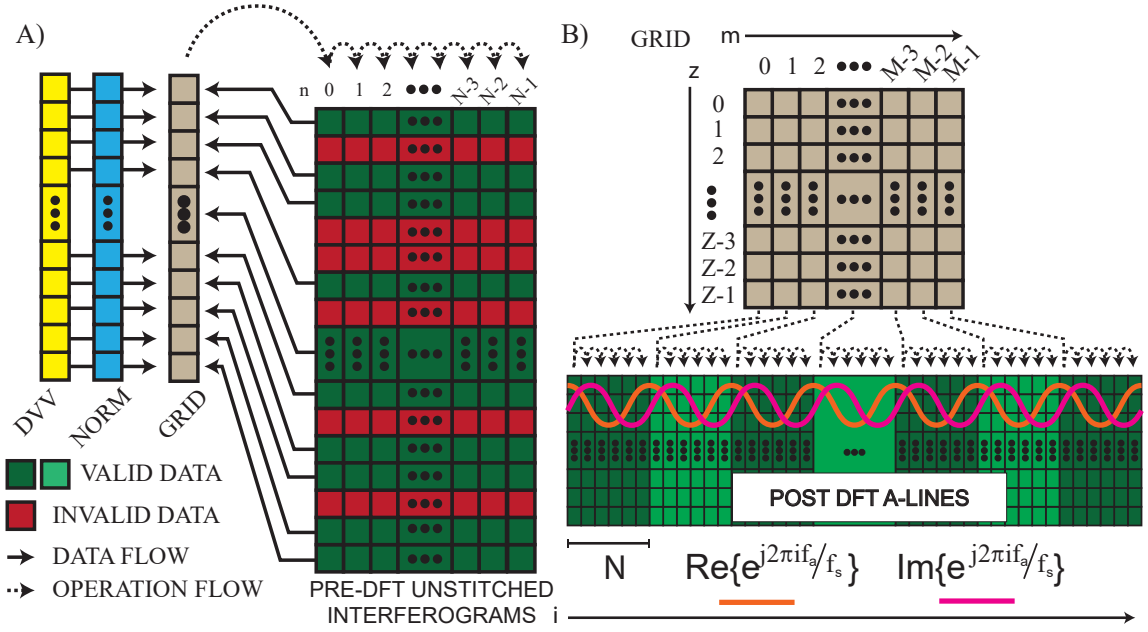

Figure 3.2: Conceptual diagram describing the memory and grid structure of the CUDA streams used for, A, pre- and, B, post-DFT processing the raw unstitched interferometric data. **DVV** data valid vector describing the pattern of invalid data to be ignored in the spectral interferograms, **NORM** complex-valued normalization vector used for ripple-rejection, dispersion compensation and windowing prior to discrete Fourier-transformation, **GRID** array of threads of executions running in parallel on the GPU during execution.

measurement is complete, or at all values of m simultaneously if the measurement is complete, until all M contributing data frames have been accumulated. After single-precision floating point calculation of the phase angles ψ_{nmz} and application of a non-iterative phase unwrapping algorithm, the phasor $e^{j\phi_{nm}}$ can be generated inside each thread from the grid parameters m, and loop counter n. In a pattern similar to that used during pre-processing, each thread loops across N sweeps and accumulates the B-mode average and OCT-DV results into efficiently accessed registers, and only the final results are written to global memory before transfer to the CPU. The subsequent sum over m operates on a greatly reduced amount of data. We carry out the sum over m, partially, on the GPU, and partially on the host CPU after transfer to host memory and the overall calculation can run continuously on a consumer grade NVidia GTX660 GPU with the SLE-101 configured for its maximum speed with imperceptible latency (4000-point wavelength sweeps at $f_s = 100$kHz), in parallel with standard B-Mode averaging calculations. It is the combination of the system's synchrony, the careful placement of measurement data into memory on the GPU, and the appropriate structuring of the CUDA threads to have correspondence between grid structure and the indices n and m that makes real-time B-mode and OCT-DV processing calculations fast and efficient.

The accuracy of the OCT-DV measurement system was determined by imaging the vibration of a B&K 8001 impedance head/accelerometer mounted on a B&K 4810 minishaker. The OCT-DV measurements agreed with the accelerometer reading to within 0.3dB over an acoustic frequency range from 250Hz to 8kHz.

3.5.5 Patient-Compatible Scanning Optics

We addressed the trade-offs between imaging probe types described in Section 3.4.4 by adopting a hybrid approach to the system's optical design. By imaging down the ear canal through standard 4 mm disposable plastic specula with a custom microscope mounted on the articulating arm of a Zeiss OPMI3 surgical microscope, we benefited from hands-free stability while avoiding the sterility problem. Our scanning microscope, depicted in Figure 3.3, consists of a pair of orthogonal galvanometer mirror scanners and a three-lens system of off-the-shelf achromatic doublets from Thorlabs. Lenses L1 (AC254-050) and L2 (AC508-100) operate roughly as a pupil relay, and L3

(AC254-060) as an objective. Adjustment of element separation D2 provides a means to vary the depth of best-focus within the sample. Adjustment of element separation D3 provides a means to adjust the maximum fan angle of the scan pattern. A wide FOV capturing the entire eardrum was achieved by placing a pupil image (*i.e.* an image of the center of rotation of the galvanometer mirrors) near the speculum tip. The system NA was kept small (≈ 0.022) in maintaining the required depth-of-field along the middle ear's axial length in accordance with the findings of Chapter 2.

A custom clamp was machined to allow changing of the speculum between patients. The sound stimulus was presented through a tube speaker (Etymotic Research, ER3A) and fed into the airspace within the speculum. The sound pressure level was monitored using a calibrated tube microphone (Etymotic Research, ER7C-Series B). During experiments, gain inline with the stimulus speaker was manually adjusted to reach $P_a = 100\text{dB}_{SPL}$ on the monitoring microphone.

3.6 Results

3.6.1 *Ex vivo* Imaging

A cadaveric human temporal bone, obtained fresh-frozen, was prepared for OCT-DV imaging to demonstrate the system's potential for applications in fundamental research in hearing physiology. We partially drilled away the ear canal to facilitate alignment of the system for imaging. With the system configured to excite and detect vibrations at $f_a = 625\text{Hz}$ (an acoustic period of 160 laser sweeps, duty-cycle scaled to an absolute frequency of $\approx 515\text{Hz}$), Figure 3.4A and 3.4B show 2D functional images of the middle ear response measured transtympanically with our system. In configuring the system for imaging a trade-off must be made between A-line density, Doppler sensitivity at each A-line, and total measurement time. The images in Figure 3.4 were collected with $N_l = 128$ A-lines per 2D B-mode image, and $N_l^2 = 16,384$ measurement points per 3D volume, arranged in an approximately square grid. There are $Z = 330$ pixels per A-line, corresponding to a maximum axial ranging distance of $z_D = 10\text{mm}$. Digital lock-in detection was applied over 128 acoustic cycles at each transverse coordinate, and processed with $N = 160$ and $M = 128$ in Equation 3.9. The measured vibration levels are consistent with those previously reported in LDV

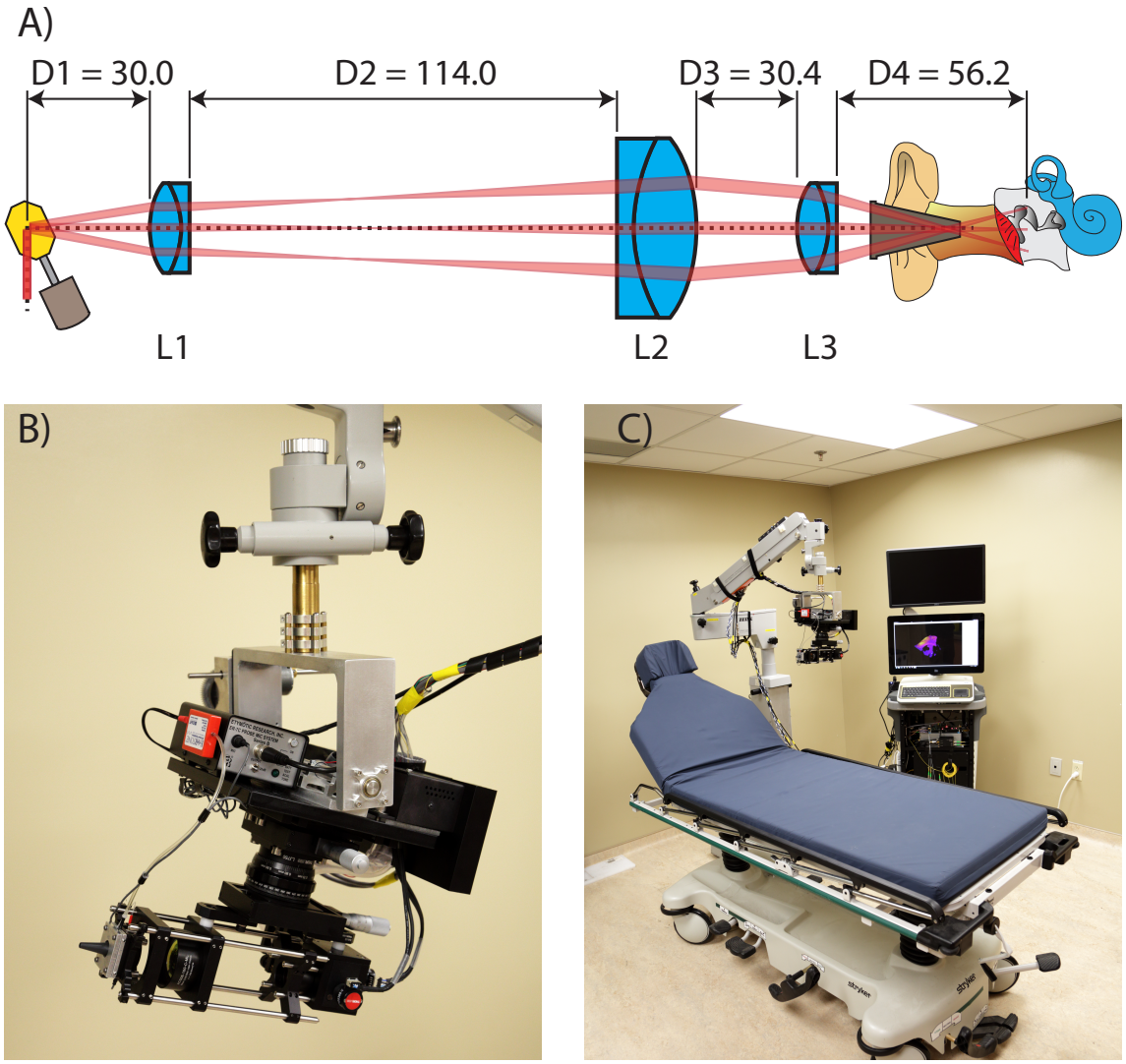

Figure 3.3: The SS-OCT system developed for *in vivo* transtympanic, full middle ear imaging. A, Optical layout with a pupil image located at the tip of the speculum to provide and wide field-of-view and access the full volume of interest in the middle ear. B, Closeup of the middle ear OCT scanning microscope used for imaging down the ear canal through a 4 mm otoscopic speculum and mounted to a surgical microscope arm. C, Complete in-clinic, real-time imaging setup. Units in A are in mm.

studies of temporal bones [39]. Figures 3.4C and 3.4D show a full 3D render of the excited response before and after digital removal of the TM by digial tympanotomy, respectively (see Supplementary File A). This volume scan was constructed from 128 stacked B-mode images taken over a total acquisition time of 70 minutes. Using the same dataset, we generated an animation of the complete vibration response of the ear with peak-to-peak displacements magnified by $4,000\times$ and slowed in time by $1,000\times$ shown in Supplementary File B. The relative phases of motion of all structures in the volume are preserved and accurately depicted. Since we can only measure the velocity component along the axis of the OCT beam, only motion along z is captured here.

3.6.2 *In vivo* Anatomical Imaging

Figure 3.6A shows the wide-field, long-range view of the middle ear as viewed through the TM from the intact ear canal, *in vivo*. The B-mode image contains $N_l = 256$ image lines, $Z = 330$ pixels per line, and was collected at $f_r = 20$FPS. Supplementary File C demonstrates the ability to observe the real-time macroscopic dynamics of the middle ear in 2D using video-rate B-mode OCT imaging. Between times 0:16s and 0:21s the outward bulge of the TM due to pressurization of the middle ear cavity by a Valsalva maneuver (pinching of the nose and popping of the ears) is clearly seen, as well as the subsequent depressurization that occurs when the subject swallows. 3D volume renders of the entire live middle ear can be seen in Figures 3.6B, 3.6C, and Supplementary File D.

To further support the proposed clinical utility of transtympanic middle ear anatomical imaging for post-operative tracking of middle ear prosthetics as described in Chapter 2, Figure 3.5 and Supplementary File E show anatomical images of a patient's middle ear acquired during a check-up visit following a stapedotomy surgery to treat otosclerosis, shown diagrammatically in Figure 3.5A [4]. Figure 3.5B shows a 3D render of the patient's ear with the crimp of the prosthetic appearing as a prominent bulge wrapped around the long process of the incus. Figures 3.5C and 3.5D show 2D transverse cross-sections through the patient's incus with the bone and titanium prosthetic having starkly different appearances. The crimp of the prosthesis lacks the speckle-filled multiple-scattering tails that are so prominent in images of the ossicles.

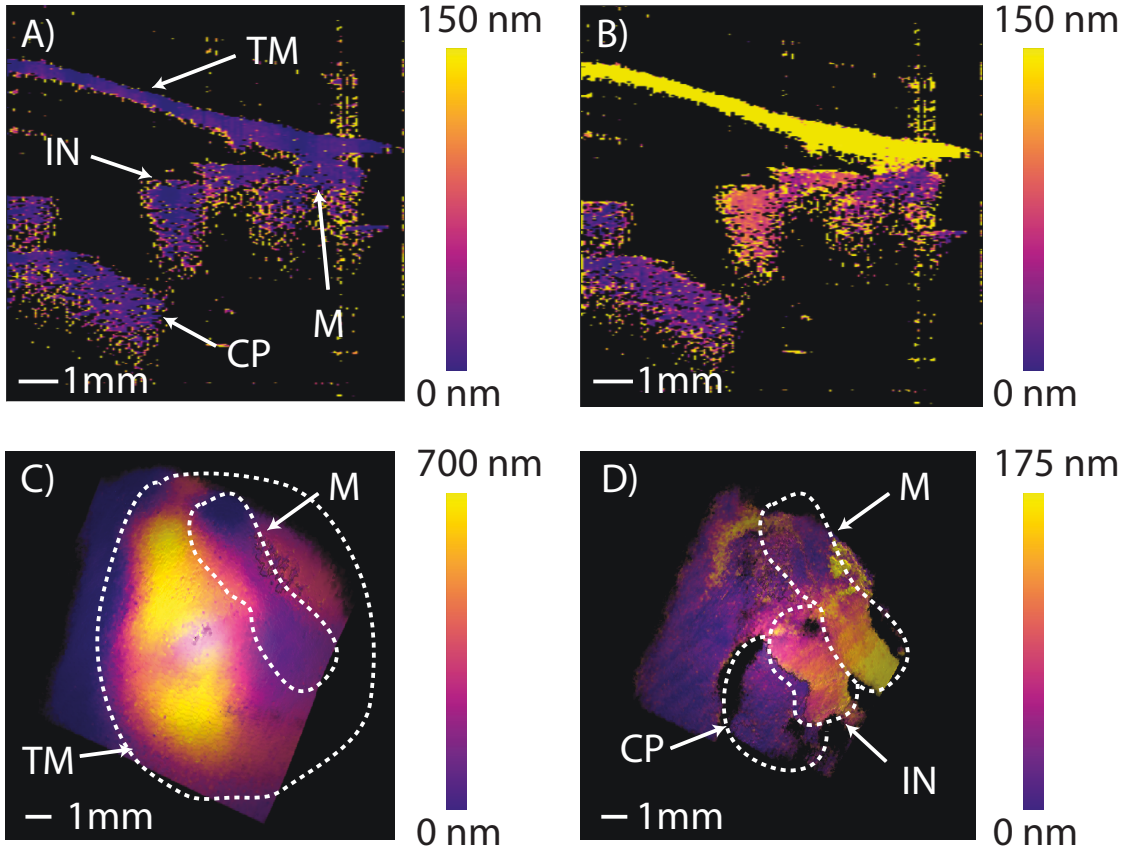

Figure 3.4: *Ex vivo* OCT-DV response in a cadaveric right ear at a nominal acoustic frequency of $f_a = 625$Hz (≈ 515Hz actual) showing a cross-sectional view of the ear's measured peak-to-peak vibrational response, A, without acoustic stimulus and, B, with stimulus applied at $100\text{dB}_{\text{SPL}}$. C and D show the color-mapped vibrational response to stimulus in 3D before and after digital removal of the TM. Supplementary File A shows a 3D rendered volume of the full vibrational response. Supplementary File B uses the same data to animate the middle ear's vibrational response. **TM** tympanic membrane, **M** malleus, **IN** incus, **CP** cochlear promontory.

In this patient the implant was well fixed-in-placed and had not migrated or eroded the incus, which answers a relevant clinical question for the clinician.

3.6.3 *In vivo* OCT-DV Measurements

When a live subject is imaged with OCT-DV, motion generated due to heartbeat, breathing and muscle movement induce phase disturbances in the collected interferograms that can dwarf the acoustic vibrations of interest by several orders of magnitude, and in a manner that varies from patient-to-patient and measurement-to-measurement. While these unwanted macroscopic motions are relatively slow and well-separated in frequency from the physiological response of interest at acoustic frequencies, when combined with the random micro-structure of the biological tissues, they produce phase noise that extends into the acoustic frequency band, significantly degrading OCT-DV sensitivity as compared to cadaver experiments.

Fortunately, because the ossicles move as rigid bodies at acoustic frequencies [145], it is possible to apply spatial averaging through the depth of an ossicle to improve SNR without compromising imaging speed. Using spatial averaging in the axial direction in combination with temporal averaging over a few seconds can typically produce a noise floor of $\approx$ 5nm *in vivo* with this system ($N \times M = 409,600$ with f_s nominally at 100kHz). This is measured by carrying out OCT-DV measurements with the sound stimulus disabled. Segmentation of the ossicles to implement spatial averaging is straightforward owing to the high contrast between the ossicles and the surrounding air, discussed further in Section 3.7.4.

The procedure we adopted for imaging live subjects is as follows. Using real-time B-mode imaging for navigation, we align the microscope in the patient's ear canal to obtain a preliminary assessment of the anatomy. We then capture a 3D volumetric scan of the ear and render it onscreen with the eardrum digitally removed to unveil the locations of the ossicles, nerves and tendons in the middle ear cavity. Based on the anatomical landmarks, individual lines are selected within the 3D volume for performing the OCT-DV measurements. We then collect OCT-DV data for $\approx 5s$ along each selected location through the anatomical structures of interest. The resulting vibration magnitude is displayed on the screen as a co-registered colour overlay on the B-mode image to provide immediate feedback to the clinician. If results

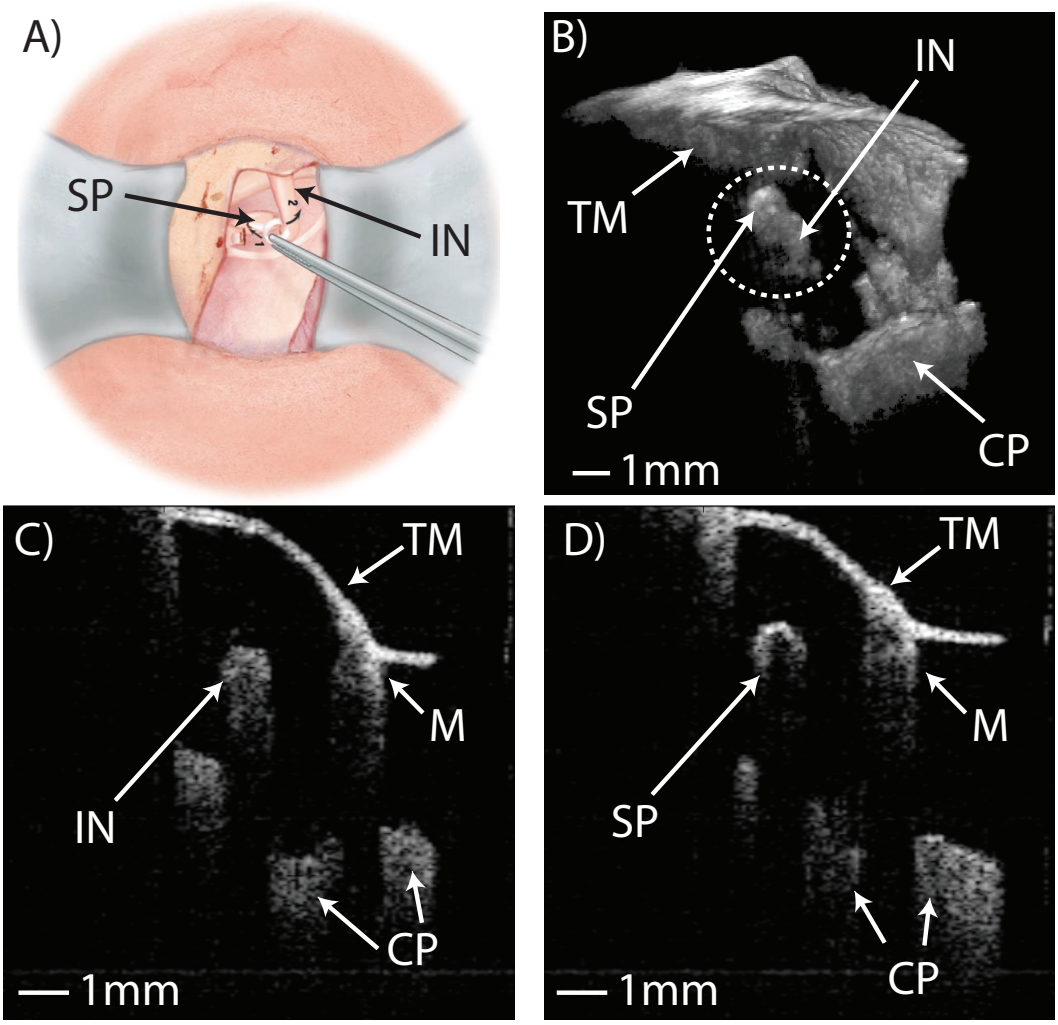

Figure 3.5: Images of stapes piston, *in vivo*. A, Illustration of the placement of a stapes piston prosthesis during stapedotomy surgery (taken from [4] with permission, illustration by Anne Johnson). B, *In vivo* 3D render of a patient's middle ear containing a stapes piston prosthethis, clearly showing the crimp of the piston around the long process of the incus (see Supplementary File E). C) and D) show real-time 2D B-mode images comparing the appearance of normal incus bone, characterized by gradual signal drop-off and multiple scattering, to the appearance of the titanium prosthesis, characterized by a single strong surface reflection. **TM** tympanic membrane, **IN** incus, **SP** stapes piston prosthesis, **CP** cochlear promontory, **M** malleus.

appear satisfactory as assessed by apparent smoothness of color, spatial averaging is applied in post-processing to improve the SNR of the displacement measurements for each measurement.

This procedure was applied to obtain the live patient OCT-DV data shown in Figure 3.6D-F. With the system configured to excite and detect vibrations at $f_a = 1250$Hz (an acoustic period of 80 laser sweeps, duty-cycle scaled to an absolute frequency of $\approx$ 1030Hz) we measured the displacement of the structures lying along the yellow line shown in Figures 3.6B and 3.6C in a 5s measurement ($N \times M = 409,600$). The colour-mapped Doppler results with and without a 100dB$_{\text{SPL}}$ stimulus applied are shown in Figures 3.6D and 3.6E. The measurement was repeated at seven sound pressure levels between 80dB$_{\text{SPL}}$ and 100dB$_{\text{SPL}}$ to produce the plot in Figure 3.6F. The slope of the data shows good agreement with the 20dB/decade reference line on the plot indicating that the response of the middle ear is linear over the measured range of amplitudes, in agreement with measurements performed in cadavers [146].

3.7 Discussion

3.7.1 Artifact-Free Dynamic Range

One of the disadvantages of using the VT-DBRL in the OCT engine is that it fails to meet the high dynamic-range requirement of $DNR > 60.5$dB identified in Chapter 2. Despite the VT-DBRL's built-in sweep linearity in optical frequency and the ability to tailor the optical power profile of the sweep, the achievable axial point-spread-function (PSF) has imperfections that impact image quality. The PSF side lobes described in [137] amount to ghosting in the OCT images that are particularly evident in lines containing strong back-scatter, since the side lobes clear the noise floor by the largest margin in those locations. As is evident in Fig. 5 of [137], the ghost artifact increases with axial ranging distance. While at very shallow depths $z < 5$mm one can achieve $DNR \approx 40$dB before the brightest reflector will generate artifacts that clear noise (as determined from the ratio of each main peak to the next largest side lobe), only $DNR < 30$dB is possible at $z = 10$mm when $f_s = 100$kHz. While only one side-lobe is apparent in Fig. 5 of [137], the PSF effectively has sharp-featured tails that produce artifacts in ear images like the example shown in Figure

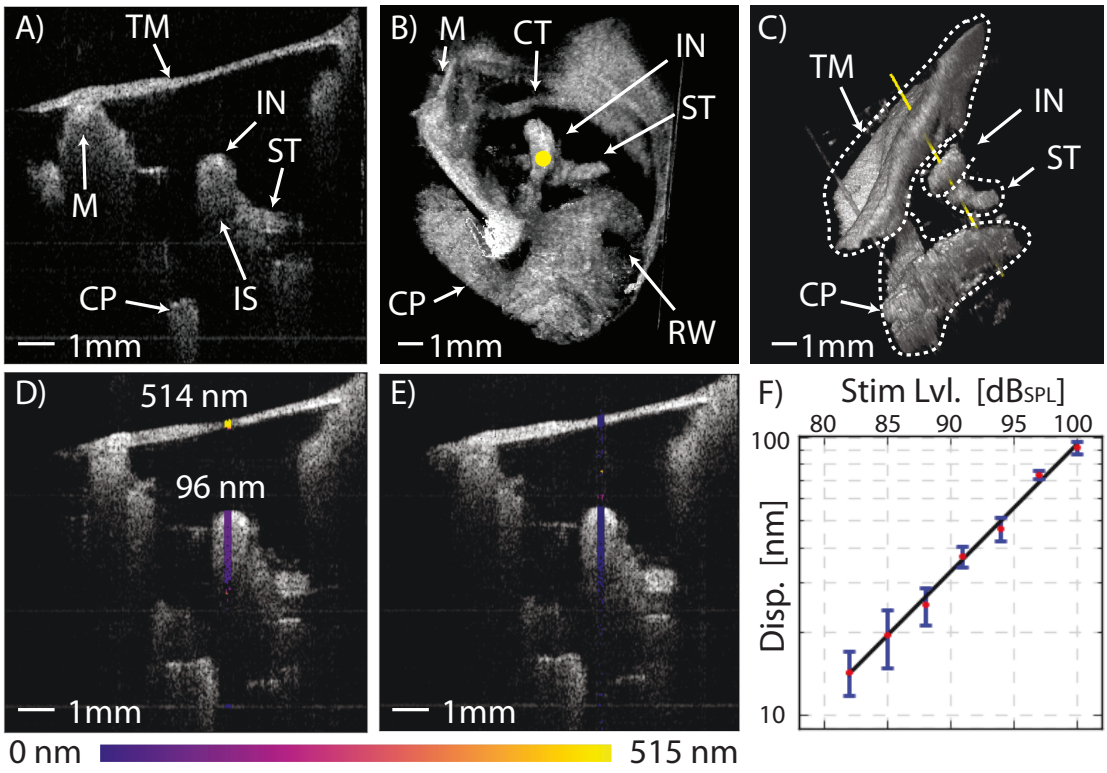

Figure 3.6: *In vivo* real-time OCT-DV measurement in a normal left ear's response to sound at 1030Hz. A shows a $10 \times 10\text{mm}^2$ 2D cross-section of the middle ear in the transverse plane. Supplementary File C shows the macroscopic changes to the ear anatomy during a Valsalva maneuver. B Shows a $10 \times 10 \times 10\text{mm}^3$ 3D volume render of the middle ear as seen from the perspective of the ear canal with the TM digitally removed (see Supplementary File D). C, shows the same volume from an inferior-posterior perspective with the TM in-place showing the axis of OCT-DV measurement along the yellow line passing through the incus at the stapedius tendon. Functional measurements of the TM and incus' peak-to-peak vibrational response at 1030Hz are shown in D with a $P_0 = 100\text{dB}_{SPL}$ tone applied to the ear and in E without stimulus. F, Peak-to-peak displacement of the incus versus presentation level showing good linearity from 80dB_{SPL} to $100\text{dB}_{\text{SPL}}$. Error bars represent $\pm$ one standard deviation of the response over the pixels along the axial length of the incus. **TM** tympanic membrane, **M** malleus, **IN** incus, **IS** incudostapedial joint, **ST** stapedius tendon, **CT** chorda tympani, **CP** cochlear promontory, **RW** round window.

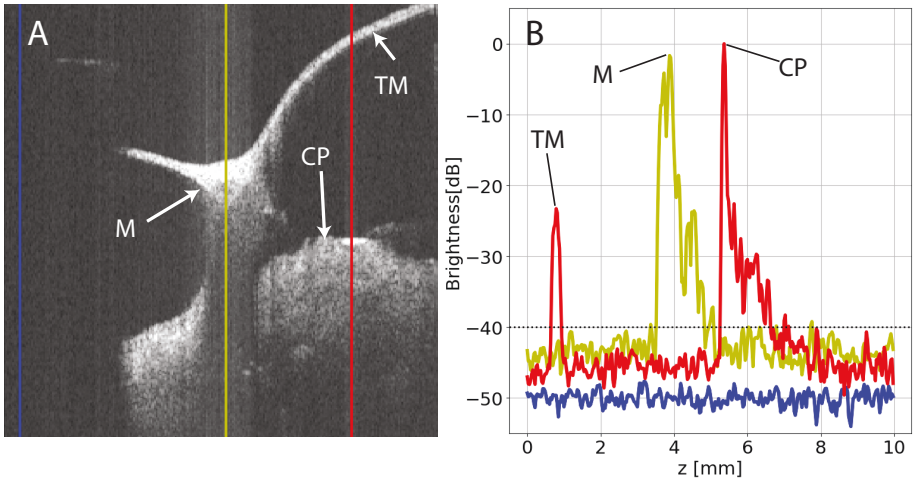

Figure 3.7: Image artifacts arising from imperfections in the PSF of the VT-DBRL. A, A 2D B-Mode image through the malleus. B, Selected A-lines from A corresponding by colour. Blue is a representative line of noise only, yellow intersects the malleus, and red intersects the cochlear promontory. In B, the dotted line shows where the black-threshold is set to display the images without the artifact apparent, and that in our system the quality of the PSF improved with increasing z in B. **TM** tympanic membrame, **M** malleus, **CP** cochlear promontory.

3.7, where the display range has been lowered to show the ghosting produced by the bright TM reflections relative to the random measurement noise. They are most severe at cross-sections that intersect the light reflex on the TM, where some degree of specular reflection occurs and the brightness is very high. Note that the desired SNR $>$ 47dB determined in Chapter 2 has been achieved at the ossicles relative to the noise, but the PSF tails degrade the effective contrast due to the elevated background level. Eliminating the 20.5dB DNR deficit relative to the requirement identified in Chapter 2 would eliminate the ghosting, but Figure 3.7 suggests that artifact-free $DNR >$ 55dB would be sufficient to remain noise-limited. It is worth recognizing that the ghost artifacts are temporally invariant, that they cannot be reduced by averaging, and that they currently impose a practical limit on contrast. To avoid their appearance in the images of this thesis, images are displayed with an elevated black-threshold level. The high contrast against air allows the images to remain qualitatively acceptable, but meeting the high DNR requirement would retain more information in the images.

3.7.2 Practical OCT-DV Sensitivity

Because, in our implementation, Doppler sensitivity is limited primarily by patient motion, the system could be improved by mitigating or eliminating its effects. Without a solution to this problem, the phase-stability breakthrough provided by the VT-DBRL can not fully be taken advantage of *in vivo*. Time-gating around heartbeat and/or breathing are both possible, but would add additional complicating steps to the imaging process. Improved vibration isolation, while technically feasible, is difficult to implement in a clinical setting and not likely to be effective with a live subject in the isolated system. The most recent published work made use of a bite plate to stabilize the patient's head during the measurements through a surgical microscope, with enough stability to carry out OCT-DV over 2D cross-sections, *in vivo* [84].

3.7.3 OCT-DV Processing Speed

Both VT-DBRL [137] and MEMS-VCSEL [147] based systems can offer phase stability high enough to allow Doppler imaging in architectures that are compatible with very fast A-line rates approaching 1MLPS. The GPU-based Doppler processing architecture presented here is readily scalable to higher speeds once faster phase-stable swept sources become available. We are currently working with VT-DBRL's that operate at f_s = 300kHz, although our total data throughput remains the same as the work of this chapter, at a fixed continuous sampling rate of 400MSPS. Currently available high-end GPUs could handle processing rates an order of magnitude higher than those needed for our current system.

3.7.4 Segmentation and Motion Artifact in OCT-DV

Figure 3.8A shows an example of the method by which a single numerical value is extracted from an OCT-DV measurement to quantify the overall displacement at a structure of interest. The approximate location of a structure is evident from the peaks present in the the A-line brightness data, and can be used to reference sample points in the OCT-DV data. Because the ossicles move as rigid bodies, all pixels within the structure have roughly the same displacement value. This amounts to local regions of brightness in the A-line corresponding to local regions of relatively

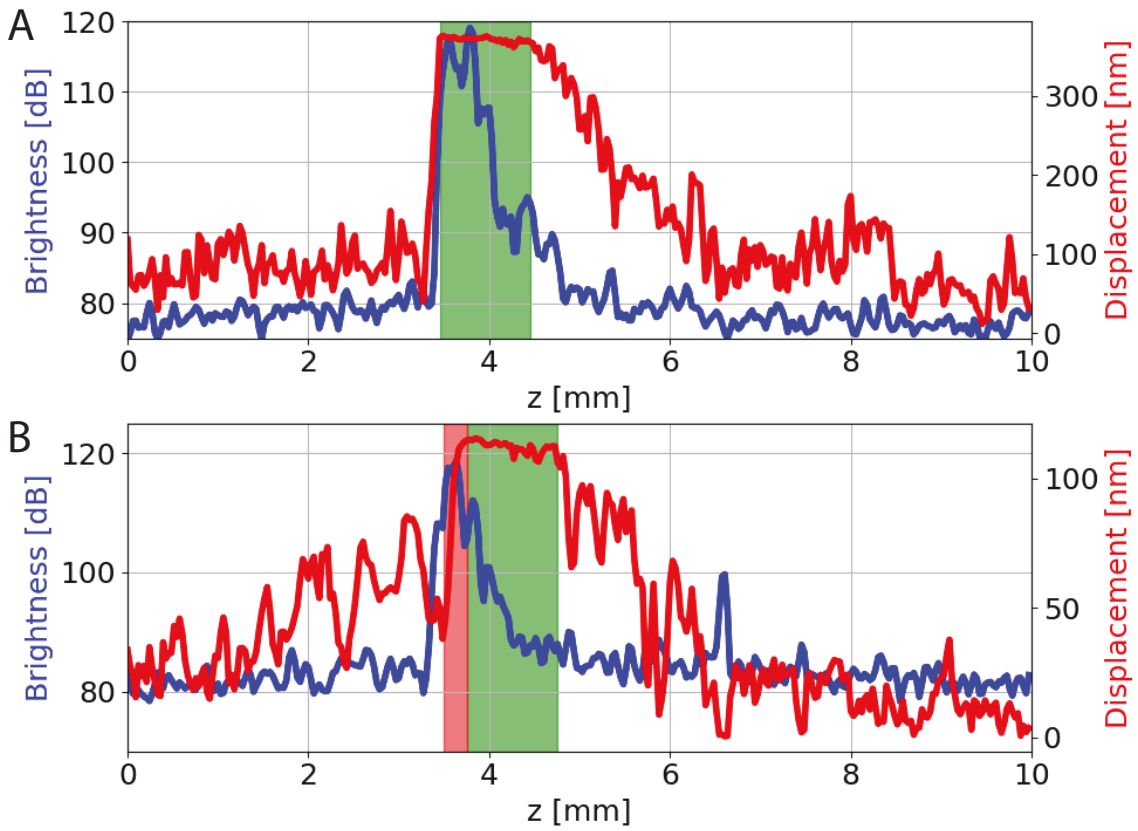

Figure 3.8: Example of the extraction of the OCT-DV signal showing both A-line magnitude and the extracted OCT-DV signal. A is taken in an exceptionally still patient while B is taken in a patient with a typical amount of motion during the measurement time. The green areas show the subjectively determined spatial averaging window, and the red shows areas that have been manually rejected due to motion artifact.

low variance within the OCT-DV trace, *i.e.* a flat region. In this work we manually selected, in post-processing, the region of interest over which to apply spatial averaging. This is as opposed to simply examining the smoothness of the displayed real-time color-map, which was used as an indicator of OCT-DV quality at measurement-time.

This is a process that could easily be automated, however there are technical problems that still require addressing. The most significant issue is that macro-scale motion artifact become problematic over the 5s OCT-DV measurement time. Patient motion during the measurement time creates inaccurate averaging. Fortunately, as long as the relative motion between the scanning optics and subject remains small compared to the size of the structure being probed, good averaging remains possible in the central mass of the structure. An example of a typical result with realistic

patient motion artifact is shown in Figure 3.8B, where the rolling off at the edge of the flat region is due to axial macro-motion during the measurement time. Selection of the optimal window-region to extract the local mean displacement amplitude remains somewhat subjective and is a source of variability between subjects and the individual conducting post-processing. While it is quite difficult to maintain small macro-motion compared to the thickness of the TM, it is relatively easy to maintain sufficiently low macro-motion as compared to the size of the ossicles.

A very plausible solution to this problem involves making the sum over m in Equation 3.9 more intelligent, either by only allowing the summing of pixels with significant brightness, *i.e.* to reject A-lines during times when the structure of interest has drifted off-target; by actively tracking axial motion of the subject during summation, *i.e.* by summing along m with intelligently varied z; or by using both of these techniques simultaneously. Active tracking in the transverse direction could also be beneficial. All of these mitigations fit very well with Equation 3.9 and the other processing discussions below in Section 3.7.7 regarding the benefits of having broken the extraction into many sub-calculations that are each very short in time. We are in the process of implementing an algorithm of this type. It has become increasingly clear that before OCT-DV could ever reach adoption, robust motion-artifact compensation and automatic measurement-quality-assessment will need to be developed.

3.7.5 Time-Scaling and Duty-Cycle Improvements

Since the work of this chapter has been completed, firmware for the VT-DBRL has been improved to enable greater control over the sweep parameters, enabling very good absolute frequency generation with this architecture with typically $< 1\%$ error. The 256 point-ignorance issue has also since been resolved via firmware upgrade that enables the insertion of a dead period between successive laser sweeps that give the acquisition electronics sufficient time to reset and recognize all sweep triggers. This still amounts to a reduction in duty-cycle, but it restores the ability to capture the full spectral content of the optical frequency sweep and corrects the calibration dependent time-scaling problem.

3.7.6 Patient Comfort and Practicality of the Microscope

While the system described in this chapter did enable *in vivo* imaging, alignment for the best possible FOV along the ear canal (i.e. to visualize the largest area of the TM as possible) still required great skill on the part of the operator. Volunteers who underwent imaging complained of tender ear canals following imaging, and the operator adjustments needed to position the microscope for optimal viewing of the full TM would often cause the subject pain. Overall, the basic form factor used in this chapter was not sufficiently usable for deployment in a clinical setting without continuous engineering support and two operators present in the room to keep the overall measurement session with volunteers acceptably fast, *i.e.* one operator at the GUI, and one operator with the mechanical controls for the system. These issues highlight the importance and need for workflow and ergonomic considerations in trying achieve utility; a factor often overlooked in the literature.

3.7.7 Processing Implications of Synchronization

The selection of the parameter N in Equation 3.9 is an important one. Phase unwrapping is a portion of the calculation that was not described in detail, above. It is an inherently serial operation since every value's required phase correction term depends on all previous values and their associated phase correction terms, making it a classic example of a problem poorly-suited to parallelization on a GPU. In the system described in this chapter, this problem was avoided by always choosing the period of the acoustic stimulus to be N sweeps in duration, i.e. $f_a = \frac{f_s}{N}$. Substituting this into Equation 3.9 gives:

$$A\left(z, f_a\right) e^{j\phi(z,f_a)} = \frac{\lambda_0}{4\pi} \frac{1}{NM} \sum_{m=0}^{M-1} \sum_{n=0}^{N-1} e^{j2\pi \frac{f_s/N}{f_s}(n+mN)} \psi_{nmz} \tag{3.10}$$

$$= \frac{\lambda_0}{4\pi} \frac{1}{NM} \sum_{m=0}^{M-1} \sum_{n=0}^{N-1} e^{j2\pi \frac{n}{N}} e^{j2\pi m} \psi_{nmz} \tag{3.11}$$

$$= \frac{\lambda_0}{4\pi} \frac{1}{NM} \sum_{m=0}^{M-1} \sum_{n=0}^{N-1} e^{j2\pi \frac{n}{N}} \psi_{nmz} \tag{3.12}$$

since $e^{j2\pi m} = 1$ for all m. This condition makes Equation 3.9 then appear more like the average of M N-point DFTs, than as a single $M \times N$ point DFT. And so, with reference to the post-DFT processing steps, each thread that operated over N sweeps also operated over a single acoustic period, exactly. During the unwrapping step, this meant that only local subsets of single acoustic periods were unwrapped, leaving residual phase steps between each of the total M data frames (*i.e.* allowing phase steps $> \pi$rad between acoustic periods). This takes advantage of the interesting fact that the spurious jumps that remain between acoustic periods have no impact on the overall OCT-DV calculation at the frequency of interest. This can be understood by, again, considering the calculation of Equation 3.9 to be the calculation of the single coefficient of the un-windowed $M \times N$-point DFT along i at frequency bin index M. The residual phase-steps from the partial phase-unwrapping are equivalent to a sum of top-hat functions of length N (and unpredictable amplitude). Noting the fact the $M \times N$-point DFT of a top-hat of length L is given by:

$$T(k) = \frac{\sin(\frac{\pi L k}{MN})}{L \sin(\frac{\pi k}{MN})} \tag{3.13}$$

we can see that for $L = N$, $T(k = M) = 0$ and so the residual phase-unwrapping errors do not contribute to the calculation. This is a key benefit to Equation 3.9 as compared to performing a single, long $M \times N$-point DFT type calculation; phase unwrapping can be broken down into several smaller parallelizable calculations on small groups of a whole periods of acoustics cycles.

This also works for fitting any integer number, P, of acoustic cycles inside N laser sweeps. A more generically useful condition for selection of intelligent pairs of f_a and N is given by:

$$f_a = f_s \frac{P}{N} \tag{3.14}$$

This alters Equation 3.12 to become:

$$A\left(z, f_a\right) e^{j\phi(z, f_a)} = \frac{\lambda_0}{4\pi} \frac{1}{NM} \sum_{m=0}^{M-1} \sum_{n=0}^{N-1} e^{j2\pi \frac{nP}{N}} \psi_{nmz} \tag{3.15}$$

In the published work, we always chose to use $P = 1$ and varied N to select the

acoustic frequency that satisfied Equation 3.14. Equation 3.15 is an even simpler calculation than 3.9 and can provide further speed-up. By the linearity of the DFT, there isn't a requirement that the inner sum of Equation 3.15 be carried out first, and the complex-multiplication could be carried out on pre-averaged phases along m to reduce the total number of complex multiplications required to N (instead of $M \times N$), which may be beneficial in long measurements. We have yet to implement this version of the algorithm as throughput is already sufficient for our maximum imaging speed, but it may be necessary in the future as data rates increase with advances in swept-source technology. In this case, the partial phase unwrapping simplification remains valid since from Equation 3.13, $T(k = PM) = 0$, for all integer P as well.

Additionally, we anticipate this breaking up of the calculation as being valuable in implementing active compensation of the motion artifact described in Section 3.7.4. That type of intelligent averaging would not be possible with a straight-forward full $M \times N$-point DFT based calculation.

The downside to this approach is that it prevents the use of $W \times N$-point windowing before carrying out the frequency analysis of the phase. Instead, only M individual N-point windows can be effectively be applied (although here we have not), which has implications for spectral resolution and dynamic range in the calculation. The underlying benefit of the careful phase-locking and integer frequency ratios is that it enables perfect placement of the acoustically induced phase modulations in the center of the frequency bins in the Doppler extraction calculation. This completely avoids any amplitude errors that could arise due to spectral leakage. Interestingly, this zero-spectral-leakage can only be fully realized at acoustic frequencies where there exists a whole number of acoustic cycles that occupy a whole number of laser sweeps, *i.e.* Equation 3.14, the same condition that enables partial phase unwrapping to be used!

3.7.8 Integrated Automatic Gain Control

A particular challenge encountered in imaging live patients was that variable degrees of acoustic seal were obtained in different ear canals, resulting in pressure variability in the acoustic stimulus applied to the ear. In this work, the goal was to maximally excite an acoustic response to get the best possible SNR in the OCT-DV measurement without inducing pain, and so a target pressure of $P_a = 100\text{dB}_{SPL}$ was used. The

manual adjustment of pressure levels proved impractically slow in live patients, and so the system described in this chapter was eventually equipped with an automatic gain control (AGC) module with a feedback loop implemented in a Labview VI that would regulate the pressure in the ear canal in a few hundred milliseconds. This practical enhancement has proven extremely valuable in achieving rapid patient throughput and should be incorporated into future OCT-DV systems for use in live patients.

3.8 Conclusions

In this chapter, we demonstrated a SS-OCT system for use in clinical middle ear imaging in live humans trans-tympanically. The use of the newly available akinetic VT-DBRL allowed for unprecedented imaging of the full lateral and axial extents of the human middle ear, for OCT-DV mapping of the ear's dynamic response to acoustic tones in cadavers, and for the first *in vivo* OCT-DV measurements in humans. When combined with the custom wide-field mounted microscope designed to accommodate the human ear canal, we presented the most complete trans-tympanic middle ear images at the time, including an *in vivo* image of a stapes piston prosthesis in-place on the long process of the incus. The presented system architecture incorporates scalable GPU acceleration of the OCT-DV calculations, which we have shown achieves sufficient throughput for continuous 100% duty processing at full-speed sweeping with the SLE-101 VT-DBRL on a consumer-grade NVidia GTX660 GPU at $f_l = 100$kLPS.

Chapter 4

Applying Optical Coherence Tomography Doppler Vibrography to Clinical Otology: Discriminating Stapes Fixation from Normal

Dan MacDougall,[a] Loran Morrison,[b] Christine Morrison,[b] David P Morris,[b] Manohar Bance,[a,b,c] Robert BA Adamson[a,b,d]

[a] School of Biomedical Engineering, Dalhousie University, Halifax NS, Canada

[b] Division of Otolaryngology Head and Neck Surgery, Department of Surgery, Dalhousie University, Halifax NS, Canada

[c] Clinical Neurosciences, Univeristy of Cambridge, Cambridge, United Kingdom

[d] Electrical and Computer Engineering Department, Dalhousie University, Halifax NS, Canada

4.1 Author Contribution Statement

D. MacDougall, R. Adamson and M. Bance conceived the experiments and analyses. L. Morrison, D. MacDougall and C. Morrison carried out imaging sessions with normal controls and patients. L. Morrison, D. Morris and M. Bance recruited patients and volounteers. D. MacDougall carried out the analysis of the imaging results and was the lead and corresponding author on the journal submission.

4.2 Preamble

This chapter is based on my third peer reviewed publication [148]. Its contents remain, largely, unaltered. However, introductory information that would duplicate the contents of Chapter 1 have been omitted or otherwise changed for conciseness. Some additional, unpublished experimental details have been opportunistically added, and some modifications have been made to lend context and render this document, as a whole, self-consistent in terminology and style. Specifically, the introductory section

has been altered to provide insight into the motivation and novelty for the work at the time the original manuscript was submitted for peer review, and to explain the work's fit into the overall story of my thesis; descriptions of pathologies and surgical interventions have been reduced, and the reader is directed to Section 1.2.2 for those details; and discussion points have been expanded and altered to better reflect insights that have been gleaned since the paper was published. A copyright transfer agreement with Wolters Kluwer Health requires that I state that this chapter represents a non-final version of an article published in final form in [148], and that a link to the *Otology and Neurotology* website be provided (https://journals.lww.com/otology-neurotology).

4.3 Abstract

Hypothesis: Ears with otosclerotic stapes fixation will exhibit lower-than-normal levels of ossicular mobility as measured by Optical Coherence Tomography Doppler Vibrometry (OCT-DV).

Background: OCT-DV measures the vibration of middle ear structures in response to sound non-invasively through the intact tympanic membrane. This allows, in particular, direct measurement of the vibration at the lenticular process of the incus which is expected to be lower in patients with otosclerotic stapes fixation.

Methods: OCT-DV was performed on ears presumptively diagnosed with stapes fixation (N=13) and a group of normal control ears (N=42). Displacement was measured at the umbo and the lenticular process of the incus in response to $f_a = 500$Hz and $f_a = 1000$Hz stimulus tones at a presentation levels of $P_a = 100\text{dB}_{SPL}$.

Main Outcome Measure: The ability to discriminate between groups was assessed using receiver operator characteristic analysis, with the main outcome measures being the area-under-curve (AUC) and the sensitivity and specificity.

Results: For the best condition tested (absolute displacements measured at the incus at $f_a = 500$Hz), the AUC was 0.998 and discriminated the otosclerotic from normal ears with a sensitivity/specificity of 1.00/0.98. One anomalous patient with surgically confirmed stapes fixation exhibited hypermobility at the umbo, possibly due to a partial ossicular discontinuity. Despite the high umbo mobility, this patient's stapes fixation was correctly discriminated based on the measured incus vibration levels.

Conclusions: OCT-DV is a promising tool for pre-operatively assessing ossicular

mobility non-invasively in the clinic. Our results suggest OCT-DV may also be useful in discriminating other ossicular pathologies that result in conductive hearing loss.

4.4 Introduction

4.4.1 Motivation

Despite the system described in Chapter 3 ultimately remaining challenging to use on live patients, it was sufficiently accommodating to apply OCT-DV to real pathologies and begin the process of validating the technique as a tool sensitive to information relevant to clinical decision making. The focus of my work began to shift towards greater interaction with clinicians and patients, and observing the way information is gathered and how it is disseminated into a treatment plan.

To reiterate, the ultimate goal for my work was to achieve clinical utility with OCT-DV, and eventually become a gold-standard tool for understanding the state of the middle ear. For any patient that proceeds to ossiculoplasty for ABG closure, the surgeon's goals are relatively simple; to achieve stable aeration of the middle ear, to ensure solid contact between the TM and oval window to conduct sound energy to the inner ear; and to make sure the ossicles (or their replacements) are free to vibrate with as little mass-loading as possible. It's the rationalization to proceed to surgery that is quite varied. One of the challenges we have faced, and continue to face, is that CHL patients seeking tertiary care in otology are quite varied in presentation. From my own personal observation, the reality faced in the clinic is that virtually no two surgery candidates are the same. There are innumerable combinations of symptoms and factors to consider including reported autophony, atelectatisis of the TM, TM thickening, tympanosclerosis, histories of trauma or otitis media, the patient's surgical history, intermittent ABG with Valsalva maneuvers, the presence or absence of Carhart's notch, confusing immittance and audiometric results, and family history. With the work of Chapter 3 complete, and with the OCT-DV tool made available to interesting and consenting patients, we found ourselves imaging subjects with what often seemed like very unique presentations, and often with symptoms where it would be difficult to intelligently hypothesize what signature in the OCT-DV data may exist for the unknown, underlying pathology. What was

needed to generate the first nugget of real clinical evidence that OCT-DV was of some practical use was a carefully selected patient group that could be readily recruited, a standard imaging protocol that could be applied to that patient group, and a sample of normal controls to be compared against.

We proceeded in a, perhaps, unorthodox manner by selecting a patient group where a skilled clinician is already quite effective at pre-operative diagnosis, and where there exists a very logical physiological signature that OCT-DV could detect: stapes fixation. The motivation for this chapter was to show that OCT-DV was sensitive to the specific dynamic abnormality in the ossicular chain, and not to show that OCT-DV can provide a diagnosis that the standard-of-care diagnostics cannot. The task of identifying and discriminating a patient group where otologists are currently ineffective at pre-operative diagnosis remains an ongoing effort. Aside from this work, there still exists no other examples in the literature of OCT-DV being applied to real ossicular pathologies in the clinic, *in vivo*.

4.4.2 Optical Vibrometry and Stapes Fixation

Recall from Section 1.3.1 that unless there exists a perforation or the TM is surgically lifted, laser Doppler vibrometry (LDV) in the ear is limited in that it can only perform surface measurements on the TM. This means that changes in the dynamics of the middle ear's deeper structures have to be inferred from changes observed on the TM's external surface. Typically such measurements are performed at or near the umbo, with the TM's point of maximum optical reflectance, often called the light reflex, used as a surrogate measurement location [3]. The light reflex is close to, but not always on, the umbo and poses a potential source of variability in the measurement.

LDV's potential applicability and utility in diagnostic otology was rigorously investigated in a series of clinical studies [3, 26, 55]. These investigations showed that ossicular discontinuities and malleus fixation can be detected through umbo vibration measurements. However, stapes fixation was shown to only subtly alter the response seen at the umbo by -5dB, compared to -30dB at the site of fixation (from Fig. 8 in [58]). This is close to the variation seen in normal hearing (one standard deviation is ≈ 6dB from Fig. 3 in [54]) and illustrates why the identification of stapes fixation

is difficult without additional audiometric data. It can be attributed to the compliance of the ossicular chain, and is consistent with the intuitive notion that vibration reduction due to fixation is greatest near to the site of the pathology [45, 58].

Since OCT-DV is not restricted to measurements on the surface of the TM and is able to measure the vibration of any optically reflecting structure in the middle ear visible through the aperture of the ear canal, it has the potential to directly measure the vibration at the site of stapes fixation, and so hypo-mobility at the stapes need not be inferred from umbo measurements. The information provided by such a measurement could be useful in adding confidence to diagnosis, guiding surgical planning, informing patients of their treatment options and the associated risks, and has the potential to differentiate various pathologies in complicated cases of conductive hearing loss.

In the literature, work that preceded that of this chapter and where OCT was applied to clinical otology included a number of studies focusing on TM imaging, particularly for the diagnosis and classification of otitis media [71, 73, 78, 82]. In humans, OCT-DV had only previously been investigated for the diagnosis of middle ear disease in cadaveric temporal bone models [88, 113]. The only preceding *in vivo* OCT-DV was the work described in Chapter 3, and that was conducted in normal hearing subjects.

4.4.3 Diagnosing Otosclerosis Without Vibrometry

Otosclerosis is a primary bony disorder of the otic capsule that most commonly presents as a conductive hearing loss resulting from stapes footplate fixation. The clinical prevalence of otosclerosis is estimated to be 0.3%-0.38% [149]. Cases tend to pool by referral to tertiary otologists who, given a correct diagnosis, can restore auditory function through surgical intervention. Suspected cases are traditionally diagnosed by first ruling out the other, more obvious causes for conductive hearing loss. A history of middle ear infection, trauma, TM perforation or visible scarring seen on otoscopy are all suggestive of alternative causes of conductive hearing loss.

The typical clinical narrative that supports proceeding to exploratory tympanotomy and ossiculoplasty includes a history of progressive conductive hearing loss, normal otoscopy, supporting audiologic findings, the presence of a positive family

history, and sometimes CT imaging, although there are even cases of otosclerosis without stapes fixation [150]. High resolution CT of the temporal bone has been reported to have particularly poor sensitivity to fixations of the ossicles (in [2], CT determined 37.9% false negative congenital malformations, and 62.8% of those were associated with fixations). Otosclerosis is not generally apparent in conventional 226 Hz tympanograms. High frequency and multi-frequency immittance measurement techniques have shown mixed results in diagnosing otosclerosis with positive likelihood ratios from 1.3 to 4.4, a range that spans from uninformative to suggestive [151]. The ability of tympanometric techniques to detect otosclerosis is fundamentally limited by the compliance of the TM and components of the ossicular chain lateral to the stapes, making them largely insensitive to fixation at the stapes [58]. Pure tone audiometry, and, in particular, a narrowing of the air bone gap at 2000Hz, referred to as Carhart's notch, is found in 73% of patients with otosclerosis, but is also found in patients with otitis media, tympanosclerosis and other diseases, making it far from pathognomonic [152]. Other work has suggested the presence of Carhart's notch is an outright poor predictor of stapes fixation [22].

4.5 Methods

In this chapter, we show in a group of patients with a presumptive clinical diagnosis of otosclerosis, that the application of OCT-DV is sensitive to the expected reduced vibration of the stapes due to its pathological fixation. With these measurements, we are able to discriminate this group of patients from a group of healthy normal controls.

4.5.1 Subject Recruitment

All procedures were performed in accordance with a protocol approved by the Nova Scotia Health Authority Research Ethics Board (REB FILE No.1019922, Protocol Title: Optical Coherence of the Middle Ear, PI – Rob Adamson) and with the Helsinki Declaration (JAMA 2000;284:3043–3049). For normal control subjects, conductive hearing loss was ruled out by performing air conduction audiometry using the SHOEBOX QuickTest Audiogram (Clearwater Clinical). Tympanometry and ipsilateral acoustic reflex tests were also obtained using a TympStar tympanometer (GSI). Both

ears of normal control subjects were included unless image quality in the ear was too poor to adequately visualize the lenticular process of the incus, or if hearing thresholds were $> 10\text{dB}_{HL}$. A total of N=23 normal control subjects were recruited in the study, providing 45 eligible ears. For the otosclerosis patient population, individuals were identified following a presumptive diagnosis of otosclerosis by the referring otologist at a scheduled clinic visit. This presumptive diagnosis was made based on compelling clinical evidence. Factors considered significant in contributing to this diagnosis included normal otoscopic examination, the presence of family members with a proven surgical diagnosis of otosclerosis, and the absence of tympanometric findings that would suggest a more obvious reason for the conductive loss such as ossicular discontinuity or middle ear effusion. All included patients were offered surgical treatment. Patients were only included if they had an audiometric air-bone gap (ABG) $\geq$ 15dB at either 500Hz or 1000Hz. Audiogram results, including ABG and tympanometry, were collected from the patients' medical chart and were not repeated for study purposes. A total of 14 patients were recruited in the study, providing 18 eligible ears. Ears of patients or normal control subjects were excluded from the analysis if the lenticular process of the incus could not be seen in the OCT imaging procedure due, for instance, to a very thick TM, a narrow or stenotic external meatus that made the imaging procedure painful, an inability of the patient to keep their head still during imaging, or obstruction to imaging from debris or impacted wax in the ear canal.

4.5.2 Optical Coherence Tomography Doppler Vibrography

The device described in this manuscript is a non-significant risk investigational device and has not been approved for human use by the US Food and Drug Administration or any other national regulatory agency. The system described in Chapter 3 was configured with 4mW of light incident on the eardrum. The weakly-focused laser beam ($\lambda_0 = 1550$nm) was guided down the patient's ear canal through a rigidly mounted speculum. Light backscattered from the TM and ossicles along the beam path was measured using optical interferometry and processed into cross-sectional images of the middle ear as shown in Figures 4.1D and 4.1E. Such images were acquired at a real-time rate of $f_r = 20$FPS with each frame consisting of $N_l =$

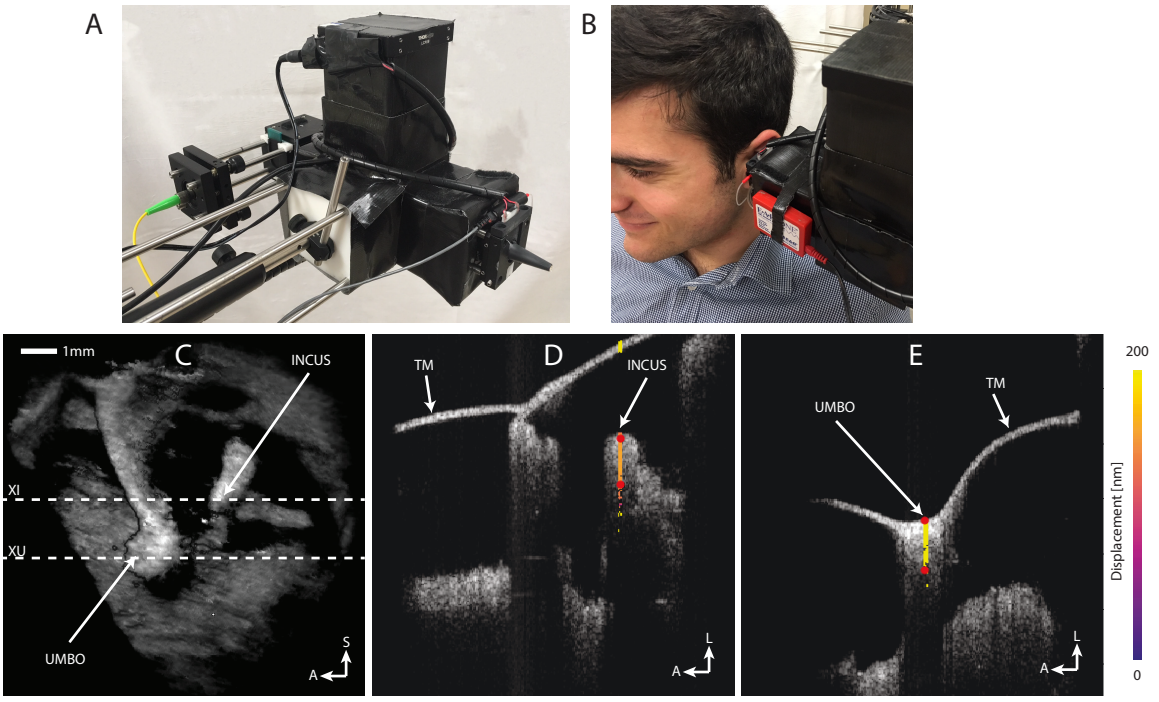

Figure 4.1: Experimental setup and representative sample of images produced from a typical session for imaging patient volounteers and normal controls. A, The mounted OCT-DV scanning head. B, The imaging system oriented along a volounteer's ear canal to visualize the TM and ossicles. C, A 3D rendering of a middle ear with the TM digitally removed via *digital tympanotomy* to reveal the ossicles and showing transverse cross-sectional cut-planes through the umbo and lenticular process of the incus. D, Cross-sectional image through the incus showing a color-mapped vibration measurement on the lenticular process of the incus. E, Cross-sectional imaging through the malleus showing a vibration measurement on the umbo. Averaging of the vibration amplitudes is done over the pixels located between red dots in D-E. **TM** tympanic membrane, **A** anterior anatomical direction **L** lateral anatomical direction, **S** superior anatomical direction, **XI** incus cross-section, **XU** umbo cross-section.

256 A-lines, and each line in the rendered image formed by averaging 20 individual interferograms acquired at $f_l = 100$kLPS.

4.5.3 System Improvements

The system used for this chapter differed from that in Chapter 3 in that it was equipped with an illumination source, and a part-time image sensor for en-face viewing of the TM during alignement of the optics to the system. This was to address the difficulties we encountered in trying to navigate the ear canal using real-time OCT alone. A visible light source was also integrated into the system to illuminate the TM

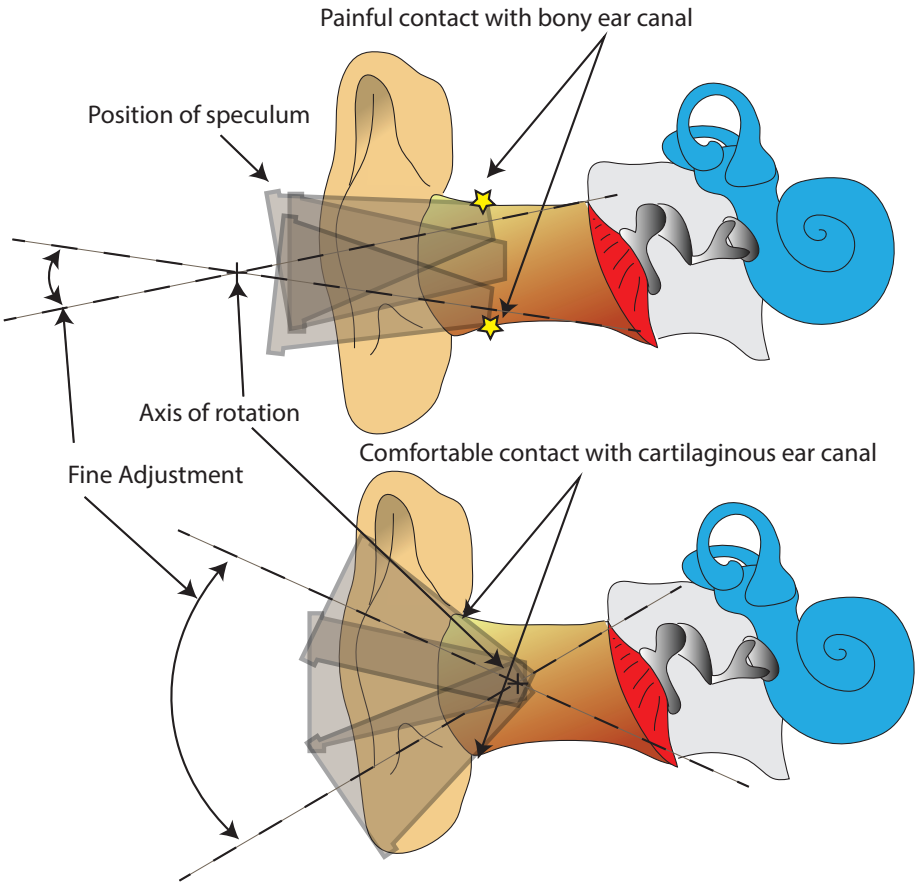

Figure 4.2: Mechanical adjustment setup of the microscope to reduce patient discomfort. At top, showing the mechanics of alignment of the microscope head to the ear canal from Chapter 3, which caused subject pain during adjustment. At bottom, the upgrade made to the fine alignment mechanics, as it was used in Chapter 4 to reduce subject discomfort.

in the, otherwise, dark ear canal.

The system was also mounted to the surgical microscope arm in a different fashion to reduce the discomfort patients would experience during physical manipulation of the microscope. Macroscopic positioning of the microscope was made by swinging the articulating arm, and fine adjustment to pitch and yaw were made using a group of geared mechanical knobs. The mounting of the microscope head was such that fine manipulations would cause the microscope to rotate about the tip of the speculum in the subjects ear canal, and greatly improved the subject discomfort problem encountered in Chapter 3. This configuration is described diagrammatically in Figure 4.2, and is similar to the way otoscopes are manipulated once inserted into the ear canal.

4.5.4 Imaging Procedure

To reiterate, when acoustic stimulus is presented during OCT-DV, the sound induced periodic motion of the TM and middle ear structures are what produce the measured optical phase shifts that are processed into vibration information. The simultaneous pure tone acoustic stimulus was presented to the ear with an ER3 insert earphone (Etymotics Research) and monitored using a modified ER7 tube microphone (Etymotics Research) through holes drilled into the assembly that held the ear speculum. Using the GPU accelerated real-time processing system described in Chapter 3, we extracted the amplitude motion at all pixels along the selected lines of interest. While, in principle, OCT-DV can penetrate the TM and measure dynamics at any point on the ossicular chain visible from the ear canal, in practice, the most distal part of the ossicular chain that can reliably be observed and imaged in most subjects was the lenticular process of the incus. In some patients the crus of the stapes, the oval window and the stapedius tendon are also clearly visible and could be potential targets for vibrometry, however their inaccessibility in the majority of patients renders these measurement locations of limited practical use.

Subjects being imaged were asked to sit in a chair positioned in front of the imaging microscope, and the microscope's rigidly mounted speculum was inserted into the ear canal (Figures 4.1A and 4.1B). The mechanical controls for fine positioning were first operated under camera guidance to maximize the amount of TM visible en-face. From then on, further alignment was performed under OCT B-mode image guidance to optimize the axial ranging distance, and to maximize the FOV in the real-time B-Mode image. Once a suitable orientation was obtained, a 3D volumetric image consisting of 256 transverse cross-sectional images spaced by 39μm was acquired in a $\approx$ 6s automatic acquisition (Figure 4.1C). The structures of interest within the middle ear were then identified in the volume rendering. Vibration measurements could then be made at the umbo and at the lenticular process of the incus while sequentially presenting pure tone stimuli at f_a = 500Hz and f_a = 1000Hz. The stimulus amplitude was P_a = 100dB$_{SPL}$ as measured at the speculum holder, and automatically regulated using the AGC Labview VI described in Section 3.7.8.

Using real-time OCT guidance, the operator would locate the umbo by scanning an approximately anatomical transverse cut-plane from the superior edge of the TM

and following the manubrium of the malleus to its inferior tip (location shown as XU in Figure 4.1C, and the corresponding 2D image shown in 4.1E). The lenticular process of the incus was then found by scanning the cut-plane superiorly from the umbo until the long process and stapedius tendon were simultaneously visible in the image (location shown as XI in Figure 4.1C, and the corresponding 2D image shown in 4.1D). In cases where the stapedius tendon was not visible, the inferior edge of the incus was used instead. At each of these two line locations, a 2s vibrometry measurement consisting of $M \times N = 204,800$ OCT interferograms was acquired for each stimulus. The OCT data was analyzed to obtain the complex vibration amplitude at each pixel. In post-processing, the complex vibration amplitudes of those pixels lying along the measured line and contained within the incus and umbo were manually identified and averaged together using the manual segmentation procedure described in Section 3.7.4. Vibration levels were consistent through the thickness of each structure as would be expected for rigid body motion (See Figure 4.1D and 4.1E).

4.6 Results

4.6.1 Sample Statistics

The otosclerosis subject group consisted of 14 patients (10 female, 4 male) and 18 eligible ears. Differences in the onset time of otosclerosis in the two ears of bilateral otosclerosis patients would tend to weaken any correlation in CHL (and hence, any correlations in the expected OCT-DV measurement) between ears at the time of measurement, and so we treated the two ears of bilateral patients as independent samples. The average age of the otosclerosis group was 50.2 years. Four of these ears were excluded due to poor quality imaging. In three of the four subjects we could not locate the incus and in the fourth the measurements were of a poor quality due to an operator error. Of the remaining 13 ears included in this study, all were offered the standard range of treatment options for otosclerosis (i.e. observation, auditory rehabilitation with a conventional hearing aid, and surgical exploration with a view to stapedotomy/stapetectomy). At $f_a = 500Hz$, these remaining ears had a range of ABG from 10dB to 70dB (mean: 34.2dB, standard deviation: 18.2dB). At $f_a = 1000$Hz, there was an ABG range from 15dB to 50dB (mean: 32.7dB,

Table 4.1: Statistical summary of peak-to-peak displacement measurements performed at the umbo and lenticular process of the incus in patients with presumptive otosclerosis and in normal controls using OCT-DV at a stimulus pressure of $P_a = 100\text{dB}_{SPL}$. 95% confidence intervals are indicated in square brackets. **M** sample mean, **SD** sample standard deviation.

	Umbo[nm]		Incus[nm]	
Group	500Hz	1000Hz	500Hz	1000Hz
Normal Control	M: 150 [130,170]	M: 150 [120,180]	M: 79 [68,92]	M: 70 [61,81]
	SD: 76	SD:85	SD:37	SD:36
Otosclerosis	M: 55 [38,82]	M: 107 [64,168]	M: 9.7 [7.5,12.6]	M: 17.9 [12.8,23.5]
	SD: 43	SD: 100	SD: 4.7	SD: 9.8

standard deviation: 12.8dB). Seven proceeded to surgery where fixation of the stapes was confirmed by manual palpation. Two ears were of subjects with contralateral otosclerosis that had previously been confirmed in surgery. The remaining 4 ears did not undergo surgery. The normal control subject group was composed of 23 subjects (9 female and 14 male) with 45 eligible ears. The average age of the otosclerosis group was 32.9 years. Three of the control ears were excluded due to poor imaging and an inability to locate the incus. The measured peak-to-peak displacement at the umbo and lenticular process of the incus for each sample group are summarized in Table 4.1, and their corresponding probability density functions are shown in Figure 4.3. All confidence intervals for the reported statistics were calculated using bootstrapping [153] (i.e. random resampling with replacement) with 1000 iterations. A Welch's T-test was used to show that the surgically confirmed patients were not significantly different from the patients who did not proceed to surgery ($p > 0.22$) and so the two groups were pooled in the analysis.

4.6.2 Discrimination Between Normal and Otosclerotic Ears

The ability of OCT-DV to discriminate between the otosclerosis and normal groups was quantified using a receiver-operating-characteristic (ROC) analysis and statistical bootstrapping, summarized in Table 4.2, and shown in Figure 4.4. In 1000 bootstrap iterations, the AUC was greater at 500Hz than at 1000Hz at both the umbo (difference in AUC=0.20, 95% CI [-0.017, 0.41]) and at the incus (difference in AUC=0.03, 95% CI [-0.0036,0.083]), although the difference was not significant at a 95% confidence level. This might be expected from the fact that the middle ear admittance due

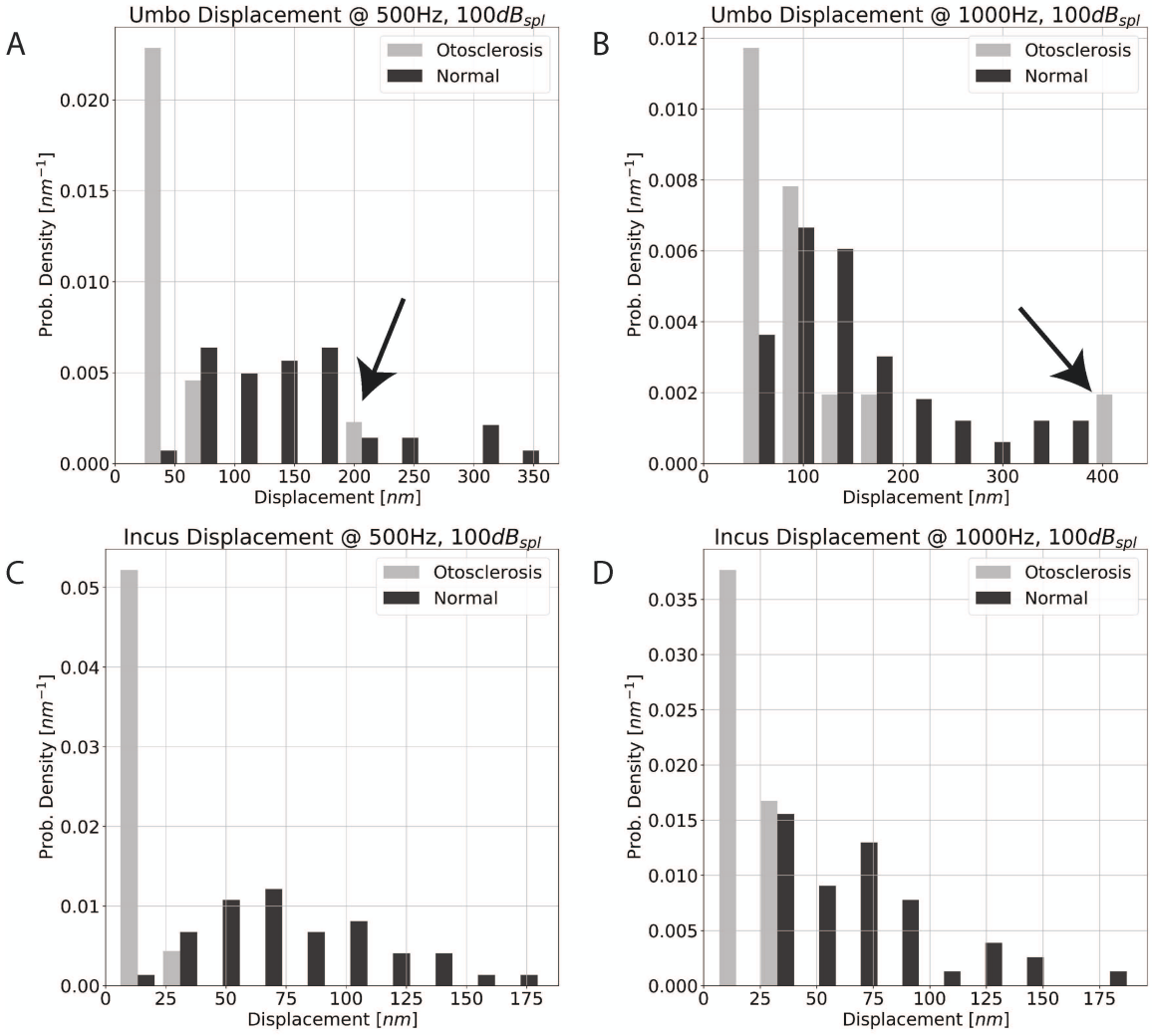

Figure 4.3: Sample distributions of measured vibrational response for the presumed otosclerotic and normal control groups. A, At the umbo with a stimulus frequency of 500Hz. B, At the umbo with a stimulus frequency of 1000Hz. C, At the incus with a stimulus frequency of 500Hz. D, At incus with a stimulus frequency of 1000Hz. Black arrows point to anomalous vibration observed at the umbo of patient 0163.

Table 4.2: Summary of ROC analysis for the discrimination of presumptive otosclerosis from normal controls using OCT-DV at the umbo and lenticular process of the incus at stimulus frequencies of 500Hz and 1000Hz. Optimal threshold is calculated as the threshold giving the maximum Youden J-index. 95% confidence intervals are indicated in square brackets. **AUC** area under ROC curves from Figure 4.4.

Location	Frequency	AUC	Optimal Threshold T_{opt}	Sensitivity@T_{opt}	Specificity@T_{opt}
Umbo	500Hz	0.91[0.78, 0.99]	72nm	0.92[0.77, 1.00]	0.88[0.79, 0.98]
	1000Hz	0.71[0.53, 0.86]	123nm	0.85[0.62, 1.00]	0.60[0.43, 0.74]
Incus	500Hz	0.998[0.989, 1.000]	24nm	1.00[1.00, 1.00]	0.98[0.93, 1.00]
	1000Hz	0.97[0.915, 1.000]	25nm	0.85[0.62, 1.00]	1.00[1.00, 1.00]

to compliance in the lateral part of the ossicular chain is lower at low frequencies. The result is consistent with previous studies showing that umbo vibration levels in otosclerosis patients diverged more strongly from normal levels at 500Hz than 1000Hz [3]. The AUC was also greater at the incus than at the umbo at both 500Hz (difference in AUC=0.088, 95% CI [0.0018,0.22]) and 1000Hz (difference in AUC=0.25, 95% CI [0.093, 0.45]). This is consistent with previous LDV studies in cadaveric temporal bones that showed that, due to the compliance of the ossicular chain, a fixation of the stapes has a greater effect on vibration at the incus than at the umbo [58]. The most discriminating measurement was at the lenticular process of the incus with a 500Hz stimulation frequency, achieving a sensitivity of 1.00 and specificity of 0.98 at the threshold value that maximizes Youdon's J-index, defined by:

$$J = sensitivity + specificity - 1 \tag{4.1}$$

4.7 Discussion

4.7.1 Study Limitations

The discrepancy in standard deviation at the incus between groups in Table 1 can be attributed to the measured vibration levels at the incus in the otosclerotic group being limited by the measurement noise floor of the system set by patient motion (typically $\approx$ 7nm in a 2s measurement). Given the mean displacement at the incus of 79.0nm at 500Hz in the normal group, and given the mean air-bone-gap of 35dB within the otosclerosis group, displacement levels on the order of 1nm would be expected

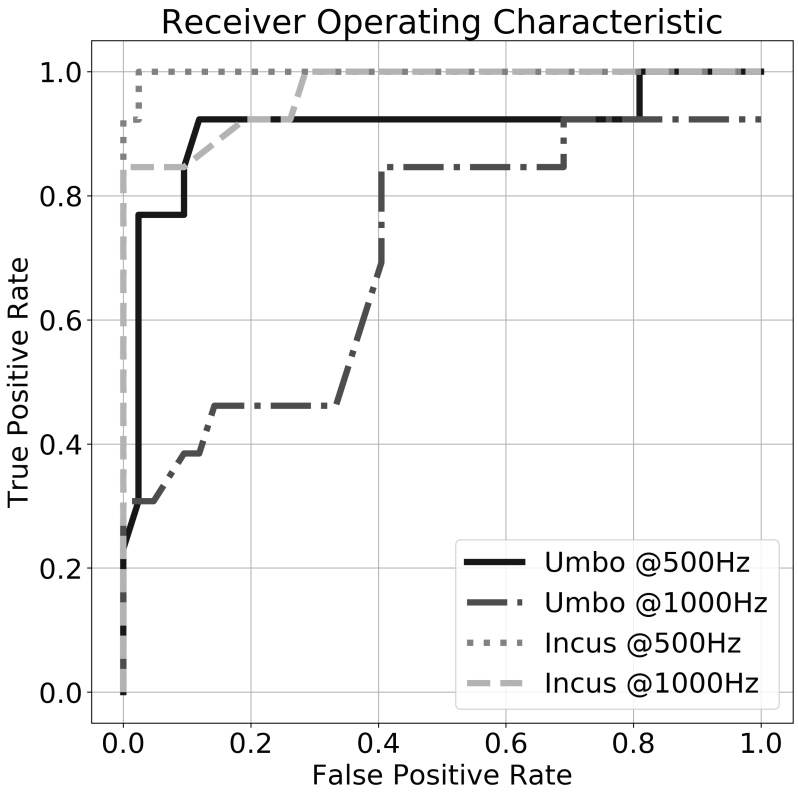

Figure 4.4: Receiver-operating-characteristic analysis for vibration measurements performed at the umbo and incus, at stimulus frequencies of $f_a = 500$ and $f_a = 1000Hz$, and $P_a = 100\text{dB}_{SPL}$

within the otosclerosis group, which could not reliably be distinguished from the patient motion noise floor with the current instrument. Improvements to either the sensitivity of the OCT-DV measurement or an increase in the amplitude of the sound stimulus could serve to further separate the normal group from the otosclerotic group and to partition otosclerotic ears according to the level of fixation. Within the patient group, there was one ear with very mild conductive loss that only narrowly met the ABG inclusion criteria for this study (patient 00137). This patient had an ABG of 10dB at 500Hz and 15dB at 1000Hz, and exhibited incus displacement above the noise floor at 15.3nm and 38.9nm, respectively. This suggests that the ossicular vibration is correlated to level of fixation and that a more sensitive system of this type could be used to assess the degree-of-stapes-fixation rather than just its presence.

A likely confounding factor in our measurements is the stapedius reflex. Because relatively loud stimuli of 100dB$_{SPL}$ are being used, the stapedius reflex is thought to be engaged in the normal ears but not in the otosclerotic ones [154]. This effect likely produces an increase in the variance of the normal group relative to the otosclerotic group due to variation in the amount of attenuation in incus vibration during activation of the reflex, and tends to make the two groups look more similar than would be observed if the stapedius reflex could somehow be circumvented.

4.7.2 Anomalous Functional Response in Otosclerotic Ear 00163

Within the otosclerotic group, a single patient was identified (patient 00163) with vibration levels indicative of pathology more complicated than simple otosclerotic stapes fixation. The patient's stapes fixation was confirmed at stapedotomy and the procedure was able to reduce the patient's ABG to 10dB at 500Hz, and 0dB at 1000Hz. Pre-operatively, however, this patient exhibited the highest umbo vibration levels at 1000Hz (430nm) of any subject in the study, including normal controls, and greater-than-normal vibration levels at 500Hz (195nm). The patient's umbo vibration levels are shown with black arrows in Figure 4.3A and 4.3B. The patient also had the highest incus vibration levels of any patient in the otosclerosis group at 1000Hz (38.9nm). Having noted this anomaly, we reviewed the patient's history in detail. We were intrigued to discover that the patient had recently experienced an episode of barotrauma during an airplane flight. This event was sufficiently severe to cause

intense bilateral ear pain and a confirmed TM rupture on the side contralateral to our study. It is possible that the patient suffered an additional injury to the ossicular chain from this event, causing the malleus to become mechanically uncoupled from the fixed stapes to some degree, however tympanometry tested normal. Interestingly, a previous study [26] examining diagnosis of conductive hearing loss using LDV at the umbo also reported a single patient with clinical otosclerosis and hypermobility at the umbo (patient P049L in Figure 1 of [26]) within a group of N=14 otosclerosis subjects. These two cases suggest that the incidence of stapes fixation in conjunction with umbo hypermobility may not be entirely rare. While the umbo measurement alone might have suggested ossicular discontinuity, the patient was still categorized as having fixation from the measurements at the incus. It is worth noting that this likely would not have been concluded from the incus measurement alone, since the hypermobility at the umbo and hypomobility at the incus is suggestive of a melleoincudal joint discontinuity. When compared to single-point LDV at the umbo, this points to likely advantages of OCT-DV's ability to provide vibrational information at multiple locations along the ossicular chain.

4.7.3 Comparison to Laser Doppler Vibrometry

Previous studies investigating the use of LDV as a diagnostic tool for differential diagnosis of various causes of conductive hearing loss reported sensitivity of 93% and specificity of 94% in the detection of stapes fixation, but relied on additional information provided by pure tone audiometry to overcome the insensitivity of umbo response to footplate fixation [26]. The results of the present study suggest that OCT-DV alone can achieve sensitivity and specificity higher than combined audiometry and LDV, owing to OCT-DV's ability to directly probe ossicular vibration distal to the umbo. Additionally, because OCT-DV measurements are spatially resolved, complex cases of conductive hearing loss that involve fixations or discontinuities at multiple locations may be better characterized by considering motion at different points in the ossicular chain. OCT-DV also offers important advantages in terms of ease and repeatability of alignment. In previous LDV studies [3], the measurement beam was aligned to the light reflex, *i.e.* the region of the TM that has its local surface-normal parallel to the optical axis of the imaging system. While this region is generally

close to the umbo, it does not always overlap with it, making umbo LDV prone to mis-measurement and overestimation of umbo velocity due to its confusion with nearby and more compliant TM. Because OCT-DV is aligned under cross-sectional image guidance, the umbo can be precisely located for measurement (see Figure 4.1E). Additionally, the measured brightness in OCT-DV is almost completely insensitive to the orientation of the structures being imaged.

While in this study we only examined vibratory response at two frequencies, nothing precludes measuring at more frequencies covering most of the range of human hearing as has previously been done with LDV. Upgrades to the system used in this chapter have enabled synchronous generation of stimulus tones with fine frequency resolution over the entire diagnostic frequency range of hearing, *i.e.* at frequencies that meet the condition of Equation 3.14. A more flexible processing algorithm is currently being developed to enable rapid OCT-DV calculations at all of these fine frequencies.

4.8 Conclusions

We have quantified the ability of OCT-DV to discriminate between the ears of normal controls and ears with a presumptive diagnosis of otosclerosis. Using a combination of cross-sectional anatomical imaging and non-contact OCT-DV measurements taken through the intact TM, the reduction in ossicular vibration response associated with stapes fixation was probed at the umbo and at the lenticular process of the incus during acoustic stimulation. Absolute displacement magnitude at a stimulus frequency of 500Hz at the incus was found to provide sensitivity of 1.00 and specificity of 0.98 in discriminating between the groups. This represented a significant improvement over measurements performed at the umbo alone. The results indicate that OCT-DV may offer improved diagnostic power over LDV which can only measure at the umbo, and over tympanometry which can only measure the mechanical compliance presented by the TM. One subject in our series showed that not all cases with surgically confirmed otosclerosis present with hypomobility at the umbo. In this case, OCT-DV was able to correctly detect stapes fixation through lower-than normal vibration at the lenticular process of the incus, which would still be indicative of otosclerosis despite the observed umbo hypermobility. Our results, taken together with those of previous

LDV vibrometry studies [3, 26, 54, 55, 59] suggest that OCT-DV may prove to be a powerful tool for discriminating between different causes of conductive hearing loss.

Chapter 5

Discussions

In this chapter I will present the results of individual case studies that qualitatively demonstrate the capability of middle ear OCT and OCT-DV to provide diagnostically useful information. This is preceded by a brief description of the continued development of the instrument, and considerations currently being addressed to promote adoption of technology of this type. Finally, brief descriptions of current limitations of the system are provided to reflect what we feel are the most important problems to solve in the future.

5.1 Continued Development: Mark II

In carrying out the work presented in chapters 2-4, improvements needed for the system to be more usable by clinicians in a typical high-throughput clinic environment were identified. A complete design iteration to the system has been carried out, mainly to address user and patient experience issues.

5.1.1 Contribution Statement

Contributions to the development of the Mark II system have been made by many individuals. Dr. Robert Adamson provided general direction to the team in all aspects of its development. Dr. David Morris, Dr. Manohar Bance, Dr. Nael Shoman, and Dr. Anne Oonk have collectively contributed user feedback and to patient recruitment. Christine Morrison coordinated patient imaging studies. Dan MacDougall and Christine Morrison carried out imaging studies with patients. Matthew Jahns, Carmen McKnight, and Dan MacDougall contributed to mechanical design. Dan MacDougall and Drew Hubley contributed electronic embedded system design. Joshua Farrell, Matthew Farrell, Drew Hubley, and Dan MacDougall contributed to software design. Dan MacDougall contributed the optical design. Many anonymous patients also volunteered their time to participate in imaging studies.

5.1.2 Mechanical Design

We have moved towards a hand-held, otoscopic form factor consisting of a desk-top console, a tethered hand-piece, and a wireless controller for controlling the user interface. The design is highly integrated with minitature speaker, microphone, illumination and imaging electronics packaged into the hand-piece. This is detailed in Figures 5.1 and 5.2, and was done in an effort to allow a single operator to interact with the patient and initiate measurements simultaneously, and because conventional otoscopes are inherently comfortable, safe, familiar, and easy to use. This has enabled very rapid imaging sessions.

5.1.3 Optical Design

The OCT engine in the current system very closely resembles that of Figure 3.1, however the hand-piece differs greatly from the mounted microscope head from Figure 3.3. The new design uses NIR illumination at $\lambda = 850$nm to provide full-time en-face otoscopic imaging of the TM, improving navigation of the ear canal. The OCT scanning optics have been miniaturized and use a 3.6mm diameter MEMS beam deflector in place of bulky galvanometer mirrors. A four-element pupil relay passes the scanned beam to a custom graded-index (GRIN) objective rod lens. The GRIN lens carries the beam to $\approx$ 3mm from the tip of a standard 4mm speculum, and places a pupil image at its distal end to achieve the $D_{FOV} \approx 10$mm at the middle ear and access the full VOI. The entrance pupils for both the OCT and the otoscopic imaging paths have been co-located so as to enable accurate co-registration between the imaging modes and prevent any relative parallax error between them. A custom wedged dichroic mirror is used to separate the OCT and otoscopic wavelengths, without introducing the image ghosting encountered in the TD-OCT system of Chapter 2. The OCT depth of best focus is nominally positioned 5mm deeper, axially, than that of the en-face imaging, so that the OCT may focus on the ossicles, while the otoscope remains focused on the TM. This is illustrated in the ray-tracing diagram of Figure 5.1A.

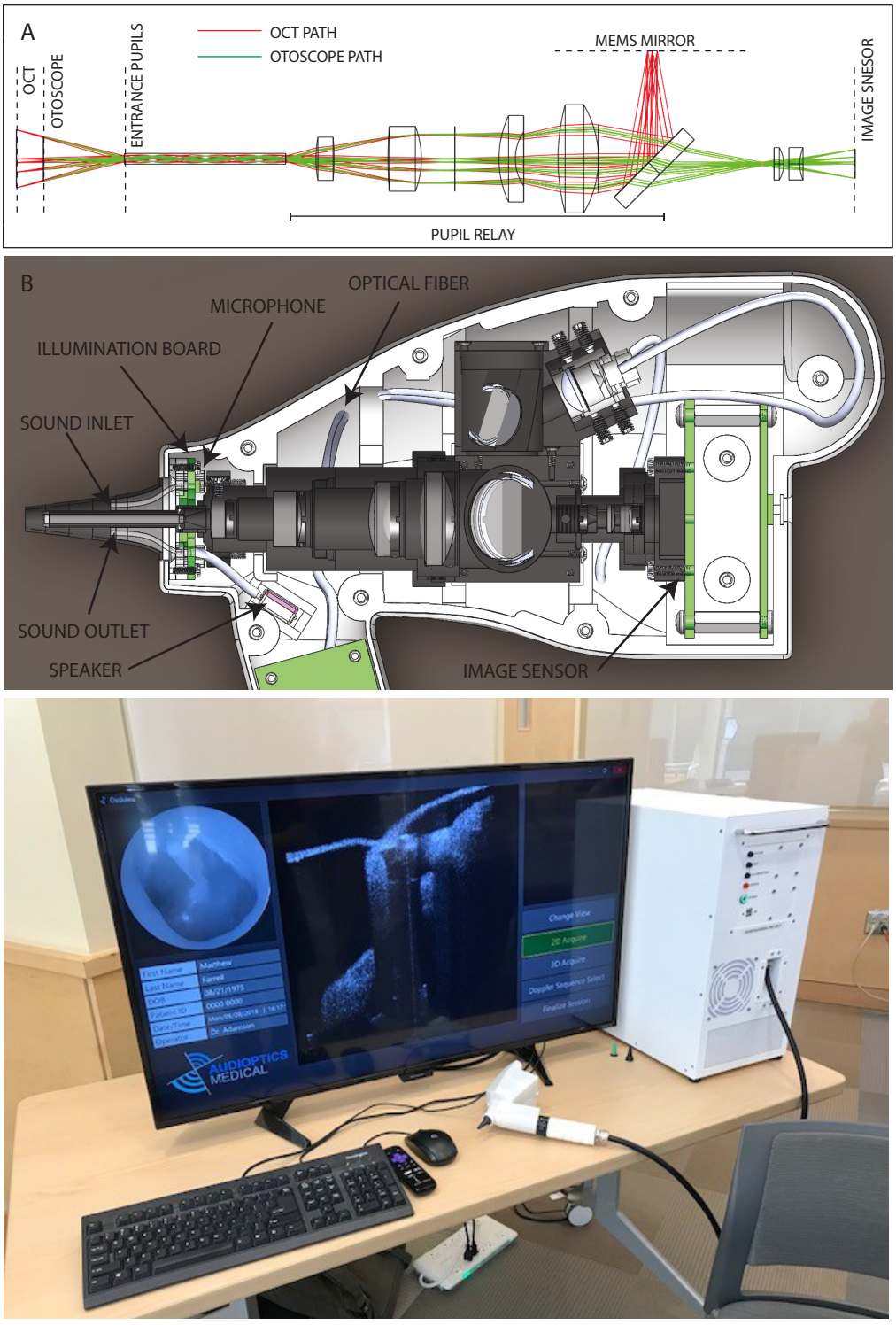

Figure 5.1: Design of the Mark II clinical imaging system. A, A ray-tracing diagram of the optical system internal to the hand-piece. B, A 3D section view of the internal components within the hand-piece. C, A photograph of the assembled console and hand-piece.

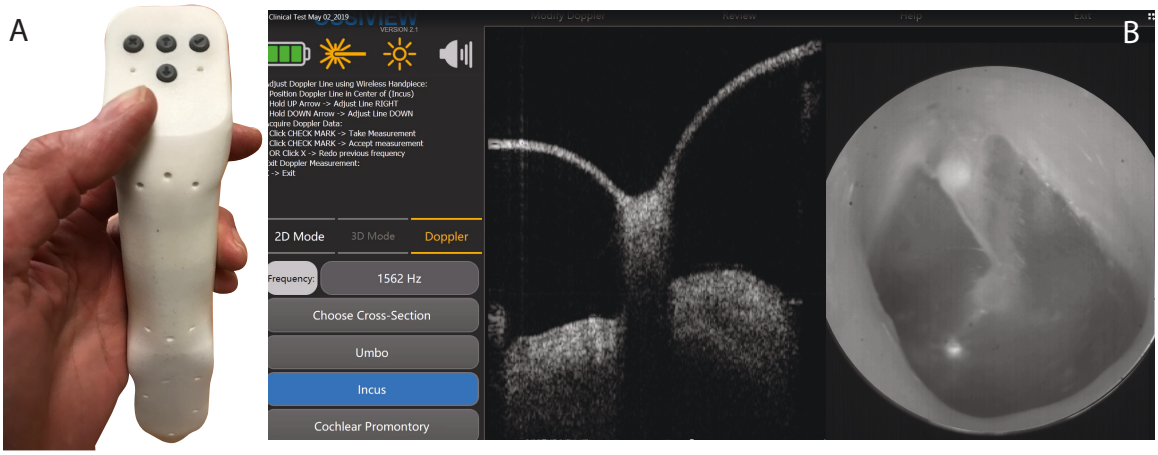

Figure 5.2: The Mark II user interface. A, The wireless controller that allows a single operator to select structures and initiate measurements while using the hand-piece. B, A screen capture from the graphical user interface showing a simultaneous 2D B-Mode image and an en-face otoscopic image.

5.2 Pathway to Adoption

Given the uniqueness of many of the clinical scenarios we have encountered in using the various iterations of the system, several of which will be described in Section 5.3, it has become increasingly apparent that the role transtympanic OCT will play in clinical otology will likely be quite case-dependent for the near future. It remains somewhat unclear which niche application areas within otology can *most* benefit from the image fidelity and access to functional information that OCT provides. Until there exists sufficient access to a common platform, with reliable, intuitive and convenient functionality, this will likely remain the case. The best route towards adoption depends greatly on demonstrating as wide a range of potential areas of impact as possible, and gauging excitement and interest from the community of otologists and ENTs. This requires that the technology to be made flexible, now, so that areas for specialization can be identified and incorporated in the future.

The challenges faced in the clinical translations of a new technology involves a very complex interplay of barriers to adoption, especially one as drastic a leap as OCT-DV in otology. Ghodeswar *et al.* concisely captured the conceptual factors that contribute to successful adoption in the hospital environment [5], from which Figure 5.3 was taken. Our work to refine transtympanic OCT and our access to interesting clinical cases has provided an opportunity to begin addressing some of these factors,

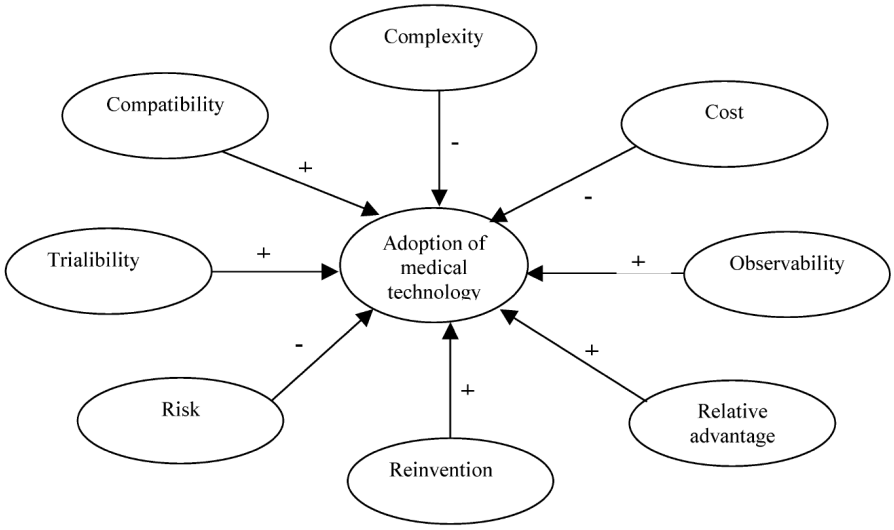

Figure 5.3: Contributing factors to the successful adoption of medical technology and innovation (taken from [5] under fair dealing).

a few of which are considered briefly below:

1. **Complexity** Relative to existing diagnostic tools commonly used in the otology clinic, OCT-DV is quite complex. While good engineering can hide the complexity of its inner workings, interpretation of its outputs remains challenging and still requires deductive reasoning, as will become apparent in Section 5.3.

2. **Risk** In terms of patient risk, transtympanic OCT's inherently safe and non-invasive mode of operation makes it a very attractive alternative to exploratory tympanotomy, although the degree to which exploration may be supplanted remains to be determined.

3. **Reinvention** As has become evident in the literature by the movement towards endoscopic, surgical microscopic and otoscopic delivery of OCT to the ear, the natural compatibility with otology's common optical imaging tools provides an avenue for creating a sense of familiarity with the technology.

In the following section, by presenting relevant examples of clinical use, we begin to address two additional factors critical to promoting transtympanic OCT and

OCT-DV's adoption: its potential "relative advantage" over standard practice, and its "observability", which refers to one's ability to see how an innovation works by watching someone else use it and then acknowledging that the technology is safe and beneficial.

5.3 Evidence of Clinical Utility: Transtympanic OCT Patient Cases

The images compiled in this chapter for discussion have not previously been published. They form the basis of a preliminary, evidence-based argument for the clinical utility of OCT and OCT-DV in otology and show how it could be used for improved decision making. The results presented below are largely the byproduct of having the system deployed in an active ENT clinic with an open invitation for clinicians to recruit patients with interesting cases for participation in our imaging study. With there being virtually no published literature on OCT or OCT-DV of real pathological cases aside from our own, and with direct access to patients with middle ear pathologies of all sorts, this section contains imaging results from real cases where the clinician felt transtympanic OCT could provide new insights into the pathology. Cases were chosen where there was uncertainty about the structural configuration of the middle ear, where obvious structural anomalies existed that could potentially be better visualized by OCT than by conventional means, or where there was expected abnormal or completely unknown activation and sound transmission through the middle ear. The data collected for each patient was tailored for each case to best capture the structural or functional features of interest.

Note that the images presented in this chapter were acquired and processed with the system at various stages of development, and there exist slight variations in system configuration that creates some variability in the appearance of the images. In all OCT-DV results presented in this section, measurements are limited in sensitivity to few nanometers by the practical OCT-DV noise floor encountered *in vivo*, and numeric values measured near this limit are not likely to be physiological. Despite this, logical conclusions can still be drawn. Each case represents a unique scenario with no prior, comparable results in the OCT literature. Since many of the provided interpretations of the results in this section cannot be confirmed by any other means, they merely represent promising avenues and potential areas of research for the future.

5.3.1 Generating Evidence Against Simple Stapes Fixation

The clinical narrative around patient 00190 is a prime example of the diffculties a clinician faces in pre-operative assessment of ossicular mobility. The patient presented with a right side ABG of 40dB, unremarkable CT imaging, normal tympanometry, a normal TM under otoscopy, and no family history of otosclerosis. The patient did, however, have a remarkable history of head trauma. Based on the presence of the significant ABG with no indicators of other pathologies, the attending physician pre-operatively diagnosed the patient with otosclerosis, while a clinical fellow disagreed due to the absence of Carthart's notch, and exploratory tympanotomy was pursued.

Figure 5.4 shows pre-operative OCT-DV findings very consistent with the mean activation levels presented in Table 4.1, leaning slightly towards hyper-mobility, and not supportive of a diagnosis of simple otosclerotic stapes fixation. Given the normal activation of the malleus and incus, partial dislocation of the incudostapedial joint is much more likely, which could potentially require a much simpler surgery. This is more consistent with the patient's history of head trauma, and is similar to the case of patient 00163 discussed in Chapter 4 where hypermobility was observed despite a confirmed finding of otosclosis at surgery, and further supports the notion that there are likely cases where additional ossicular pathology is present that goes undetected during stapedotomy.

On the morning of the exploratory surgery that would confirm the OCT-DV findings, patient 00190 suffered a heart attack in the OR and the exploratory tympanotomy was aborted.

5.3.2 Visualizing Perforations of the Tympanic Membrane

Visualization of TM perforations shows the middle ear in particularly good definition, owing to the absence of the TM's deleterious effects described in Chapter 2. Figure 5.5 shows a nearly complete right TM perforation collected in patient 01199220331, whose TM ruptured in a surfing accident. From a clinical utility perspective, anatomical OCT imaging through perforations like these may not have obvious advantages over conventional microscopy, given that microscopes and otoscopes can peer through the perforations as well. However, pure perforations with no accompanying pathologies of the ossicles can sometimes be repaired by a simple tympanoplasty in an office

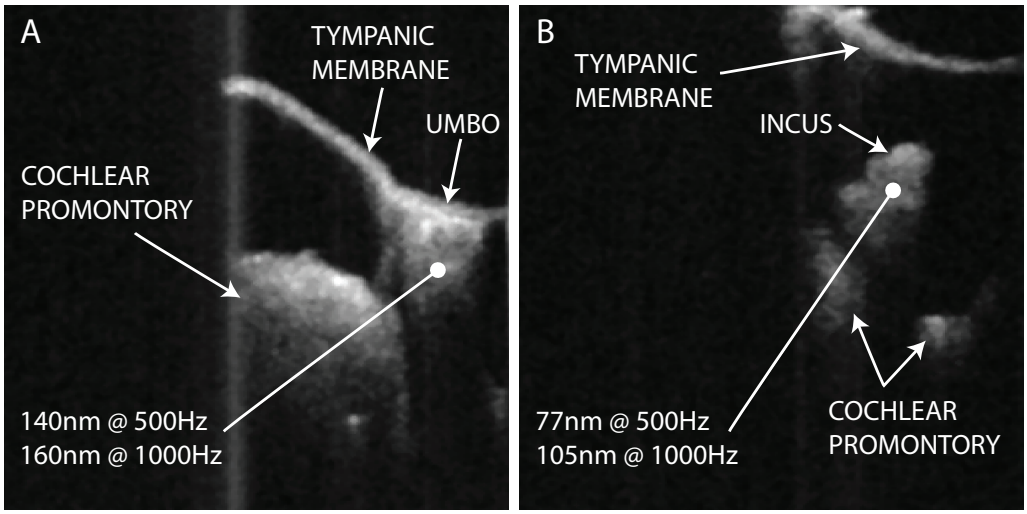

Figure 5.4: OCT images from patient 00190, *in vivo*, pre-operatively diagnosed with otosclerosis. A, OCT-DV results at the umbo. B, OCT-DV results at the incus. OCT-DV measurements were taken at $P_a = 100\text{dB}_{SPL}$.

setting under local anesthetic (*i.e.* as opposed to in the OR under general anesthetic). The clinical question where OCT may be of use revolves around determining if concomitant pathologies are contributing to the CHL and if escalation to a full exploratory tympanotomy is required. We performed the OCT-DV measurements of Figures 5.5C-D to assess whether any part of the ossicular chain was activated through air-conduction and found no substantial sound-induced displacement with our instrument.

Figure 5.6 shows another set of OCT-DV measurements taken in the perforated left ear of patient 00101, who had a history of chronic otitis media. In this ear there was some activation of the malleus (25nm in Figure 5.6B), but measurements at the round window were at the measurement noise floor (2nm in Figure 5.6C). Further work will be required to determine what displacement can be expected at the round window for a given level of ossicular activation, as the round window has been easily accessible in most of the posterior perforations we have imaged.

One complication in this application is that the perforation's presence alters the differential pressure generated across the TM, with significant dependence on the geometries of the ear, and the perforation itself [18]. This is because the pressure wave in the ear canal effectively leaks around to the TM's medial side. As is readily obvious in the both Figures 5.5, if the TM is sufficiently perforated to prevent any measureable

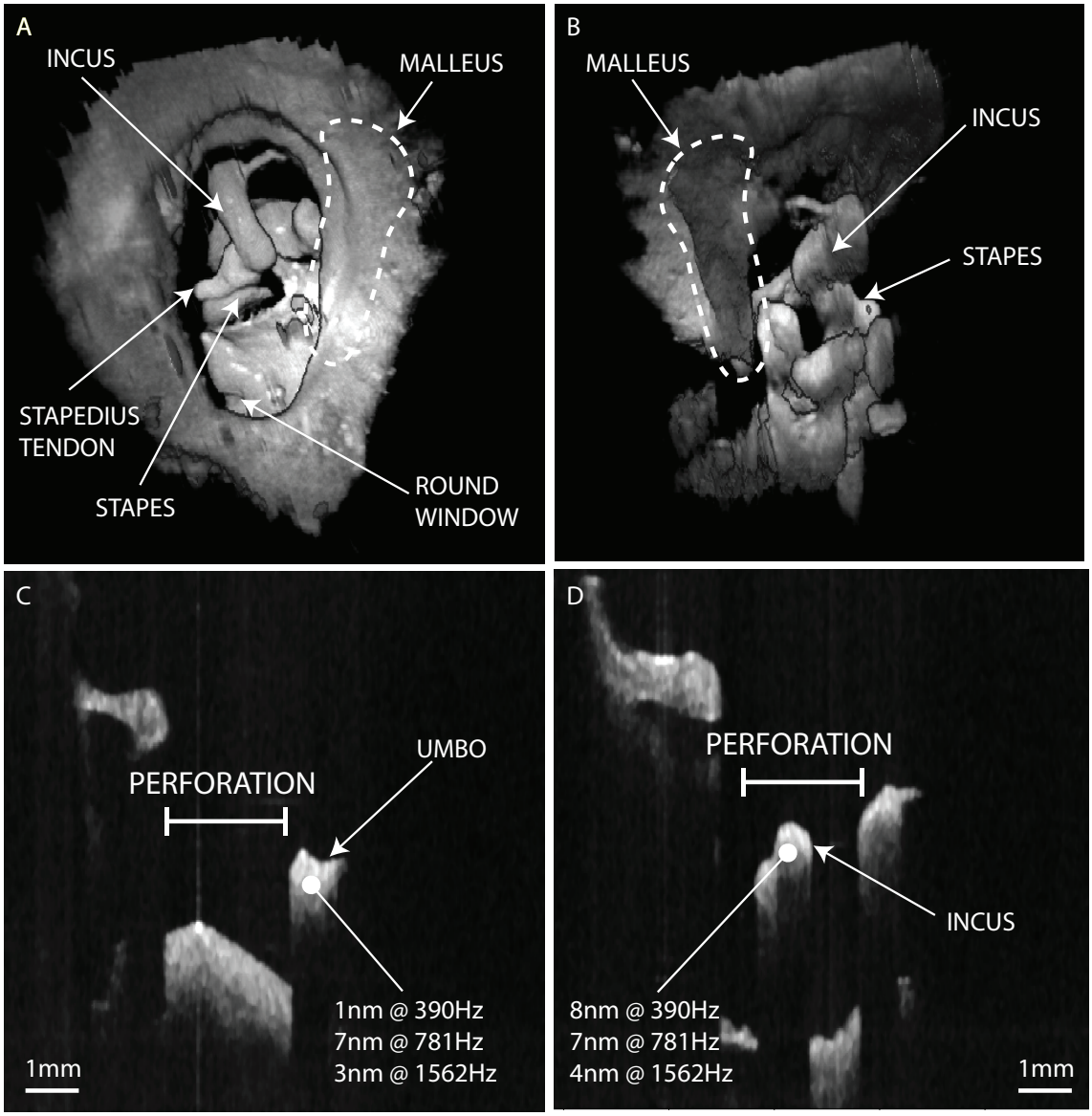

Figure 5.5: OCT images of a nearly complete TM perforation in patient 01199220331, *in vivo*. A, A 3D rendering of the middle ear as seen from the ear canal, and B, as seen from the medial side of the middle ear. C, A 2D B-Mode image and OCT-DV measurements taken at the umbo, and D, at the incus. OCT-DV measurements were taken at $P_a = 100\text{dB}_{SPL}$.

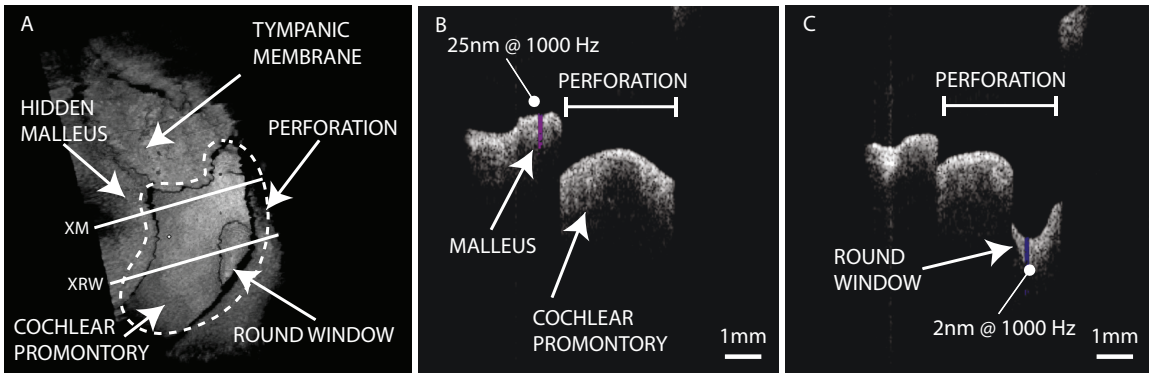

Figure 5.6: OCT images of a partial TM perforation in Patient 00101, *in vivo*. A shows a 3D volumetric rendering of the TM perforation. **XM** indicates the location of the cross section shown in B, a 2D B-mode image with OCT-DV measurement on the malleus. **XRW** indicates the location of the cross-section shown in C, a 2D B-mode image with OCT-DV measurements on the round window. OCT-DV measurements were taken at $P_a = 100\text{dB}_{SPL}$.

air-driven displacement of the malleus, it becomes difficult to draw conclusions about the incus and stapes since there is no driving force reaching them. A means of normalizing the activation of the ossicles in the presence of this kind of inter-ear variability would be needed for OCT-DV to be diagnostically useful.

5.3.3 Assessing Retractions and Sound Coupling to the Ossicles

Patients often present with configurations of the TM and ossicles that continue to transmit sound effectively despite complete departure from normal anatomy. Figure 5.7 shows the left ear of patient 01199220131, where a retraction pocket is evident from the direct contact between the TM and the incus. The patient suffered from virtually no CHL, and interestingly, Figures 5.7B-C suggest that activation at the incus appears to be overall greater than at the umbo, in opposition to what is observed in the normal hearing cohort of Table 4.1, and inconsistent with the impedance transformation that normally occurs through the ossicular chain. This suggests that the retracted TM is directly driving the incus, and not via transmission through the malleus. While OCT-DV offers insight into the mechanics of the pathology and would support an argument that the abnormality should be left undisturbed, it is at least in this case not obviously impactful since the patient nonetheless required tympanoplasty to stabilize the retraction.

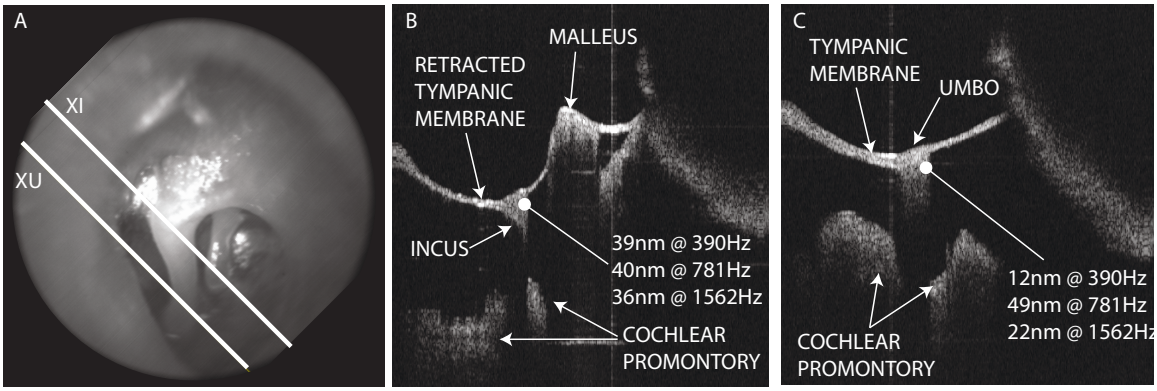

Figure 5.7: Images of the left ear in patient 01199220131 with an adhesive retraction pocket. A, an en-face IR otoscopic image of the ossicles and TM. **XI** indicates the location of the 2D B-mode image of the retraction pocket adhered to the incus shown B. B also shows OCT-DV measurements of incus displacement. **XU** indicates the location of the 2D B-mode image of the malleus in C. C also shows OCT-DV measurements of umbo displacement. OCT-DV measurements were taken at $P_a = 100\text{dB}_{SPL}$.

5.3.4 Revealing Unknown Surgical Histories

Not all patients arrive to the otology clinic with complete documentation of their medical history. Figure 5.8 shows images acquired in patient 00198 who presented with moderate CHL in their right ear with $\approx$ 30dB ABG across all frequencies. The patient had a history of otitis media, and tubes placed as a child $>$ 20 years prior to examination. Additionally, the patient denied having any symptoms other than difficulty hearing, and no history of previous middle ear surgery. A CT scan reported the middle ear space to be unremarkable. Under microscopy, the TM was thickened posteriorly, with tympanosclerosis as a possible cause for the CHL. There were no visual indicators compelling enough to suspect an inaccurate surgical history. Pre-operatively, the prevailing theory was of otosclerotic fixation, despite no family history, and exploratory tympanotomy was required.

The OCT images clearly showed what the surgeon eventually confirmed to be a section of silastic sheet (*i.e.* silicone rubber) inside the patient's middle ear cavity. Silastic is sometimes placed in the ear during tympanoplasty or other surgeries to prevent adhesion and soft tissue infiltration [155]. This is a clear indication that the patient's history differed from their memory, and that a surgical approach would not in fact be a primary surgery, and carried a different risk profile. While we were under

an ethical obligation not to alter the patient's course of treatment with our findings, having this knowledge could have ruled out tympanosclerosis, and confidently attributed the TM's thickening to a previous tympanoplasty. This posterior thickening precluded OCT-DV measurements at the incus, but measurements taken at the umbo revealed displacements of $\approx$ 32nm and $\approx$ 68nm at 500Hz and 1000Hz, respectively, suggesting substantial ossicular activation, although below the discriminating thresholds for otosclerosis found in Table 4.2. At exploration, the patient was in fact found to have middle ear adhesions and an attenuated incudostapedial joint (*i.e* a partial ossicular dicontinuity). The discrepancy could reasonably be attributed to the fact that the otosclerosis cohort in Chapter 4 had normal TMs and no history of surgery. One would also reasonably expect CHL arising from tympanosclerosis of the TM to be evident in OCT-DV measurements at the umbo since CHL should be associated with a reduction in activation of all of the ossicular chain. Relative to normal, the respective -13dB and -7dB umbo displacements cannot account for the 30dB ABG, which is consistent with pathology more complicated than tympanosclerosis alone.

5.3.5 Objective Evidence of Partial Ossicular Discontinuity in "Sniffer-Poppers"

There is a significant population of CHL patients who are able to temporarily improve their hearing acuity by intentionally manipulating the static pressure in their middle ear cavity. This can be done with sharp sudden sniffing or popping (*i.e.* a Valsalva maneuver). The effect can be quite dramatic but typically subsides as the middle ear equalizes to atmospheric pressure. Figure 5.9 shows OCT images collected in patient 001199220571, who suffered barotrauma during a rapid extraction of their finger from the ear canal while under water, inadvertently creating a suction effect in the canal. The patient only presented with a mild CHL, but complained of "buzzing" sounds during sound stimulus. Tympanometry was of type A_D, (*i.e.* hypermobile/hypercompliant), and examination with otoscopy showed an atelectatic TM section that was plausibly responsible for all of the symptoms.

If the improvement in hearing acuity after valsalva were solely due to inflation of the atelectatic segment, one would expect that to be apparent with an increase in

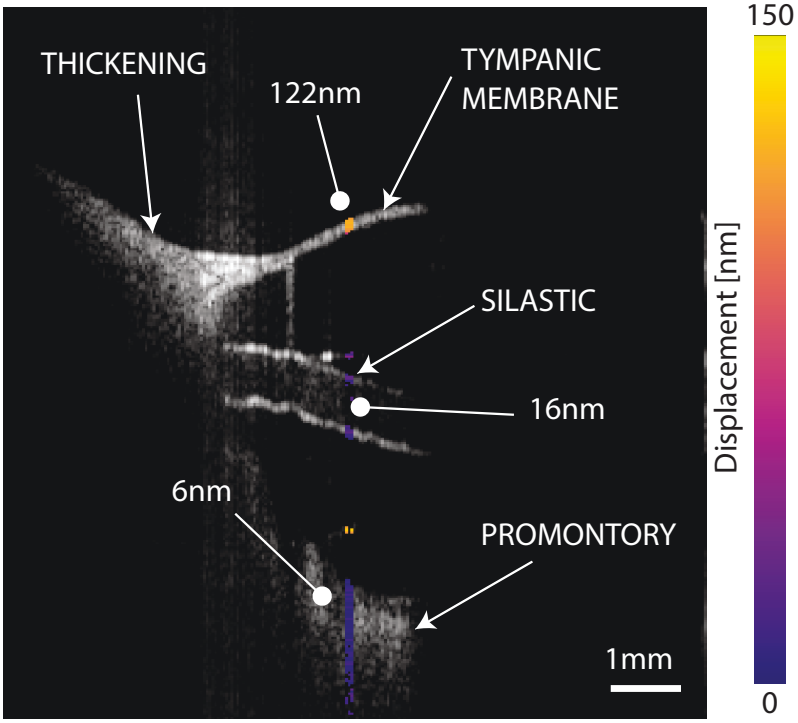

Figure 5.8: Anatomical and OCT-DV image acquired from a patient who had reported *no history* of middle ear surgery to the clinic. The image clearly shows the presence of a silastic sheet medial to the eardrum, likely placed there either by a magical being of some kind, or during a previous middle ear surgery. The sound induced peak-to-peak displacements of the visible structures were probed with OCT-DV, shown by the color mapped overlay and annotations. Interestingly, there is some activation of the sheet, indicating that it is mechanically coupled to the ossicles and may be contributing to the CHL. OCT-DV measurements were taken at $f_a = 500\text{Hz}$ and $P_a = 100\text{dB}_{SPL}$.

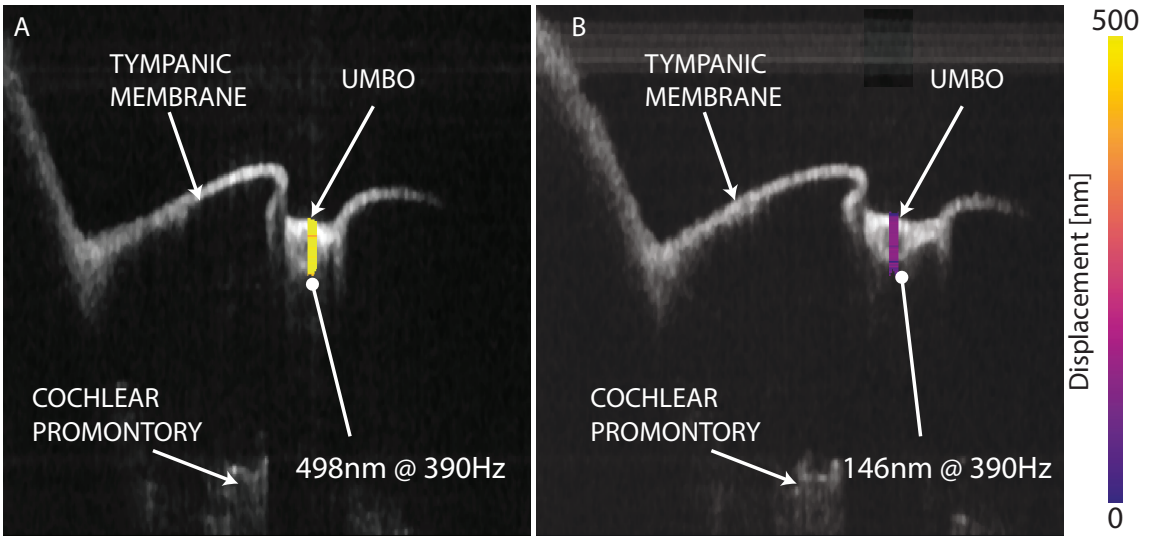

Figure 5.9: Transtympanic OCT images taken in a patient's right ear whose CHL improves following a valsalva maneuver, but returns after pressure equalization. A, Showing umbo displacement measured immediately before and, B, immediately after pressurizing the middle ear.

the activation of the malleus in the pressurized state. However, OCT-DV measurements taken at the umbo revealed contrary evidence since malleus activation, in fact, decreased during pressurization, as shown in Figure 5.9. This is highly suggestive of a partial ossicular discontinuity. In simple terms the OCT-DV measurements suggest that in addition to a "floppy" TM, there is also a "loose" joint in the ossicular chain that rattles when stimulated by sound. Patient 001199220571 did not present with sufficient CHL to warrant surgery, and so the partial discontinuity could not be confirmed. A reliable measurement at the incus couldn't be made in this patient to further probe transmission through the ossicles.

5.3.6 Visualizing Traumatic Ear Injury

Traumatic ear injury resulting in CHL presents a clinical challenge in that medical history is often irrelevant, and because the nature of the injury may or may not have gross anatomical indicators visible from outside the ear canal. Figure 5.10 shows OCT images obtained in patient 00200 who experienced an accidental breach of the ear canal during temporomandibular joint arthroscopy. The result was a perforation of the TM through direct contact with the penetrating endoscope and with evident

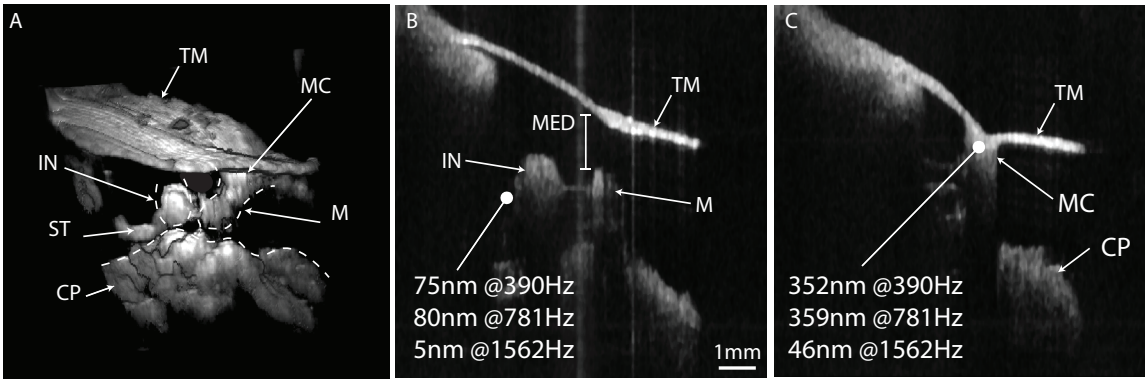

Figure 5.10: OCT images acquired in patient 00200, who suffered traumatic perforation of the TM and disruption of the ossicles following complications during temporomandibular arthroscopy. A, A render of the 3D volume with the abnormal configuration of the ossicles highlighted with dotted lines. B, A 2D B-mode image through the incus and the malleus at the umbo, showing that the malleus has medialized ≈ 1.5mm away from the TM. B shows OCT-DV measurements of incus activation. C shows a 2D B-mode image with OCT-DV measurements of activation at the umbo where it remains coupled to the TM, half way up the manubrium. **TM** tympanic membrane, **IN** incus, **ST** stapedius tendon, **CP** cochlear promontory, **M** malleus, **MC** inferior mallear contact point with the TM, **MED** medialization.

disruption of the ossicles. The patient's hearing was, presumably, normal prior to the injury, but presented with a moderate $15-35$dB ABG. The images clearly show the malleus partially medialized, with separation from the TM occurring about half way down the length of the manubrium. OCT-DV revealed that despite the trauma, there remains very high activation of the malleus at its contact point to the TM across a range of frequencies. However, the results also suggests a roll-off in transmission to the incus at 1562Hz, which is consistent with audiometric findings that the patient's ABG is 20dB worse at 1000Hz than at 500Hz. Overall, these results are strongly suggestive of concomitant disarticulation of the malleoincudal joint (based on the abnormally high activation of the malleus) and ossicular discontinuity medial to the incus (based on the presence of the relatively large ABG despite activation of the incus being very near the normal mean in Table 4.1 at low frequencies), *i.e.* either a fracture of the stapes, or a dis-articulation of the incudostapedial joint. Patient 00200 decided not to undergo an additional surgery due to risk aversion so the deductive reasoning made from the OCT-DV measurements could not be confirmed.

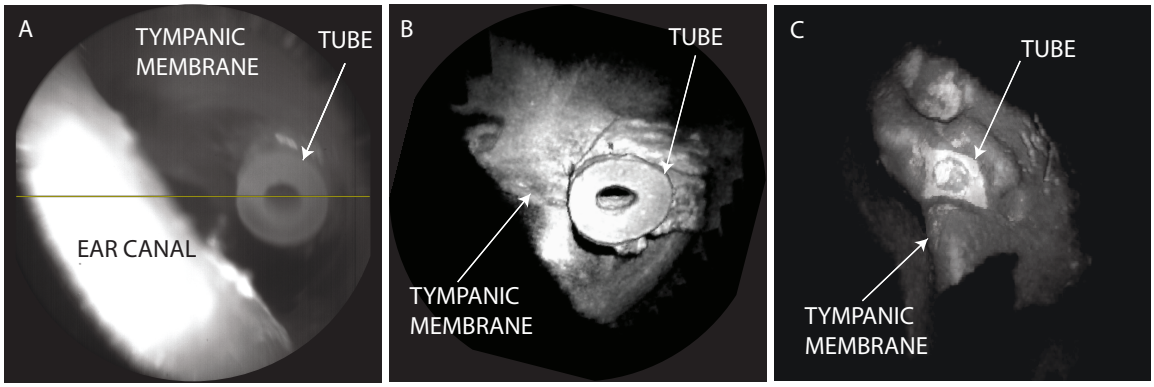

Figure 5.11: Anatomical images of tympanostomy tubes, *in vivo*. A, IR otoscopy, and B, a 3D rendering of OCT of the TM and tube in patient 01199220531. C shows the surface of a medialized tube hidden behind the TM in patient 01199220611, which has been emphasized by adding transparency to the TM and increasing brightness with axial depth.

5.3.7 Detecting Foreign Objects Behind the TM

Tympanostomy tubes are placed to drain fluid from ears with recurrent or chronic otitis media, with the expectation that they will naturally migrate laterally and into the ear canal, or will be deliberately removed by a surgeon. Figures 5.11A-B show the intended placement of tubes in the left ear of patient 01199220531. The ability to view the tube in 3D and perform OCT-DV is intriguing, although not particularly useful in this case. However, Figure 5.11C shows the left ear of patient 01199220611 where a tube was placed ≈ 8 years prior to imaging, and has migrated medially. The TM has healed over to enclose the tube in the middle ear cavity. In this particular case the clinicians already very strongly suspected that the tube remained, but the OCT imaging provides added confidence since its surface profile is directly visualized.

5.4 Current Limitations of the System

5.4.1 Accessible Volume of Interest

Even since adopting a true otoscopic form-factor, we have found that there remains a significant fraction of subjects whose middle ear cannot be satisfactorily accessed. One limiting factor is the curvature of the ear canal, which can completely shadow entire regions of the TM from view, *e.g.* in Figure 5.11 where only about 50% of

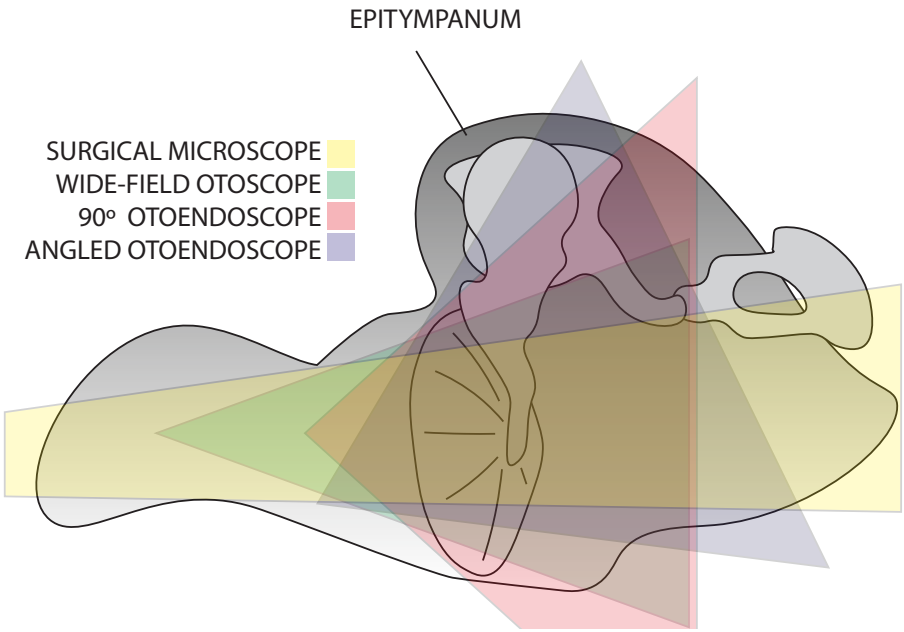

Figure 5.12: Accessible volume of interest for different form factors the device could take, including surgical microscopes, wide-field otoscopes like the devices demonstrated in this work, and forward-facing or angled otoendoscopes, which could provide the best visualization of the epitympanum.

the membrane is visible. Another limitation is the superior placement of the ossicles in the middle ear. The head of the malleus, the body of the incus and the malleoincudal joint are contained in the epitympanum, or the "attic", making them invisible to our current instrument. Accessing this region would be beneficial for a greater ability to interrogate the ossicular chain, but also because it is a common site for cholesteatoma and other pathologies. An angled endoscopic probe would best address that limitation, as is illustrated in Figure 5.12 that shows the potentially accessible FOV achievable if the system were to be implemented in different form factors. More problematic, though, is that the long process of the incus and the incudostapedial joint are sometimes completely obscured by the scutum. The images of Figure 4.1 are of a particularly accessible middle ear since a large section of the incus is visualized. Poor access to the incus increases the difficulty in aligning the optics for the types of measurements that were performed in Chapter 3-4, and in the cases where a measurement cannot be obtained at any of the deeper ossicles, OCT's advantages over LDV are effectively reduced.

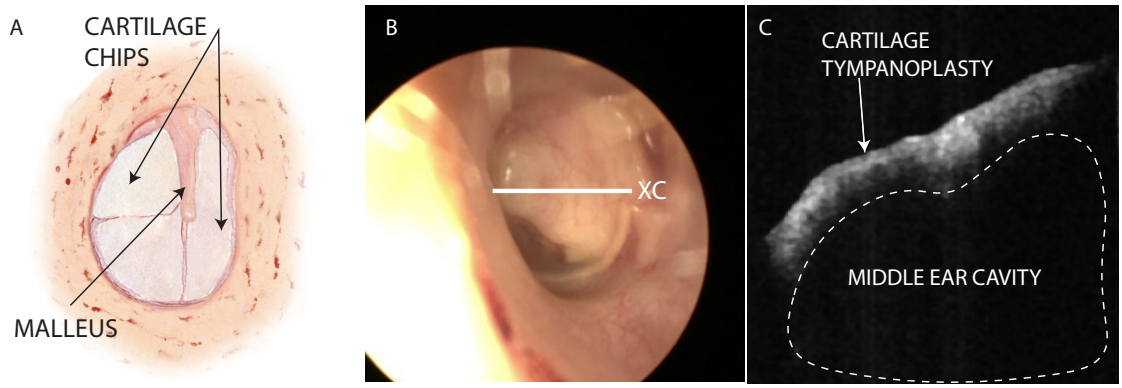

Figure 5.13: The deleterious effects of tympanoplasty on transtympanic middle ear image. A, A diagram of "palisade" tympanoplasty (taken from [4] with permission, illustration by Anne Johnson). B, A surgical microscope view of a healed cartilage tympanoplasty. **XC** indicates the location of the 2D B-Mode image shown in C of the tympanoplasty with no ability to resolve the ossicles.

5.4.2 Imaging Through Tympanoplasties

Tympanoplasty leaves the reconstructed TM thicker and more opaque than a normal TM, and ultimately precludes transtympanic OCT imaging of the middle ear. Figure 5.13A shows one approach to total tympanoplasty called "palisade", in which the TM is overlayed with harvested cartilage chips [4]. Figure 5.13B shows how this would appear under microscopy after healing. The anatomical OCT imaging results shown in Figure 5.13C shows no features of the middle ear space, and is representative of all imaging we have performed in post-tympanoplasty patients. This presents a clear limitation to utility in a significant patient population that could benefit from post-operative visualization of the middle ear space.

5.4.3 Practical Noise-Floor Limits in *In Vivo* OCT-DV

As was previously described in Chapter 3-4, OCT-DV displacement sensitivity is somewhat degraded in live subjects. Figure 5.14 shows measurements taken in a steady subject with the sound stimulus on and off, and compared to measurements taken in a stationary phantom. All measurements were taken over 2s. In Figure 5.14A it is apparent that there is more variation in the pixels measured at the incus with the stimulus applied than without. In Figure 5.14B, it's clear that there is a tighter grouping in the phantom measurements than in the case of no stimulus at

the incus, although this may be due to the difference in brightness of the reflectors. In Figure 5.14C, it is interesting to note that the grouping of points for the incus measured with stimulus appears to be bi-modal. The sub-grouping at the bottom right of the main grouping is, interestingly, associated with the *first* measurement set collected, and could be related to stapedius reflex relaxation following repeated loud stimuli. The important feature of Figure 5.14 is that despite being able to repeatably achieve low noise floors of a few nanometers in $\approx$ 2s both in stationary objects and *in vivo*, there are other factors that contribute to how much variation exist in the measurement. Possible contributing factors are physiological variations over time, poor repeatability in the acoustic pressure developed at the TM, or some variable degree of cross-talk between vibrating structures within the measurement line (*i.e.* the presence of the TM's large displacement amplitude coupled with the finite dynamic range of the system, leading to cross-talk between their extracted OCT-DV amplitudes). While the VT-DBRL has been shown to approach shot-noise limited phase sensitivity [106], a complete understanding of all of the contributing sources of variability and channel separation is needed. Fortunately, even in the presence of this system's current limitation, activation of the structures of the middle ear can already be quantified at physiologically relevant sound levels.

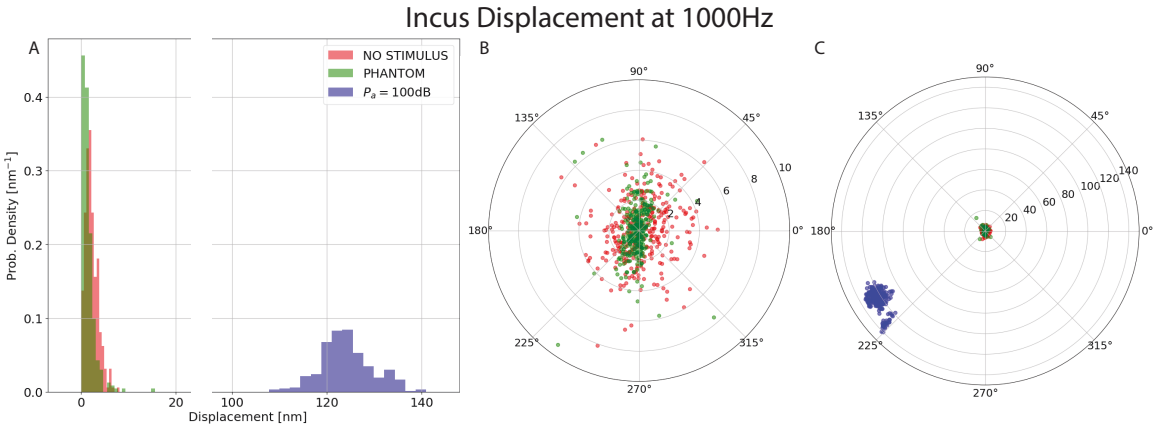

Figure 5.14: Distribution of OCT-DV measurements at $f_a = 1000$Hz across 300 pixels taken in a single subject at the incus, *in vivo*. A, density distributions of displacement magnitude. B and C, polar plots showing the complex pixel values from the OCT-DV data in A at different scales. For each condition, 10 measurements were performed a few seconds apart, with 30 pixels extracted from each. Red shows measurements with no sound stimulus playing, blue shows measurements with stimulus at $P_a = 100\text{dB}_{SPL}$, and green shows measurement taken in a stationary reflector sitting on a table. Measurements were 2s in duration ($M \times N = 204,800$ in Equation 3.9).

Chapter 6

Conclusion

Given the otologist's ability to restore hearing in cases of CHL and the uncertainties about the underlying causes when proceeding to surgery, transtympanic OCT's ability to penetrate the TM and resolve both the structure and function of the middle ear presents a tremendous opportunity to impact clinical decision making. The prevalence of exploratory tympanotomy is indicative of a need for better diagnostics in the middle ear that inform the clinician of exactly what will be encountered in the OR. The varied combinations of symptoms and diagnostic findings provided by current tools like CT and tympanometry may be consistent with the overall clinical narrative, but often don't contain the expected supporting evidence or must be disregarded. Consequently, diagnosis relies heavily on the clinician's experience to formulate an overall assessment. Recent years have seen a rapid increase in the amount of ear-related OCT literature [156], reflective of its potential as a diagnostic tool and accumulating clinical interest. The exciting technical advances that are enabling OCT-DV studies in hearing physiology can immediately benefit from the deep LDV literature that provides strong evidence for the sensitivity of optical vibrometry to the deviations from normal dynamics in middle ear pathology. However, moving from benchtop studies in animals and cadavers to live subjects in a clinical setting presents significant challenges.

In working towards a complete understanding of how to achieve image quality satisfactory for a clinically deployable transtympanic OCT system, experimental work titled, "Optical coherence tomography system requirements for clinical diagnostic middle ear imaging" was published in the Journal of Biomedical Optics, on which Chapter 2 was based. This work showed how, if one pushes the VOI to 1cm^3, and the speed to real-time rates of $f_r = 10\text{FPS}$, it remains possible to adequately resolve the ossicles transtympanically. To do so, relatively high dynamic range ($\text{DNR} > 60.5\text{dB}$) and sensitivity ($S_i > 97\text{dB}$) are needed to combat the necessarily low $NA < 0.022$

and optical transmittance in the TM ($T_{TM} \approx -13.5$dB). While the system used for the work was of a TD-OCT topology and was too slow, insensitive, and inconvenient for *in vivo* imaging, it provided cadaver evidence to support two of the many potential areas of clinical utility that would subsequently be explored: anatomical images of a simulated erosion of the long process of the incus, and of a migrated PORP.

Chapter 2 confirmed that the desired real-time system was feasible, and thanks to the advent of the VT-DBRL, that it would take the form of a SS-OCT system built around the breakthrough light source that could enable OCT-DV measurements of middle ear dynamics. While others had taken advantage of the same source for functional hearing imaging, our desired system needed to be appropriate for use in live patients in a clinical setting, and accomplishing this was the focus of the work. The system we designed was detailed in "Long-range, Wide-Field Swept-Source Optical Coherence Tomography with GPU Accelerated Digital Lock-in Doppler vibrography for real-time, *In Vivo* Middle Ear Diagnostics", published in Biomedical Optics Express. The demonstrated system produced unprecedented images with access to the full middle ear's 1cm^3 VOI. While basic OCT-DV functionality was validated via volumetric mapping of the TM and ossicular dynamic response to sound in a cadaver specimen, more exciting evidence for two additional promising areas of potential clinical utility were presented; post-operative imaging of stapes piston placement on the long process of the incus, *in vivo*, showing distinct and easily discernible regions of bone and prosthesis; and the first reported OCT-DV measurements in live human, more specifically, taken transtympanically at the incus and showing good agreement with the expected physiological behavior. In the broader context, the *in vivo* measurements represented the breaking of the limits of what is possible with LDV by probing ossicular activity beyond the malleus, non-invasively. Although cumbersome and not yet comfortable for the patients, the system represented the first setup suitable for performing OCT-DV experiments on a patient population. Additionally, the system architecture incorporated scalable GPU acceleration of the OCT-DV processing, and took advantage of careful system synchrony and optimization of frequency analysis for real-time processing and display. The system was shown to achieve sufficient throughput for continuous 100% duty processing at full-speed sweeping with the SLE-101 VT-DBRL on a consumer-grade NVidia GTX660 GPU at $f_l = 100$kLPS,

and addressed the need for immediacy of results in practical patient imaging studies.

OCT-DV's ever-growing use in the literature for probing fundamental hearing physiology has tremendous value in its own right, but clinical adoption will rely on objective evidence of its ability to positively impact clinical decision making or outcomes. The accessibility of our system to patients enabled the first comparison between OCT-DV measurements in normal and pathological ears. This was the work of Chapter 4, which was published in Otology and Neurotology under the title "Optical Coherence Tomography Doppler Vibrometry Measurement of Stapes Vibration in Patients with Stapes Fixation and Normal Controls", where cohorts of individuals with normal hearing and individuals having strong clinical evidence for otosclerotic stapes fixation were compared, and conclusions were drawn from the sampling of those populations.

When measured with our instrument and stimulated with pressure levels of $P_a = 100\text{dB}_{SPL}$ in the ear canal, the normal cohort exhibited mean peak-to-peak displacements levels; at the umbo of 150nm at $f_a = 500$Hz and 1000Hz; and at the incus of 79nm at $f_a = 500$Hz and 70nm at $f_a = 1000$Hz. The otosclerosis cohort exhibited mean levels; at the umbo of 55nm at $f_a = 500$Hz and 107nm at $f_a = 1000$Hz; and at the incus of 9.7nm at $f_a = 500$Hz and 17.9nm at $f_a = 1000$Hz, with the caveat that the sample distributions in this case are skewed by the instrument's practical displacement sensitivity in *in vivo* measurements. The data suggested that low-frequency functional probing of the middle ear provides the best discrimination between groups, and that OCT-DV's ability to measure at the incus is more sensitive to this fixation than at the umbo (*i.e.* the anatomy accessible to LDV). Absolute displacement at a stimulus frequency of 500Hz at the incus was found to provide the best discrimination between the two groups with sensitivity and specificity of 1.00 and 0.98. The normal data also provided a bench mark for comparison of future measurements with the instrument in individuals with unique pathologies and unknown middle ear activation.

Despite the exciting results, there remain many practical challenges to address to improve the characterization of pathology and capture more aspects of middle ear structure and dynamics, *e.g.* to improve usability and clinic-compatibility, dealing with ergonomics and workflow; to improving the achievable displacement sensitivity

in *in vivo* OCT-DV measurements so that higher fidelity is possible, and so that vibratory response can be quantified even in severely fixated middle ears with large ABG; to explore means of accessing an even greater VOI, specifically allowing access to the epitympanic region to reliably visualize the incus in a greater fraction of the population; and to reduce imaging artifacts arising from sources like imperfect PSFs and multiple scattering that render the images more difficult to interpret.

In general, the questions answered by the works of Chapters 2-4 progressed from "Will this be possible?", to "How does one make this practical?", and now remains "How much impact can this have on clinical practice?" Our continued efforts to refine the system are motivated by this question, and in my opinion, this is the most interesting and exciting avenue for future research in OCT imaging of the ear. Ultimately, our ability to convincingly provide benefits to the clinician will rely on developing a body rigorous statistical analyses like that of Chapter 4 in carefully chosen pathologies. However, from a motivation stand-point, the conjectured analyses and discussion of imaging results from the selected set of unique patient cases have proven to be the most compelling aspects of the overall work, in that they set up very logical forward pathways to generate new evidence of utility.

Bibliography

[1] Brad A. Stach, editor. *Clinical Audiology: An Introduction*. Delmar Cengage Learning, Clifton Park, NY, 2nd ed edition, 2010. OCLC: ocn173086974.

[2] Na Zhang, Yi Li, Xiaobo Ma, Danni Wang, Shuling Li, Fei Yan, and Shouqin Zhao. Isolated Congenital Middle Ear Malformations: Comparison of Preoperative High-Resolution CT and Surgical Findings. *The Annals of Otology, Rhinology, and Laryngology*, page 3489419883659, October 2019.

[3] John J. Rosowski, Hideko H. Nakajima, and Saumil N. Merchant. Clinical utility of laser-Doppler vibrometer measurements in live normal and pathologic human ears. *Ear and Hearing*, 29(1):3–19, January 2008.

[4] Michel C. H. Gersdorff and Jean-Marc Gérard. *Atlas of Middle Ear Surgery*. Thieme, Stuttgart New York, 2011. OCLC: 693888578.

[5] B.M. Ghodeswar and J. Vaidyanathan. Adoption of medical technology by hospitals: A review of innovation attributes and a conceptual model of the resulting service. *World Review of Science, Technology and Sustainable Development*, 3(4):362, 2006.

[6] J. A. Izatt and M. A. Choma. Theory of Optical Coherence Tomography. In Elias Greenbaum, Wolfgang Drexler, and James G. Fujimoto, editors, *Optical Coherence Tomography*, pages 47–72. Springer Berlin Heidelberg, Berlin, Heidelberg, 2008.

[7] C. B. Ruah, P. A. Schachern, D. Zelterman, M. M. Paparella, and T. H. Yoon. Age-related morphologic changes in the human tympanic membrane. A light and electron microscopic study. *Archives of Otolaryngology–Head & Neck Surgery*, 117(6):627–634, June 1991.

[8] Karen J. Cruickshanks, Ted S. Tweed, Terry L. Wiley, Barbara E. K. Klein, Ronald Klein, Rick Chappell, David M. Nondahl, and Dayna S. Dalton. The 5-year incidence and progression of hearing loss: The epidemiology of hearing loss study. *Archives of Otolaryngology–Head & Neck Surgery*, 129(10):1041–1046, October 2003.

[9] K.M.A. Sarmento, C.A.C.P. de Oliveira, A.L.L. Sampaio, and A.F. Sales. Erosion of the long process of the incus with incomplete ossicular discontinuity in simple chronic otitis media: Should we reconstruct or leave it be? *Clinical Otolaryngology*, 43(1):300–305, February 2018.

[10] Anand V. Kasbekar, Virjen Patel, Mihiri Rubasinghe, and Venkat Srinivasan. The Surgical Management of Tympanic Membrane Retraction Pockets Using Cartilage Tympanoplasty. *Indian Journal of Otolaryngology and Head & Neck Surgery*, 66(4):449–454, December 2014.

[11] Vincent Van Rompaey, Gerd Claes, Thomas Somers, and Erwin Offeciers. Erosion of the Long Process of the Incus in Revision Stapes Surgery: Malleovestibular Prosthesis or Incus Reconstruction With Hydroxyapatite Bone Cement? *Otology & Neurotology*, 32(6):914–918, August 2011.

[12] Ghodrat Mohammadi, Masoud Naderpour, and Mehrnoosh Mousaviagdas. Ossicular erosion in patients requiring surgery for cholesteatoma. *Iranian Journal of Otorhinolaryngology*, 24(68):125–128, 2012.

[13] Hun Yi Park, Dong Hee Han, Jong Bin Lee, Nam Soo Han, Yun-Hoon Choung, and Keehyun Park. Congenital stapes anomalies with normal eardrum. *Clinical and Experimental Otorhinolaryngology*, 2(1):33–38, March 2009.

[14] John W. House, J. Eric Lupo, and John C. Goddard. Management of Incus Necrosis in Revision Stapedectomy Using Hydroxyapatite Bone Cement:. *Otology & Neurotology*, 35(8):1312–1316, September 2014.

[15] Stefan Delrue, Nicolas Verhaert, Joost van Dinther, Andrzej Zarowski, Thomas Somers, Christian Desloovere, and Erwin Offeciers. Surgical Management and Hearing Outcome of Traumatic Ossicular Injuries. *The Journal of International Advanced Otology*, 12(3):231–236, December 2016.

[16] P. Meriot, F. Veillon, J. F. Garcia, M. Nonent, J. Jezequel, P. Bourjat, and M. Bellet. CT appearances of ossicular injuries. *Radiographics: A Review Publication of the Radiological Society of North America, Inc*, 17(6):1445–1454, 1997 Nov-Dec.

[17] D. S. Grewal, Bachi T. Hathiram, Alok V. Moliorikar, Santhosli Davis, and T. Rajeevan. Retraction pockets in chronic suppurative otitis media- our experience. *Indian Journal of Otolaryngology and Head and Neck Surgery: Official Publication of the Association of Otolaryngologists of India*, 55(2):107–112, April 2003.

[18] Ritvik P. Mehta, John J. Rosowski, Susan E. Voss, Ellen O'Neil, and Saumil N. Merchant. Determinants of hearing loss in perforations of the tympanic membrane. *Otology & Neurotology: Official Publication of the American Otological Society, American Neurotology Society [and] European Academy of Otology and Neurotology*, 27(2):136–143, February 2006.

[19] Saumil N. Merchant and John J. Rosowski. Conductive hearing loss caused by third-window lesions of the inner ear. *Otology & Neurotology: Official Publication of the American Otological Society, American Neurotology Society [and] European Academy of Otology and Neurotology*, 29(3):282–289, April 2008.

[20] Anthony A. Mikulec, Michael J. McKenna, Mitchell J. Ramsey, John J. Rosowski, Barbara S. Herrmann, Steven D. Rauch, Hugh D. Curtin, and Saumil N. Merchant. Superior semicircular canal dehiscence presenting as conductive hearing loss without vertigo. *Otology & Neurotology: Official Publication of the American Otological Society, American Neurotology Society [and] European Academy of Otology and Neurotology*, 25(2):121–129, March 2004.

[21] Saumil N. Merchant, John J. Rosowski, and Michael J. McKenna. Superior Semicircular Canal Dehiscence Mimicking Otosclerotic Hearing Loss. In W. Arnold and R. Häusler, editors, *Advances in Oto-Rhino-Laryngology*, pages 137–145. KARGER, Basel, 2007.

[22] Akinori Kashio, Ken Ito, Akinobu Kakigi, Shotaro Karino, Shin-ichi Iwasaki, Takashi Sakamoto, Takuya Yasui, Mitsuya Suzuki, and Tatsuya Yamasoba. Carhart Notch 2-kHz Bone Conduction Threshold Dip: A Nondefinitive Predictor of Stapes Fixation in Conductive Hearing Loss With Normal Tympanic Membrane. *Archives of Otolaryngology–Head & Neck Surgery*, 137(3):236, March 2011.

[23] Robert H. Withnell, Pierre Parent, Patricia S. Jeng, and Jont B. Allen. Using wideband reflectance to measure the impedance of the middle ear:. *The Hearing Journal*, 62(10):36, October 2009.

[24] Gabrielle R. Merchant, Saumil N. Merchant, John J. Rosowski, and Hideko Heidi Nakajima. Controlled exploration of the effects of conductive hearing loss on wideband acoustic immittance in human cadaveric preparations. *Hearing Research*, 341:19–30, November 2016.

[25] Hideko Heidi Nakajima, John J. Rosowski, Navid Shahnaz, and Susan E. Voss. Assessment of ear disorders using power reflectance. *Ear and Hearing*, 34 Suppl 1:48S–53S, July 2013.

[26] Hideko H. Nakajima, Dominic V. Pisano, Christof Roosli, Mohamad A. Hamade, Gabrielle R. Merchant, Lorice Mahfoud, Christopher F. Halpin, John J. Rosowski, and Saumil N. Merchant. Comparison of Ear-Canal Reflectance and Umbo Velocity in Patients With Conductive Hearing Loss: A Preliminary Study:. *Ear and Hearing*, 33(1):35–43, January 2012.

[27] M. Patrick Feeney, Bert Stover, Douglas H. Keefe, Angela C. Garinis, Jessica E. Day, and Noah Seixas. Sources of Variability in Wideband Energy Reflectance Measurements in Adults. *Journal of the American Academy of Audiology*, 25(5):449–461, May 2014.

[28] Edward Onusko. Tympanometry. *American Family Physician*, 70(9):1713–1720, November 2004.

[29] A F Fercher, W Drexler, C K Hitzenberger, and T Lasser. Optical coherence tomography - principles and applications. *Reports on Progress in Physics*, 66(2):239–303, February 2003.

[30] Danielle J. Harper, Marco Augustin, Antonia Lichtenegger, Pablo Eugui, Carlos Reyes, Martin Glösmann, Christoph K. Hitzenberger, and Bernhard Baumann. White light polarization sensitive optical coherence tomography for sub-micron axial resolution and spectroscopic contrast in the murine retina. *Biomedical Optics Express*, 9(5):2115, May 2018.

[31] D. Huang, E. A. Swanson, C. P. Lin, J. S. Schuman, W. G. Stinson, W. Chang, M. R. Hee, T. Flotte, K. Gregory, and C. A. Puliafito. Optical coherence tomography. *Science (New York, N.Y.)*, 254(5035):1178–1181, November 1991.

[32] Michael Choma, Marinko Sarunic, Changhuei Yang, and Joseph Izatt. Sensitivity advantage of swept source and Fourier domain optical coherence tomography. *Optics Express*, 11(18):2183, September 2003.

[33] R. Leitgeb, C. Hitzenberger, and Adolf Fercher. Performance of fourier domain vs time domain optical coherence tomography. *Optics Express*, 11(8):889, April 2003.

[34] Kathy Zheng, Bin Liu, Chuanyong Huang, and Mark E. Brezinski. Experimental confirmation of potential swept source optical coherence tomography performance limitations. *Applied Optics*, 47(33):6151, November 2008.

[35] B. E. Bouma, G. J. Tearney, B. J. Vakoc, and S. H. Yun. Optical Frequency Domain Imaging. In Elias Greenbaum, Wolfgang Drexler, and James G. Fujimoto, editors, *Optical Coherence Tomography*, pages 209–237. Springer Berlin Heidelberg, Berlin, Heidelberg, 2008.

[36] Seok Hyun Yun and Brett E. Bouma. Wavelength Swept Lasers. In Wolfgang Drexler and James G. Fujimoto, editors, *Optical Coherence Tomography*, pages 619–637. Springer International Publishing, Cham, 2015.

[37] Thomas Klein and Robert Huber. High-speed OCT light sources and systems [Invited]. *Biomedical Optics Express*, 8(2):828, February 2017.

[38] Robert B. Northrop. *Introduction to Instrumentation and Measurements*. Taylor & Francis, Boca Raton, 2nd ed edition, 2005.

[39] Rong Z. Gan, Mark W. Wood, and Kenneth J. Dormer. Human Middle Ear Transfer Function Measured by Double Laser Interferometry System:. *Otology & Neurotology*, 25(4):423–435, July 2004.

[40] S. E. Voss, J. J. Rosowski, S. N. Merchant, and W. T. Peake. Acoustic responses of the human middle ear. *Hearing Research*, 150(1-2):43–69, December 2000.

[41] Irina Arechvo, Nikoloz Lasurashvili, Matthias Bornitz, Zurab Kevanishvili, and Thomas Zahnert. Laser Doppler vibrometry of the middle ear in humans: Derivation dependence, variability, and bilateral differences. *Medicina (Kaunas, Lithuania)*, 45(11):878–886, 2009.

[42] Jae Hoon Sim, Michail Chatzimichalis, Michael Lauxmann, Christof Röösli, Albrecht Eiber, and Alexander M. Huber. Complex stapes motions in human ears. *Journal of the Association for Research in Otolaryngology: JARO*, 11(3):329–341, September 2010.

[43] Naohito Hato, Stefan Stenfelt, and Richard L. Goode. Three-dimensional stapes footplate motion in human temporal bones. *Audiology & Neuro-Otology*, 8(3):140–152, 2003 May-Jun.

[44] Morteza Khaleghi, Jeffrey Tao Cheng, Cosme Furlong, and John J. Rosowski. In-plane and out-of-plane motions of the human tympanic membrane. *The Journal of the Acoustical Society of America*, 139(1):104–117, January 2016.

[45] A. Huber, T. Linder, M. Ferrazzini, S. Schmid, N. Dillier, S. Stoeckli, and U. Fisch. Intraoperative assessment of stapes movement. *The Annals of Otology, Rhinology, and Laryngology*, 110(1):31–35, January 2001.

[46] Wade Chien, John J. Rosowski, Michael E. Ravicz, Steven D. Rauch, Jennifer Smullen, and Saumil N. Merchant. Measurements of stapes velocity in live human ears. *Hearing Research*, 249(1-2):54–61, March 2009.

[47] Wade Chien, Michael E. Ravicz, Saumil N. Merchant, and John J. Rosowski. The effect of methodological differences in the measurement of stapes motion in live and cadaver ears. *Audiology & Neuro-Otology*, 11(3):183–197, 2006.

[48] Yasuomi Kunimoto, Kensaku Hasegawa, Shiro Arii, Hideyuki Kataoka, Hiroaki Yazama, Junko Kuya, Kazunori Fujiwara, and Hiromi Takeuchi. Sequential motion of the ossicular chain measured by laser Doppler vibrometry. *Acta Oto-Laryngologica*, 137(12):1233–1237, December 2017.

[49] Michael D. Seidman, Robert T. Standring, Syed Ahsan, Sam Marzo, Jack Shohet, Catherine Lumley, and Kevin Verzal. Normative data of incus and stapes displacement during middle ear surgery using laser Doppler vibrometry. *Otology & Neurotology: Official Publication of the American Otological Society, American Neurotology Society [and] European Academy of Otology and Neurotology*, 34(9):1719–1724, December 2013.

[50] Jacek Sokołowski, Kazimierz Niemczyk, Robert Bartoszewicz, Krzysztof Morawski, and Antoni Bruzgielewicz. [Method of ossicular chain valuation. Experimental measurement and clinical application]. *Otolaryngologia Polska = The Polish Otolaryngology*, 63(5):432–436, 2009 Sep-Oct.

[51] Krzysztof Morawski, Kazimierz Niemczyk, Jacek Sokolowski, Aleksandra Hryciuk, and Robert Bartoszewicz. Intraoperative Monitoring of Hearing Improvement during Ossiculoplasty by Laser-Doppler Vibrometry, Auditory Brainstem Responses, and Electrocochleography. *Otolaryngology–Head and Neck Surgery*, 150(6):1043–1047, June 2014.

[52] R. L. Goode, G. Ball, and S. Nishihara. Measurement of umbo vibration in human subjects–method and possible clinical applications. *The American Journal of Otology*, 14(3):247–251, May 1993.

[53] N. Stasche, H. J. Foth, K. Hörmann, A. Baker, and C. Huthoff. Middle ear transmission disorders–tympanic membrane vibration analysis by laser-Doppler-vibrometry. *Acta Oto-Laryngologica*, 114(1):59–63, January 1994.

[54] Kenneth R. Whittemore, Saumil N. Merchant, Becky B. Poon, and John J. Rosowski. A normative study of tympanic membrane motion in humans using a laser Doppler vibrometer (LDV). *Hearing Research*, 187(1-2):85–104, January 2004.

[55] John J. Rosowski, Ritvik P. Mehta, and Saumil N. Merchant. Diagnostic utility of laser-Doppler vibrometry in conductive hearing loss with normal tympanic membrane. *Otology & Neurotology: Official Publication of the American Otological Society, American Neurotology Society [and] European Academy of Otology and Neurotology*, 24(2):165–175, March 2003.

[56] J.J. Rosowski, S.N. Merchant, and H.H. Nakajima. THE USE OF LASER - DOPPLER VIBROMETRY IN HUMAN MIDDLE - EAR RESEARCH: THE EFFECTS OF ALTERATIONS IN MIDDLE - EAR LOAD. In *Middle Ear Mechanics in Research and Otology*, pages 27–34, Matsuyama, Ehime, Japan, July 2004. WORLD SCIENTIFIC.

[57] A. M. Huber, C. Schwab, T. Linder, S. J. Stoeckli, M. Ferrazzini, N. Dillier, and U. Fisch. Evaluation of eardrum laser doppler interferometry as a diagnostic tool. *The Laryngoscope*, 111(3):501–507, March 2001.

[58] Hideko Heidi Nakajima, Michael E. Ravicz, Saumil N. Merchant, William T. Peake, and John J. Rosowski. Experimental ossicular fixations and the middle ear's response to sound: Evidence for a flexible ossicular chain. *Hearing Research*, 204(1-2):60–77, June 2005.

[59] John J. Rosowski, Hideko H. Nakajima, Mohamad A. Hamade, Lorice Mahfoud, Gabrielle R. Merchant, Christopher F. Halpin, and Saumil N. Merchant. Ear-Canal Reflectance, Umbo Velocity, and Tympanometry in Normal-Hearing Adults:. *Ear and Hearing*, 33(1):19–34, January 2012.

[60] C. Pitris, K. T. Saunders, J. G. Fujimoto, and M. E. Brezinski. High-resolution imaging of the middle ear with optical coherence tomography: A feasibility

study. *Archives of Otolaryngology–Head & Neck Surgery*, 127(6):637–642, June 2001.

[61] Brian J. Wong, Johannes F. de Boer, Boris H. Park, Zhongping Chen, and J. Stuart Nelson. Optical coherence tomography of the rat cochlea: Preliminary investigations. In R. Rox Anderson, Kenneth E. Bartels, Lawrence S. Bass, Darryl J. Bornhop, C. Gaelyn Garrett, Kenton W. Gregory, Nikiforos Kollias, Harvey Lui, Reza S. Malek, Aaron P. Perlmutter, Hans-Dieter Reidenbach, Lou Reinisch, David S. Robinson, Lloyd P. Tate, and Eugene A. Trowers, editors, *BiOS '99 International Biomedical Optics Symposium*, page 261, San Jose, CA, June 1999.

[62] Brian J. F. Wong, Johannes F. de Boer, B. Hyle Park, Zhongping Chen, and J. Stuart Nelson. Optical coherence tomography of the rat cochlea. *Journal of Biomedical Optics*, 5(4):367, 2000.

[63] Brian J. f Wong, Yonghua Zhao, Mark Yamaguchi, Nader Nassif, Zhongping Chen, and Johannes F. De Boer. Imaging the internal structure of the rat cochlea using optical coherence tomography at 0.827 microm and 1.3 microm. *Otolaryngology–Head and Neck Surgery: Official Journal of American Academy of Otolaryngology-Head and Neck Surgery*, 130(3):334–338, March 2004.

[64] Mark K. Yamaguchi, Johannes F. de Boer, Boris H. Park, Nader Nassif, Yonghua Zhao, Zhongping Chen, and Brian J. Wong. Imaging the internal structure of the guinea pig cochlea using optical coherence tomography at 1310 nm. In R. Rox Anderson, Kenneth E. Bartels, Lawrence S. Bass, C. Gaelyn Garrett, Kenton W. Gregory, Abraham Katzir, Nikiforos Kollias, Michael D. Lucroy, Reza S. Malek, J. Stuart Nelson, George M. Peavy, Hans-Dieter Reidenbach, Lou Reinisch, David S. Robinson, Lloyd P. Tate, Eugene A. Trowers, and Timothy A. Woodward, editors, *BiOS 2001 The International Symposium on Biomedical Optics*, page 372, San Jose, CA, May 2001.

[65] Ali Sepehr, Hamid R. Djalilian, Janice E. Chang, Zhongping Chen, and Brian J. F. Wong. Optical Coherence Tomography of the Cochlea in the Porcine Model. *The Laryngoscope*, 118(8):1449–1451, August 2008.

[66] >Hans Wilhelm Pau, Eva Lankenau, Tino Just, Detlef Behrend, and Gereon Hüttmann. Optical coherence tomography as an orientation guide in cochlear implant surgery? *Acta Oto-Laryngologica*, 127(9):907–913, January 2007.

[67] James Lin, Hinrich Staecker, and M. Samir Jafri. Optical coherence tomography imaging of the inner ear: A feasibility study with implications for cochlear implantation. *The Annals of Otology, Rhinology, and Laryngology*, 117(5):341–346, May 2008.

[68] T. Just, E. Lankenau, G. Hüttmann, and H. W. Pau. [Intraoperative application of optical coherence-tomography (OCT) for visualization of the oval window niche]. *Laryngo- Rhino- Otologie*, 88(3):168–173, March 2009.

[69] T. Just, E. Lankenau, G. Hüttmann, and H. W. Pau. Optical coherence tomography of the oval window niche. *The Journal of Laryngology and Otology*, 123(6):603–608, June 2009.

[70] Hamid R. Djalilian, Marc Rubinstein, Edward C. Wu, Kaveh Naemi, Shawn Zardouz, Koohyar Karimi, and Brian J. F. Wong. Optical coherence tomography of cholesteatoma. *Otology & Neurotology: Official Publication of the American Otological Society, American Neurotology Society [and] European Academy of Otology and Neurotology*, 31(6):932–935, August 2010.

[71] Hamid R. Djalilian, James Ridgway, Majestic Tam, Ali Sepehr, Zhongping Chen, and Brian J. F. Wong. Imaging the Human Tympanic Membrane Using Optical Coherence Tomography In Vivo:. *Otology & Neurotology*, 29(8):1091–1094, December 2008.

[72] Sam Van der Jeught, Joris J. J. Dirckx, Johan R. M. Aerts, Adrian Bradu, Adrian G. H. Podoleanu, and Jan A. N. Buytaert. Full-field thickness distribution of human tympanic membrane obtained with optical coherence tomography. *Journal of the Association for Research in Otolaryngology: JARO*, 14(4):483–494, August 2013.

[73] Zita Hubler, Nathan D. Shemonski, Ryan L. Shelton, Guillermo L. Monroy, Ryan M. Nolan, and Stephen A. Boppart. Real-time automated thickness measurement of the in vivo human tympanic membrane using optical coherence tomography. *Quantitative Imaging in Medicine and Surgery*, 5(1):69–77, February 2015.

[74] Paritosh Pande, Ryan L. Shelton, Guillermo L. Monroy, Ryan M. Nolan, and Stephen A. Boppart. A Mosaicking Approach for In Vivo Thickness Mapping of the Human Tympanic Membrane Using Low Coherence Interferometry. *Journal of the Association for Research in Otolaryngology: JARO*, 17(5):403–416, October 2016.

[75] Chuanwu Xi, Daniel Marks, Simon Schlachter, Wei Luo, and Stephen A. Boppart. High-resolution three-dimensional imaging of biofilm development using optical coherence tomography. *Journal of Biomedical Optics*, 11(3):34001, 2006 May-Jun.

[76] Cac T. Nguyen, Sarah R. Robinson, Woonggyu Jung, Michael A. Novak, Stephen A. Boppart, and Jont B. Allen. Investigation of bacterial biofilm in the human middle ear using optical coherence tomography and acoustic measurements. *Hearing Research*, 301:193–200, July 2013.

[77] Ryan L. Shelton, Woonggyu Jung, Samir I. Sayegh, Daniel T. McCormick, Jeehyun Kim, and Stephen A. Boppart. Optical coherence tomography for advanced screening in the primary care office. *Journal of Biophotonics*, 7(7):525–533, July 2014.

[78] C. T. Nguyen, W. Jung, J. Kim, E. J. Chaney, M. Novak, C. N. Stewart, and S. A. Boppart. Noninvasive in vivo optical detection of biofilm in the human middle ear. *Proceedings of the National Academy of Sciences*, 109(24):9529–9534, June 2012.

[79] Guillermo L. Monroy, Paritosh Pande, Ryan M. Nolan, Ryan L. Shelton, Ryan G. Porter, Michael A. Novak, Darold R. Spillman, Eric J. Chaney, Daniel T. McCormick, and Stephen A. Boppart. Noninvasive in vivo optical coherence tomography tracking of chronic otitis media in pediatric subjects after surgical intervention. *Journal of Biomedical Optics*, 22(12):1, December 2017.

[80] Guillermo L. Monroy, Jungeun Won, Roshan Dsouza, Paritosh Pande, Malcolm C. Hill, Ryan G. Porter, Michael A. Novak, Darold R. Spillman, and Stephen A. Boppart. Automated classification platform for the identification of otitis media using optical coherence tomography. *npj Digital Medicine*, 2(1):22, December 2019.

[81] Guillermo L. Monroy, Paritosh Pande, Ryan L. Shelton, Ryan M. Nolan, Darold R. Spillman, Ryan G. Porter, Michael A. Novak, and Stephen A. Boppart. Non-invasive optical assessment of viscosity of middle ear effusions in otitis media. *Journal of Biophotonics*, 10(3):394–403, March 2017.

[82] Nam Hyun Cho, Sang Heun Lee, Woonggyu Jung, Jeong Hun Jang, Stephen A. Boppart, and Jeehyun Kim. Optical coherence tomography for the diagnosis and evaluation of human otitis media. *Journal of Korean Medical Science*, 30(6):834, June 2015.

[83] Dan MacDougall, Joshua Farrell, Jeremy Brown, Manohar Bance, and Robert Adamson. Long-range, wide-field swept-source optical coherence tomography with GPU accelerated digital lock-in Doppler vibrography for real-time, in vivo middle ear diagnostics. *Biomedical Optics Express*, 7(11):4621–4635, November 2016.

[84] Wihan Kim, Sangmin Kim, Shuning Huang, John S. Oghalai, and Brian E. Applegate. Picometer scale vibrometry in the human middle ear using a surgical microscope based optical coherence tomography and vibrometry system. *Biomedical Optics Express*, 10(9):4395, September 2019.

[85] Michal E. Pawlowski, Sebina Shrestha, Jesung Park, Brian E. Applegate, John S. Oghalai, and Tomasz S. Tkaczyk. Miniature, minimally invasive, tunable endoscope for investigation of the middle ear. *Biomedical Optics Express*, 6(6):2246–2257, June 2015.

[86] Anke Burkhardt, Julia Walther, Peter Cimalla, Mirko Mehner, and Edmund Koch. Endoscopic optical coherence tomography device for forward imaging

with broad field of view. *Journal of Biomedical Optics*, 17(7):071302, July 2012.

[87] Woonggyu Jung, Jeehyun Kim, Mansik Jeon, Eric J. Chaney, Charles N. Stewart, and Stephen A. Boppart. Handheld optical coherence tomography scanner for primary care diagnostics. *IEEE transactions on bio-medical engineering*, 58(3):741–744, March 2011.

[88] Jesung Park, Jeffrey T. Cheng, Daniel Ferguson, Gopi Maguluri, Ernest W. Chang, Caitlin Clancy, Daniel J. Lee, and Nicusor Iftimia. Investigation of middle ear anatomy and function with combined video otoscopy-phase sensitive OCT. *Biomedical Optics Express*, 7(2):238–250, February 2016.

[89] Ernest W. Chang, James B. Kobler, and Seok H. Yun. Subnanometer optical coherence tomographic vibrography. *Optics Letters*, 37(17):3678, September 2012.

[90] Stanley S. Hong and Dennis M. Freeman. Doppler optical coherence microscopy for studies of cochlear mechanics. *Journal of Biomedical Optics*, 11(5):054014, 2006.

[91] Niloy Choudhury, Guiju Song, Fangyi Chen, Scott Matthews, Tanja Tschinkel, Jiefu Zheng, Steven L. Jacques, and Alfred L. Nuttall. Low coherence interferometry of the cochlear partition. *Hearing Research*, 220(1-2):1–9, October 2006.

[92] Wihan Kim, Sangmin Kim, John S. Oghalai, and Brian E. Applegate. Endoscopic optical coherence tomography enables morphological and subnanometer vibratory imaging of the porcine cochlea through the round window. *Optics Letters*, 43(9):1966, May 2018.

[93] Fangyi Chen, Niloy Choudhury, Jiefu Zheng, Scott Matthews, Alfred L. Nutall, and Steven L. Jacques. In vivo imaging and low-coherence interferometry of organ of Corti vibration. *Journal of Biomedical Optics*, 12(2):021006, 2007.

[94] Hee Yoon Lee, Patrick D. Raphael, Jesung Park, Audrey K. Ellerbee, Brian E. Applegate, and John S. Oghalai. Noninvasive in vivo imaging reveals differences between tectorial membrane and basilar membrane traveling waves in the mouse cochlea. *Proceedings of the National Academy of Sciences*, 112(10):3128–3133, March 2015.

[95] Fangyi Chen, Dingjun Zha, Anders Fridberger, Jiefu Zheng, Niloy Choudhury, Steven L Jacques, Ruikang K Wang, Xiaorui Shi, and Alfred L Nuttall. A differentially amplified motion in the ear for near-threshold sound detection. *Nature Neuroscience*, 14(6):770–774, June 2011.

[96] Dingjun Zha, Fangyi Chen, Sripriya Ramamoorthy, Anders Fridberger, Niloy Choudhury, Steven L. Jacques, Ruikang K. Wang, and Alfred L. Nuttall. In Vivo Outer Hair Cell Length Changes Expose the Active Process in the Cochlea. *PLoS ONE*, 7(4):e32757, April 2012.

[97] S. Ramamoorthy, D. Zha, F. Chen, S. L. Jacques, R. Wang, N. Choudhury, A. L. Nuttall, and A. Fridberger. Filtering of Acoustic Signals within the Hearing Organ. *Journal of Neuroscience*, 34(27):9051–9058, July 2014.

[98] H. Y. Lee, P. D. Raphael, A. Xia, J. Kim, N. Grillet, B. E. Applegate, A. K. Ellerbee Bowden, and J. S. Oghalai. Two-Dimensional Cochlear Micromechanics Measured In Vivo Demonstrate Radial Tuning within the Mouse Organ of Corti. *Journal of Neuroscience*, 36(31):8160–8173, August 2016.

[99] Tianying Ren, Wenxuan He, and Peter G. Barr-Gillespie. Reverse transduction measured in the living cochlea by low-coherence heterodyne interferometry. *Nature Communications*, 7(1):10282, April 2016.

[100] Yanli Wang, Charles R. Steele, and Sunil Puria. Cochlear Outer-Hair-Cell Power Generation and Viscous Fluid Loss. *Scientific Reports*, 6(1):19475, May 2016.

[101] Anping Xia, Xiaofang Liu, Patrick D. Raphael, Brian E. Applegate, and John S. Oghalai. Hair cell force generation does not amplify or tune vibrations within the chicken basilar papilla. *Nature Communications*, 7(1):13133, December 2016.

[102] Alberto Recio-Spinoso and John S. Oghalai. Mechanical tuning and amplification within the apex of the guinea pig cochlea: Tuning and amplification in the cochlear apex. *The Journal of Physiology*, 595(13):4549–4561, July 2017.

[103] Zina Jawadi, Brian E. Applegate, and John S. Oghalai. Optical Coherence Tomography to Measure Sound-Induced Motions Within the Mouse Organ of Corti In Vivo. In Bernd Sokolowski, editor, *Auditory and Vestibular Research*, volume 1427, pages 449–462. Springer New York, New York, NY, 2016.

[104] Simon S. Gao, Rosalie Wang, Patrick D. Raphael, Yalda Moayedi, Andrew K. Groves, Jian Zuo, Brian E. Applegate, and John S. Oghalai. Vibration of the organ of Corti within the cochlear apex in mice. *Journal of Neurophysiology*, 112(5):1192–1204, September 2014.

[105] Brian E. Applegate, Ryan L. Shelton, Simon S. Gao, and John S. Oghalai. Imaging high-frequency periodic motion in the mouse ear with coherently interleaved optical coherence tomography. *Optics Letters*, 36(23):4716, December 2011.

[106] Jesung Park, Esteban F. Carbajal, Xi Chen, John S. Oghalai, and Brian E. Applegate. Phase-sensitive optical coherence tomography using an Vernier-tuned distributed Bragg reflector swept laser in the mouse middle ear. *Optics Letters*, 39(21):6233, November 2014.

[107] Anke Burkhardt, Lars Kirsten, Matthias Bornitz, Thomas Zahnert, and Edmund Koch. Investigation of the human tympanic membrane oscillation *ex vivo* by Doppler optical coherence tomography: Investigation of the human tympanic membrane oscillation. *Journal of Biophotonics*, 7(6):434–441, June 2014.

[108] Antoine Ramier, Jeffrey Tao Cheng, Michael E. Ravicz, John J. Rosowski, and Seok-Hyun Yun. Mapping the phase and amplitude of ossicular chain motion using sound-synchronous optical coherence vibrography. *Biomedical Optics Express*, 9(11):5489, November 2018.

[109] Lars Kirsten, Martin Schindler, Joseph Morgenstern, Mikael Timo Erkkilä, Jonas Golde, Julia Walther, Pascal Rottmann, Max Kemper, Matthias Bornitz, Marcus Neudert, Thomas Zahnert, and Edmund Koch. Endoscopic optical coherence tomography with wide field-of-view for the morphological and functional assessment of the human tympanic membrane. *Journal of Biomedical Optics*, 24(03):1, December 2018.

[110] Ernest W. Chang, Jeffrey T. Cheng, Christof Röösli, James B. Kobler, John J. Rosowski, and Seok Hyun Yun. Simultaneous 3D imaging of sound-induced motions of the tympanic membrane and middle ear ossicles. *Hearing Research*, 304:49–56, October 2013.

[111] Lars Kirsten, Anke Burkhardt, Jonas Golde, Julia Walther, Thomas Stoppe, Matthias Bornitz, Max Kemper, Thomas Zahnert, and Edmund Koch. Imaging the tympanic membrane oscillation ex vivo with Doppler optical coherence tomography during simulated Eustachian catarrh. In Brett E. Bouma and Maciej Wojtkowski, editors, *European Conferences on Biomedical Optics*, page 95410R, Munich, Germany, July 2015.

[112] Lars Kirsten, Simon Baumgärtner, Mikael Timo Erkkilä, Jonas Golde, Max Kemper, Thomas Stoppe, Matthias Bornitz, Marcus Neudert, Thomas Zahnert, and Edmund Koch. Doppler optical coherence tomography as a promising tool for detecting fluid in the human middle ear. *Current Directions in Biomedical Engineering*, 2(1), January 2016.

[113] Hrebesh M. Subhash, Anh Nguyen-Huynh, Ruikang K. Wang, Steven L. Jacques, Niloy Choudhury, and Alfred L. Nuttall. Feasibility of spectral-domain phase-sensitive optical coherence tomography for middle ear vibrometry. *Journal of Biomedical Optics*, 17(6):060505, 2012.

[114] Z. Torbatian, P. Garland, R. B. A. Adamson, M. Bance, J. A. Brown, Christopher A. Shera, and Elizabeth S. Olson. Direct Measurement of Basilar Membrane Motion Using Pulsed-Wave Doppler High-Frequency Ultrasound. In *WHAT FIRE IS IN MINE EARS: PROGRESS IN AUDITORY BIOMECHANICS: Proceedings of the 11th International Mechanics of Hearing Workshop*, pages 430–431, Williamstown, Massachusetts (USA), 2011.

[115] Zahra Torbatian, Phil Garland, Rob Adamson, Julian Savage, Manohar Bance, and Jeremy Brown. Listening to the Cochlea With High-Frequency Ultrasound. *Ultrasound in Medicine & Biology*, 38(12):2208–2217, December 2012.

[116] Jeremy A. Brown, Zahra Torbatian, Robert B. Adamson, Rene Van Wijhe, Ronald J. Pennings, Geoffrey R. Lockwood, and Manohar L. Bance. High-Frequency Ex vivo Ultrasound Imaging of the Auditory System. *Ultrasound in Medicine & Biology*, 35(11):1899–1907, November 2009.

[117] Dan MacDougall, James Rainsbury, Jeremy Brown, Manohar Bance, and Robert Adamson. Optical coherence tomography system requirements for clinical diagnostic middle ear imaging. *Journal of Biomedical Optics*, 20(5):056008, May 2015.

[118] Bin Liu and Mark E. Brezinski. Theoretical and practical considerations on detection performance of time domain, Fourier domain, and swept source optical coherence tomography. *Journal of Biomedical Optics*, 12(4):044007, 2007 Jul-Aug.

[119] Elena Salomatina, Brian Jiang, John Novak, and Anna N. Yaroslavsky. Optical properties of normal and cancerous human skin in the visible and near-infrared spectral range. *Journal of Biomedical Optics*, 11(6):064026, 2006.

[120] W. Drexler, U. Morgner, R. K. Ghanta, F. X. Kärtner, J. S. Schuman, and J. G. Fujimoto. Ultrahigh-resolution ophthalmic optical coherence tomography. *Nature Medicine*, 7(4):502–507, April 2001.

[121] Andrew M. Rollins and Joseph A. Izatt. Optimal interferometer designs for optical coherence tomography. *Optics Letters*, 24(21):1484, November 1999.

[122] G. J. Tearney, B. E. Bouma, and J. G. Fujimoto. High-speed phase- and group-delay scanning with a grating-based phase control delay line. *Optics Letters*, 22(23):1811, December 1997.

[123] K.K.M.B.D. Silva, A.V. Zvyagin, and D.D. Sampson. Extended range, rapid scanning optical delay line for biomedical interferometric imaging. *Electronics Letters*, 35(17):1404, 1999.

[124] Wanrong Gao. Dispersion properties of grating-based rapid scanning optical delay lines. *Applied Optics*, 46(6):986, February 2007.

[125] Lihong V. Wang and Hsin-I Wu. *Biomedical Optics: Principles and Imaging*. John Wiley & Sons, Inc., Hoboken, NJ, USA, July 2009.

[126] Hans-Jochen Foth, Silke Färber, Axel Gauer, and Rudolf Wagner. Thermal damage threshold at 633 nm of tympanic membrane of pig. *Hearing Research*, 142(1-2):71–78, April 2000.

[127] Steven L Jacques. Optical properties of biological tissues: A review. *Physics in Medicine and Biology*, 58(11):R37–R61, June 2013.

[128] G. Robertson and R. Mills. Findings at exploratory tympanotomy for conductive hearing loss. *The Journal of Laryngology and Otology*, 123(10):1087–1089, October 2009.

[129] A. E. Desjardins, B. J. Vakoc, G. J. Tearney, and B. E. Bouma. Speckle Reduction in OCT using Massively-Parallel Detection and Frequency-Domain Ranging. *Optics Express*, 14(11):4736, 2006.

[130] J. M. Schmitt and S. H. Xiang. Cross-polarized backscatter in optical coherence tomography of biological tissue. *Optics Letters*, 23(13):1060, July 1998.

[131] J. M. Schmitt and A. Knüttel. Model of optical coherence tomography of heterogeneous tissue. *Journal of the Optical Society of America A*, 14(6):1231, June 1997.

[132] Yuankai K. Tao, Sunil K. Srivastava, and Justis P. Ehlers. Microscope-integrated intraoperative OCT with electrically tunable focus and heads-up display for imaging of ophthalmic surgical maneuvers. *Biomedical Optics Express*, 5(6):1877, June 2014.

[133] Tyler S. Ralston, Daniel L. Marks, P. Scott Carney, and Stephen A. Boppart. Interferometric synthetic aperture microscopy. *Nature Physics*, 3(2):129–134, February 2007.

[134] Maciej Wojtkowski. High-speed optical coherence tomography: Basics and applications. *Applied Optics*, 49(16):D30, June 2010.

[135] Ruikang K. Wang and Valery V. Tuchin. Optical Tissue Clearing to Enhance Imaging Performance for OCT. In Wolfgang Drexler and James G. Fujimoto, editors, *Optical Coherence Tomography*, pages 1455–1487. Springer International Publishing, Cham, 2015.

[136] Desmond C. Adler, Wolfgang Wieser, Francois Trepanier, Joseph M. Schmitt, and Robert A. Huber. Coherence length extension of Fourier domain mode locked lasers. In Joseph A. Izatt, James G. Fujimoto, and Valery V. Tuchin, editors, *SPIE BiOS*, page 82130O, San Francisco, California, USA, February 2012.

[137] M. Bonesi, M. P. Minneman, J. Ensher, B. Zabihian, H. Sattmann, P. Boschert, E. Hoover, R. A. Leitgeb, M. Crawford, and W. Drexler. Akinetic all-semiconductor programmable swept-source at 1550 nm and 1310 nm with centimeters coherence length. *Optics Express*, 22(3):2632, February 2014.

[138] Roman V. Kuranov, Austin B. McElroy, Nate Kemp, Stepan Baranov, Joe Taber, Marc D. Feldman, and Thomas E. Milner. Gas-Cell Referenced Swept Source Phase Sensitive Optical Coherence Tomography. *IEEE Photonics Technology Letters*, 22(20):1524–1526, October 2010.

[139] Shaozhen Song, Jingjiang Xu, and Ruikang K. Wang. Long-range and wide field of view optical coherence tomography for in vivo 3D imaging of large volume object based on akinetic programmable swept source. *Biomedical Optics Express*, 7(11):4734, November 2016.

[140] Zhao Wang, Benjamin Potsaid, Long Chen, Chris Doerr, Hsiang-Chieh Lee, Torben Nielson, Vijaysekhar Jayaraman, Alex E. Cable, Eric Swanson, and James G. Fujimoto. Cubic meter volume optical coherence tomography. *Optica*, 3(12):1496, December 2016.

[141] Antoine Ramier, John J. Rosowski, and Seok-Hyun Yun. Optical coherence tomography for imaging the middle and inner ears: A technical review. In *TO THE EAR AND BACK AGAIN - ADVANCES IN AUDITORY BIOPHYSICS: Proceedings of the 13th Mechanics of Hearing Workshop*, page 020001, St Catharines, Canada, 2018.

[142] Yifan Jian, Kevin Wong, and Marinko V. Sarunic. Graphics processing unit accelerated optical coherence tomography processing at megahertz axial scan rate and high resolution video rate volumetric rendering. *Journal of Biomedical Optics*, 18(2):026002, February 2013.

[143] Kang Zhang and Jin U. Kang. Graphics processing unit-based ultrahigh speed real-time multidimensional Fourier domain optical coherence tomography. In Joseph A. Izatt, James G. Fujimoto, and Valery V. Tuchin, editors, *SPIE BiOS*, page 82132B, San Francisco, California, USA, February 2012.

[144] Dierck Hillmann, Tim Bonin, Christian Lührs, Gesa Franke, Martin Hagen-Eggert, Peter Koch, and Gereon Hüttmann. Common approach for compensation of axial motion artifacts in swept-source OCT and dispersion in Fourier-domain OCT. *Optics Express*, 20(6):6761, March 2012.

[145] W. F. Decraemer, O. de La Rochefoucauld, W. R. J. Funnell, and E. S. Olson. Three-Dimensional Vibration of the Malleus and Incus in the Living Gerbil. *Journal of the Association for Research in Otolaryngology*, April 2014.

[146] M. S. M. G. Vlaming and L. Feenstra. Studies on the mechanics of the normal human middle ear. *Clinical Otolaryngology*, 11(5):353–363, October 1986.

[147] WooJhon Choi, Benjamin Potsaid, Vijaysekhar Jayaraman, Bernhard Baumann, Ireneusz Grulkowski, Jonathan J. Liu, Chen D. Lu, Alex E. Cable, David Huang, Jay S. Duker, and James G. Fujimoto. Phase-sensitive swept-source optical coherence tomography imaging of the human retina with a vertical cavity surface-emitting laser light source. *Optics Letters*, 38(3):338, February 2013.

[148] Dan MacDougall, Loran Morrison, Christine Morrison, David P. Morris, Manohar Bance, and Robert B. A. Adamson. Optical Coherence Tomography Doppler Vibrometry Measurement of Stapes Vibration in Patients With Stapes Fixation and Normal Controls:. *Otology & Neurotology*, 40(4):e349–e355, April 2019.

[149] F. Declau, M. van Spaendonck, J.P. Timmermans, L. Michaels, J. Liang, J.P. Qiu, and P. van de Heyning. Prevalence of Histologic Otosclerosis: An Unbiased Temporal Bone Study in Caucasians. In W. Arnold and R. Häusler, editors, *Advances in Oto-Rhino-Laryngology*, pages 6–16. KARGER, Basel, 2007.

[150] Brian S. Chen and Fred H. Linthicum. Otosclerosis Without Stapes Fixation:. *Otology & Neurotology*, 36(8):e140–e141, September 2015.

[151] Chris A. Sanford, Tracy Schooling, and Tobi Frymark. Determining the Presence or Absence of Middle Ear Disorders: An Evidence-Based Systematic Review on the Diagnostic Accuracy of Selected Assessment Instruments. *American Journal of Audiology*, 21(2):251–268, December 2012.

[152] H Yasan. Predictive role of Carhart's notch in pre-operative assessment for middle-ear surgery. *The Journal of Laryngology & Otology*, 121(3):219–221, March 2007.

[153] B. Efron and R. Tibshirani. Bootstrap Methods for Standard Errors, Confidence Intervals, and Other Measures of Statistical Accuracy. *Statistical Science*, 1(1):54–75, February 1986.

[154] Douglas H. Keefe, Kelly L. Archer, Kendra K. Schmid, Denis F. Fitzpatrick, M. Patrick Feeney, and Lisa L. Hunter. Identifying Otosclerosis with Aural Acoustical Tests of Absorbance, Group Delay, Acoustic Reflex Threshold, and Otoacoustic Emissions. *Journal of the American Academy of Audiology*, 28(9):838–860, October 2017.

[155] S M Elmorsy and H E Amer. Insertion of middle-ear Silastic sheeting during tympanoplasty: Hearing outcomes. *The Journal of Laryngology & Otology*, 125(5):445–448, May 2011.

[156] Hsern Ern Ivan Tan, Peter Luke Santa Maria, Philip Wijesinghe, Brendan Francis Kennedy, Benjamin James Allardyce, Robert Henry Eikelboom, Marcus David Atlas, and Rodney James Dilley. Optical Coherence Tomography of the Tympanic Membrane and Middle Ear: A Review. *Otolaryngology–Head and Neck Surgery*, 159(3):424–438, September 2018.

Appendix A

Computed Tomography Resolution

This appendix contains cover page and page 7 from the Siemens *Syngo CT* datasheet, a reference not publicly available, but retrieved from medical physics at the QEII Hospital (VG Site) in Halifax, NS, Canada. This is an example of a typical, modern CT scanner used when an otologist or ENT orders temporal bone imaging for pre-surgical imaging. The spatial resolution, *i.e.* the required separation between two equally intense, fine, features for them to be independently resolvable is approximately the reciprocal number of resolvable line-pairs per centimeter, listed in the "Z-UHR (Ultra-High Resolution)" section at the bottom of Page 7. We take the spatial resolution of this system to then be $\approx \frac{1}{30^{\mathrm{lp/cm}}} = 333\mu$m, and treat it as representative of a modern CT scanner.

The Reference in Single Source CT

SOMATOM Definition Edge

Datasheet for *syngo* CT 2012B

Answers for life.

SIEMENS

System Hardware

Data Acquisition System	
Stellar Detector	Siemens' first fully integrated detector with TrueSignal and Edge Technology. Due to the full electronic integration of the Stellar Detector, electronic components (microchips, conductors, etc.) are integrated directly at the photo diode. This reduces electronic noise coming from the detector elements and thus significantly improves the signal-to-noise ratio (SNR) for optimized dose efficiency and image quality.
TrueSignal Technology	Due to the full electronic integration the SNR is significantly improved, allowing a much better utilization especially of low signals at the detector, e.g. in bariatric patients or low-dose imaging
Edge Technology	Due to the full electronic integration of the Stellar Detector elements, electronic cross-talk between neighbouring detector rows is reduced. This significantly reduces slice blurring, resulting in a more precise slice profile. This enables the generation of 0.5 mm slices delivering a spatial cross-plane resolution of 0.30 mm.
HiDynamics	Due to the full electronic integration of the Stellar Detector elements, the dynamic bandwidth is significantly extended. Thus increasing the image appearance, especially when high contrast objects are in close proximity to low contrast objects. HiDynamics is of significant relevance in low kV scans, e.g. for enhancing the 80 kV dataset of Dual Energy scans or pediatric imaging at 70 kV.
Ultra Fast Ceramic Detector (UFC)	Siemens proprietary scintillator material with ultra-short decay, extremely low afterglow and high absorption for optimized image quality and high dose efficiency
Detector Scatter Collimator	For improved low-contrast resolution, e.g in neuro and abdominal imaging
Max. number of slices/rotation	128 (acquired slices); 384 (reconstructed slices)
Number of detector rows	64
Number of detector electronic channels	128
Number of detector elements	47,104
Total channels per slice	1,472
Number of projections	up to 4,608/360°
Sequence acquisition modes	128 x 0.6 mm, 64 x 0.6 mm, 16 x 0.6 mm (UHR), 2 x 1 mm, 6 x 1.2 mm, 32 x 1.2 mm, 12 x 1.2 mm, 1 x 5 mm, 1 x 10 mm
Spiral acquisition modes	16 x 0.3 mm (z-UHR), 128 x 0.6 mm, 20 x 0.6 mm, 64 x 0.6 mm, 16 x 0.6 mm (UHR), 32 x 1.2 mm, 40 x 0.6 mm
High-Pitch mode z-coverage/rotation	6.53 cm/2.57" (at pitch 1.7) equals 22.9 cm/s
Adaptive Signal Boost	The Adaptive Signal Boost amplifies low signal areas of the CT data and further reduces streaks and noise in the image especially for larger patients
Adaptive 4D Spiral mode*	Spiral scan mode for a larger perfusion and dynamic CTA acquisitionis range than the detector width of up to 48 cm/18.89". Enables for 4D CT DSA.
z-UHR (Ultra High Resolution)*	Siemens' proprietary z-UHR enables previously unachievable image detail with an isotropic resolution of 30 lp/cm (0.17 mm) at 0% MTF (± 10%). The combination of z-Sharp Technology and z-UHR offers an isotropic detail in the range of flat panel or Micro CT technology.

* Optional

Appendix B

The Importance of Coherence Length

For this explanation, it is sufficient to know that in the generic scenario of Figure B.1, a very simple representation of the raw interference signal detected along an illuminated line in the sample is given by (simplified from [35]):

$$i_{det}(k) = \rho\left(P_r + P_s\int r(z)^2 dz + 2\sqrt{P_r P_s}\int r(z)\Gamma(z)\cos\left(kz\right)\right)dz \tag{B.1}$$

Where $k = {}^{2\pi}/_{\lambda}$ is the wavenumber, λ is the wavelength, ρ is the detector responsivity, q is the charge of an electron, P_r is the optical power in the reference arm, P_s is the optical power illuminating the sample, and z is the optical path length difference between the reference and sample beams. The information we wish to obtain is $r(z)$, the reflection coefficient profile of the sample along the sample beam. $\Gamma(z)$, the laser's coherence function, is a unitless function of z, decreasing in value from 1 towards 0 as $|z|$ increases, and has a physical width inversely proportional to the instantaneous linewidth of the source. Physically, it reflects how the visibility of fringes in the measured interference pattern decrease with increasing relative delay due to the source's limited temporal coherence. This length is called the "coherence length" of the laser, or perhaps more accurately the "instantaneous coherence length", and is commonly expressed by [36]:

$$z_c = 0.44\frac{\lambda_0^2}{\delta\lambda} \tag{B.2}$$

where λ_0 is the center wavelength of the instantaneous wavelength, and $\delta\lambda$ is the instantaneous linewidth around λ_c. The important step in SS-OCT is that the interference signal is measured as k is swept in time across bandwidth Δk (or equivalently, the wavelength λ is swept across bandwidth $\Delta\lambda$). In SS-OCT, the light source's wavelength is swept over a broad bandwidth $\Delta\lambda$, but at any given moment

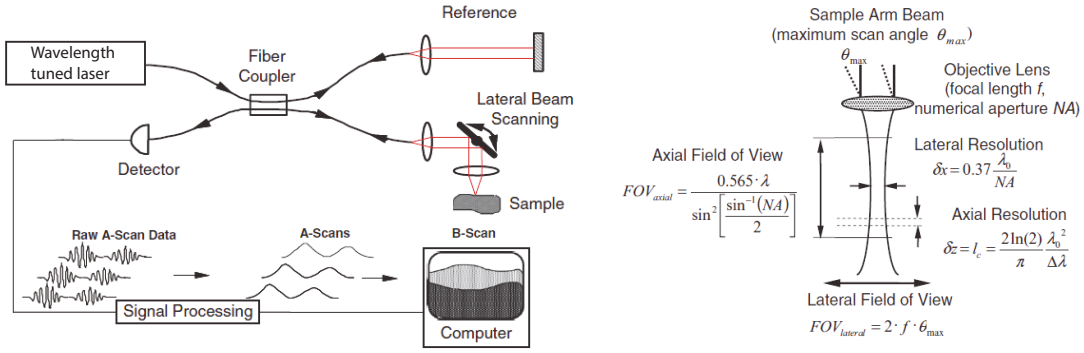

Figure B.1: Left, A generic SS-OCT setup, including a tunable wavelength laser, fiber coupler, or splitter for splitting and interfering the reference and sample beams, a lateral beam scanning mechanism, and detection and processing electronics. Right, Confocal gating in OCT due to the sample arm optics (taken from [6] with permission).

within each sweep, it has an instantaneously narrow line-width $\delta\lambda$. The first two terms in Equation B.1 represent the total power arriving at the detector from the reference and sample arms, respectively, and have no k-dependence. These are commonly called "DC terms". The third term contains the interference between the two light fields, typically called the cross-correlation terms, and is what is used to infer the structure of the sample. Note that in Equation B.1, the auto-correlation terms have been neglected [6]. Those terms reflect the self-interference between the continuum of reflections arriving at the detector from different depths within the sample. Using Euler's formula, assuming $r(z)$ is purely real-valued (which helps to simplify the math for this explanation), and since $\Gamma(z)$ is always purely real, the interference term can be re-written:

$$\begin{aligned} i_{sig}(k) &= 2\rho\sqrt{P_r P_s}\int r(z)\Gamma(z)\cos\left(kz\right)\right) dz \\ &= 2\rho\sqrt{P_r P_s}\int r(z)\Gamma(z) Re\left\{e^{jkz}\right\} dz \\ &= 2\rho\sqrt{P_r P_s} Re\left\{\int r(z)\Gamma(z)e^{jkz}dz\right\} \\ &= 4\pi\rho\sqrt{P_r P_s} Re\left\{\mathcal{F}^{-1}\left\{r(z)\Gamma(z)\right\}\right\} \end{aligned} \tag{B.3}$$

from which one can recognize that the interference signal one measures as a function of wavenumber is proportional to the real part of the inverse Fourier Transform of the product of $r(z)$ (the information we want) and $\Gamma(z)$ (a characteristic of the light source). Taking the Fourier Transform of the measured signal gives an estimate of the product $r(z)\Gamma(z)$, which are unfortunately inseparable. For $z > z_c$, $\Gamma(z)$ decreases and the measurement of $r(z)$ is increasingly attenuated until it is below the system noise level, rendering it undetectable. The masking of $r(z)$ by $\Gamma(z)$ is commonly referred to as "sensitivity falloff". In other words, since fringes cannot be detected at optical delays larger than the instantaneous coherence length, the axial extent of the image in SS-OCT is fundamentally limited to this size. This is in stark contrast to TD-OCT wherein the "coherence length" determines the axial resolution of the system. The terms "coherence length" and "instantaneous coherence length" have distinctly different importance in the two contexts that can only be appreciated with an understanding of the modes of operation of different light sources.

Appendix C

Permissions of Reproduction

This appendix contains written permissions for reproduction of the content published in the three journal articles on which Chapters 2-4 are based. Additionally, permissions for the reproduction of borrowed content in Figures 1.1, 1.2, 1.4, 3.5, 5.13, and B.1 are provided.

January 2, 2020

Director of Publications
SPIE
P.O. Box 10
Bellingham, WA
98227-0010 USA

I am preparing my PhD thesis for submission to the Faculty of Graduate Studies at Dalhousie University, Halifax, Nova Scotia, Canada. I am seeking your permission to include a manuscript version of the following paper(s) as a chapter in the thesis:

- MacDougall, D., Rainsbury, J., Brown, J., Bance, M. & Adamson, R. Optical coherence tomography system requirements for clinical diagnostic middle ear imaging. J. Biomed. Opt 20, 056008 (2015).

Canadian graduate theses are reproduced by the Library and Archives of Canada (formerly National Library of Canada) through a non-exclusive, world-wide license to reproduce, loan, distribute, or sell theses. I am also seeking your permission for the material described above to be reproduced and distributed by the LAC(NLC). Further details about the LAC(NLC) thesis program are available on the LAC(NLC) website (www.nlc-bnc.ca).

Full publication details and a copy of this permission letter will be included in the thesis.

Yours sincerely,

Dan MacDougall

Permission is granted for:

a) the inclusion of the material described above in your thesis.

b) for the material described above to be included in the copy of your thesis that is sent to the Library and Archives of Canada (formerly National Library of Canada) for reproduction and distribution.

SPIE.

Thank you for seeking permission from SPIE to reprint material from our publications. The article you have requested to reprint from is published under Creative Commons (CC BY 4.0)—Gold Open Access. For articles published under CC BY 4.0, users are free to share (copy, distribute, and transmit), to remix (adapt), and to make commercial use of the Article under the following conditions:
Attribution: Users must attribute the contribution in the manner specified by the author or licensor (but not in any way that suggests that they or their use of the Article is endorsed by the Author or licensor).
See citation formatting below.
Notice: For any reuse or distribution, users must make clear to others the license terms of this work, preferably using a link to the Creative Commons webpage.

[redacted]
Director of Publications & Platform Date 10 Jan 2020

Patrick Franzen
Director ofPublications & Platform
SPIE
PO Box 10, Bellingham, WA98227-0010
USA 360/676-3290**(Pacific Time)**
patrickf@spie.org

January 22, 2020

Rebecca Robinson
Authorized Agent
OSA

I am preparing my PhD thesis for submission to the Faculty of Graduate Studies at Dalhousie University, Halifax, Nova Scotia, Canada. I am seeking your permission to include a manuscript version of the following paper(s) as a chapter in the thesis:

- MacDougall, D., Farrell, J., Brown, J., Bance, M. & Adamson, R. Long-range, wide-field swept-source optical coherence tomography with GPU accelerated digital lock-in Doppler vibrography for real-time, in vivo middle ear diagnostics. *Biomed Opt Express* **7**, 4621–4635 (2016).

Canadian graduate theses are reproduced by the Library and Archives of Canada (formerly National Library of Canada) through a non-exclusive, world-wide license to reproduce, loan, distribute, or sell theses. I am also seeking your permission for the material described above to be reproduced and distributed by the LAC(NLC). Further details about the LAC(NLC) thesis program are available on the LAC(NLC) website (www.nlc-bnc.ca).

Full publication details and a copy of this permission letter will be included in the thesis.

Yours sincerely,

Dan MacDougall

Permission is granted for:

a) the inclusion of the material described above in your thesis.

b) for the material described above to be included in the copy of your thesis that is sent to the Library and Archives of Canada (formerly National Library of Canada) for reproduction and distribution.

Name: Rebecca Robinson Title: Authorized Agent, The Optical Society

Signature: [redacted] Date: 22 January 2020

January 30, 2020

Copyright Clearance Center
222 Rosewood Drive
Danvers, MA 01923

I am preparing my PhD thesis for submission to the Faculty of Graduate Studies at Dalhousie University, Halifax, Nova Scotia, Canada. I am seeking your permission to include the final peer-reviewed manuscript version of the following paper(s) as a chapter in the thesis:

- MacDougall, D. et al. Optical Coherence Tomography Doppler Vibrometry Measurement of Stapes Vibration in Patients with Stapes Fixation and Normal Controls: Otology & Neurotology 40, e349–e355 (2019).

Canadian graduate theses are collected and stored online by the Library and Archives of Canada. I am also seeking your permission for the material described above to be stored online with the LAC. Further details about the LAC thesis program are available on the LAC website (www.bac-lac.gc.ca).

Full publication details and a copy of this permission letter will be included in the thesis. In accordance with the copyright transfer agreement signed at the time of submission, the final peer-reviewed manuscript will be under embargo and not published by Dalhousie or stored online by the Library and Archives of Canada until April 2020.

Additional terms by Wolters Kluwer Health: You must attach the following notice to the final peer-reviewed manuscript: "This is a non-final version of an article published in final form in [provide complete journal citation]." You shall provide a link in the final peer-reviewed manuscript to the *Otology & Neurotology* website.

Yours sincerely,

Dan MacDougall

Permission is granted for:

a) the inclusion of the material described above in your thesis.

b) for the material described above to be included in the copy of your thesis that is sent to the Library and Archives of Canada (formerly National Library of Canada) for online storage.

Name:	Thomas Ramsden	Title:	Director of Licensing, Rights, and Permissions Operations
Signature:	[redacted]	Date:	Jan 30, 2020

Copyright Clearance Center Marketplace™

Cengage Learning - License Terms and Conditions

Order Date	01-Feb-2020
Order license ID	1016138-2
ISBN-13	9781565933460
Type of Use	Republish in a thesis/dissertation
Publisher	THOMSON DELMAR LEARNING
Portion	Chart/graph/table/figure

LICENSED CONTENT

Publication Title	Clinical audiology : an introduction	Country	United States of America
		Rightsholder	Cengage Learning
Author/Editor	STACH, BRAD A.	Publication Type	Book
Date	01/01/1998		
Language	English		

REQUEST DETAILS

Portion Type	Chart/graph/table/figure	Distribution	Worldwide
Number of charts / graphs / tables / figures requested	2	Translation	Original language of publication
		Copies for the disabled?	No
Format (select all that apply)	Electronic	Minor editing privileges?	Yes
Who will republish the content?	Academic institution	Incidental promotional use?	No
Duration of Use	Life of current edition	Currency	CAD
Lifetime Unit Quantity	Up to 499		
Rights Requested	Main product		

NEW WORK DETAILS

Title	OPTICAL COHERENCE TOMOGRAPHY FOR CLINICAL OTOLOGY	Institution name	Dalhousie University
		Expected presentation date	2020-04-01
Instructor name	Dan MacDougall		

ADDITIONAL DETAILS

Order reference number	N/A	The requesting person / organization to appear on the license	Dan MacDougall, PhD Student at Dalhousie University

REUSE CONTENT DETAILS

Title, description or numeric reference of the portion(s)	Figure 2-14 and 2-16	**Title of the article/chapter the portion is from**	Ch. 2 - The Nature of Hearing
Editor of portion(s)	N/A	**Author of portion(s)**	STACH, BRAD A.
Volume of serial or monograph	N/A	**Issue, if republishing an article from a serial**	Ed. 2
Page or page range of portion	Pg. 57 and 60	**Publication date of portion**	2010-01-01

PUBLISHER TERMS AND CONDITIONS

Amounts of material. No more than 10% of a single Cengage product may be re-used in your upcoming product. Total Cengage Learning content must equal 10% or less of your upcoming product. If using more than what is permitted by Cengage Learning your permission will automatically be null and void.

CCC Republication Terms and Conditions

1. Description of Service; Defined Terms. This Republication License enables the User to obtain licenses for republication of one or more copyrighted works as described in detail on the relevant Order Confirmation (the "Work(s)"). Copyright Clearance Center, Inc. ("CCC") grants licenses through the Service on behalf of the rightsholder identified on the Order Confirmation (the "Rightsholder"). "Republication", as used herein, generally means the inclusion of a Work, in whole or in part, in a new work or works, also as described on the Order Confirmation. "User", as used herein, means the person or entity making such republication.

2. The terms set forth in the relevant Order Confirmation, and any terms set by the Rightsholder with respect to a particular Work, govern the terms of use of Works in connection with the Service. By using the Service, the person transacting for a republication license on behalf of the User represents and warrants that he/she/it (a) has been duly authorized by the User to accept, and hereby does accept, all such terms and conditions on behalf of User, and (b) shall inform User of all such terms and conditions. In the event such person is a "freelancer" or other third party independent of User and CCC, such party shall be deemed jointly a "User" for purposes of these terms and conditions. In any event, User shall be deemed to have accepted and agreed to all such terms and conditions if User republishes the Work in any fashion.

3. Scope of License; Limitations and Obligations.

    3.1. All Works and all rights therein, including copyright rights, remain the sole and exclusive property of the Rightsholder. The license created by the exchange of an Order Confirmation (and/or any invoice) and payment by User of the full amount set forth on that document includes only those rights expressly set forth in the Order Confirmation and in these terms and conditions, and conveys no other rights in the Work(s) to User. All rights not expressly granted are hereby reserved.

    3.2. General Payment Terms: You may pay by credit card or through an account with us payable at the end of the month. If you and we agree that you may establish a standing account with CCC, then the following terms apply: Remit Payment to: Copyright Clearance Center, 29118 Network Place, Chicago, IL 60673-1291. Payments Due: Invoices are payable upon their delivery to you (or upon our notice to you that they are available to you for downloading). After 30 days, outstanding amounts will be subject to a service charge of 1-1/2% per month or, if less, the maximum rate allowed by applicable law. Unless otherwise specifically set forth in the Order Confirmation or in a separate written agreement signed by CCC, invoices are due and payable on "net 30" terms. While User may exercise the rights licensed immediately upon issuance of the Order Confirmation, the license is automatically revoked and is null and void, as if it had never been issued, if complete payment for the license is not received on a timely basis either from User directly or through a payment agent, such as a credit card company.

    3.3. Unless otherwise provided in the Order Confirmation, any grant of rights to User (i) is "one-time" (including the editions and product family specified in the license), (ii) is non-exclusive and non-transferable and (iii) is subject to any and all limitations and restrictions (such as, but not limited to, limitations on duration of use

or circulation) included in the Order Confirmation or invoice and/or in these terms and conditions. Upon completion of the licensed use, User shall either secure a new permission for further use of the Work(s) or immediately cease any new use of the Work(s) and shall render inaccessible (such as by deleting or by removing or severing links or other locators) any further copies of the Work (except for copies printed on paper in accordance with this license and still in User's stock at the end of such period).

3.4. In the event that the material for which a republication license is sought includes third party materials (such as photographs, illustrations, graphs, inserts and similar materials) which are identified in such material as having been used by permission, User is responsible for identifying, and seeking separate licenses (under this Service or otherwise) for, any of such third party materials; without a separate license, such third party materials may not be used.

3.5. Use of proper copyright notice for a Work is required as a condition of any license granted under the Service. Unless otherwise provided in the Order Confirmation, a proper copyright notice will read substantially as follows: "Republished with permission of [Rightsholder's name], from [Work's title, author, volume, edition number and year of copyright]; permission conveyed through Copyright Clearance Center, Inc. " Such notice must be provided in a reasonably legible font size and must be placed either immediately adjacent to the Work as used (for example, as part of a by-line or footnote but not as a separate electronic link) or in the place where substantially all other credits or notices for the new work containing the republished Work are located. Failure to include the required notice results in loss to the Rightsholder and CCC, and the User shall be liable to pay liquidated damages for each such failure equal to twice the use fee specified in the Order Confirmation, in addition to the use fee itself and any other fees and charges specified.

3.6. User may only make alterations to the Work if and as expressly set forth in the Order Confirmation. No Work may be used in any way that is defamatory, violates the rights of third parties (including such third parties' rights of copyright, privacy, publicity, or other tangible or intangible property), or is otherwise illegal, sexually explicit or obscene. In addition, User may not conjoin a Work with any other material that may result in damage to the reputation of the Rightsholder. User agrees to inform CCC if it becomes aware of any infringement of any rights in a Work and to cooperate with any reasonable request of CCC or the Rightsholder in connection therewith.

4. Indemnity. User hereby indemnifies and agrees to defend the Rightsholder and CCC, and their respective employees and directors, against all claims, liability, damages, costs and expenses, including legal fees and expenses, arising out of any use of a Work beyond the scope of the rights granted herein, or any use of a Work which has been altered in any unauthorized way by User, including claims of defamation or infringement of rights of copyright, publicity, privacy or other tangible or intangible property.

5. Limitation of Liability. UNDER NO CIRCUMSTANCES WILL CCC OR THE RIGHTSHOLDER BE LIABLE FOR ANY DIRECT, INDIRECT, CONSEQUENTIAL OR INCIDENTAL DAMAGES (INCLUDING WITHOUT LIMITATION DAMAGES FOR LOSS OF BUSINESS PROFITS OR INFORMATION, OR FOR BUSINESS INTERRUPTION) ARISING OUT OF THE USE OR INABILITY TO USE A WORK, EVEN IF ONE OF THEM HAS BEEN ADVISED OF THE POSSIBILITY OF SUCH DAMAGES. In any event, the total liability of the Rightsholder and CCC (including their respective employees and directors) shall not exceed the total amount actually paid by User for this license. User assumes full liability for the actions and omissions of its principals, employees, agents, affiliates, successors and assigns.

6. Limited Warranties. THE WORK(S) AND RIGHT(S) ARE PROVIDED "AS IS". CCC HAS THE RIGHT TO GRANT TO USER THE RIGHTS GRANTED IN THE ORDER CONFIRMATION DOCUMENT. CCC AND THE RIGHTSHOLDER DISCLAIM ALL OTHER WARRANTIES RELATING TO THE WORK(S) AND RIGHT(S), EITHER EXPRESS OR IMPLIED, INCLUDING WITHOUT LIMITATION IMPLIED WARRANTIES OF MERCHANTABILITY OR FITNESS FOR A PARTICULAR PURPOSE. ADDITIONAL RIGHTS MAY BE REQUIRED TO USE ILLUSTRATIONS, GRAPHS, PHOTOGRAPHS, ABSTRACTS, INSERTS OR OTHER PORTIONS OF THE WORK (AS OPPOSED TO THE ENTIRE WORK) IN A MANNER CONTEMPLATED BY USER; USER UNDERSTANDS AND AGREES THAT NEITHER CCC NOR THE RIGHTSHOLDER MAY HAVE SUCH ADDITIONAL RIGHTS TO GRANT.

7. Effect of Breach. Any failure by User to pay any amount when due, or any use by User of a Work beyond the scope

of the license set forth in the Order Confirmation and/or these terms and conditions, shall be a material breach of the license created by the Order Confirmation and these terms and conditions. Any breach not cured within 30 days of written notice thereof shall result in immediate termination of such license without further notice. Any unauthorized (but licensable) use of a Work that is terminated immediately upon notice thereof may be liquidated by payment of the Rightsholder's ordinary license price therefor; any unauthorized (and unlicensable) use that is not terminated immediately for any reason (including, for example, because materials containing the Work cannot reasonably be recalled) will be subject to all remedies available at law or in equity, but in no event to a payment of less than three times the Rightsholder's ordinary license price for the most closely analogous licensable use plus Rightsholder's and/or CCC's costs and expenses incurred in collecting such payment.

8. Miscellaneous.

8.1. User acknowledges that CCC may, from time to time, make changes or additions to the Service or to these terms and conditions, and CCC reserves the right to send notice to the User by electronic mail or otherwise for the purposes of notifying User of such changes or additions; provided that any such changes or additions shall not apply to permissions already secured and paid for.

8.2. Use of User-related information collected through the Service is governed by CCC's privacy policy, available online here: https://marketplace.copyright.com/rs-ui-web/mp/privacy-policy

8.3. The licensing transaction described in the Order Confirmation is personal to User. Therefore, User may not assign or transfer to any other person (whether a natural person or an organization of any kind) the license created by the Order Confirmation and these terms and conditions or any rights granted hereunder; provided, however, that User may assign such license in its entirety on written notice to CCC in the event of a transfer of all or substantially all of User's rights in the new material which includes the Work(s) licensed under this Service.

8.4. No amendment or waiver of any terms is binding unless set forth in writing and signed by the parties. The Rightsholder and CCC hereby object to any terms contained in any writing prepared by the User or its principals, employees, agents or affiliates and purporting to govern or otherwise relate to the licensing transaction described in the Order Confirmation, which terms are in any way inconsistent with any terms set forth in the Order Confirmation and/or in these terms and conditions or CCC's standard operating procedures, whether such writing is prepared prior to, simultaneously with or subsequent to the Order Confirmation, and whether such writing appears on a copy of the Order Confirmation or in a separate instrument.

8.5. The licensing transaction described in the Order Confirmation document shall be governed by and construed under the law of the State of New York, USA, without regard to the principles thereof of conflicts of law. Any case, controversy, suit, action, or proceeding arising out of, in connection with, or related to such licensing transaction shall be brought, at CCC's sole discretion, in any federal or state court located in the County of New York, State of New York, USA, or in any federal or state court whose geographical jurisdiction covers the location of the Rightsholder set forth in the Order Confirmation. The parties expressly submit to the personal jurisdiction and venue of each such federal or state court.If you have any comments or questions about the Service or Copyright Clearance Center, please contact us at 978-750-8400 or send an e-mail to support@copyright.com.

v 1.1

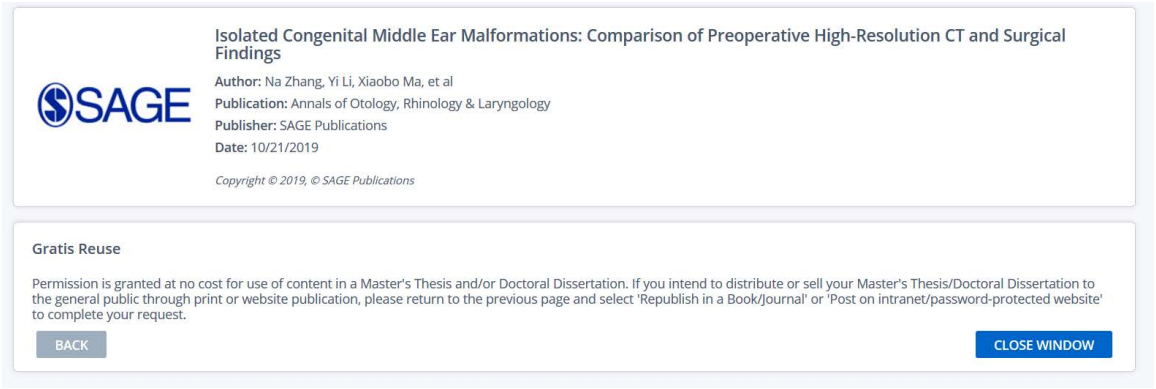
Isolated Congenital Middle Ear Malformations: Comparison of Preoperative High-Resolution CT and Surgical Findings
Author: Na Zhang, Yi Li, Xiaobo Ma, et al
Publication: Annals of Otology, Rhinology & Laryngology
Publisher: SAGE Publications
Date: 10/21/2019
Copyright © 2019, © SAGE Publications
Gratis Reuse
Permission is granted at no cost for use of content in a Master's Thesis and/or Doctoral Dissertation. If you intend to distribute or sell your Master's Thesis/Doctoral Dissertation to the general public through print or website publication, please return to the previous page and select 'Republish in a Book/Journal' or 'Post on intranet/password-protected website' to complete your request.
BACK
CLOSE WINDOW

WOLTERS KLUWER HEALTH, INC. ORDER DETAILS

Feb 04, 2020

This Agreement between Dan MacDougall ("You") and Wolters Kluwer Health, Inc. ("Wolters Kluwer Health, Inc.") consists of your order details and the terms and conditions provided by Wolters Kluwer Health, Inc. and Copyright Clearance Center.

Order Number	501543735
Order date	Feb 01, 2020
Licensed Content Publisher	Wolters Kluwer Health, Inc.
Licensed Content Publication	Ear and Hearing
Licensed Content Title	Clinical Utility of Laser-Doppler Vibrometer Measurements in Live Normal and Pathologic Human Ears
Licensed Content Author	John Rosowski, Hideko Nakajima, and Saumil Merchant
Licensed Content Date	Jan 1, 2008
Licensed Content Volume	29
Licensed Content Issue	1
Type of use	Dissertation/Thesis
Requestor type	University/College
Sponsorship	No Sponsorship
Format	Electronic
Will this be posted on a password protected website?	No
Portion	Figures/tables/illustrations
Number of figures/tables /illustrations	2
Author of this Wolters Kluwer article	No
Will you be translating?	No
Intend to modify/adapt the content	No
Title	OPTICAL COHERENCE TOMOGRAPHY FOR CLINICAL OTOLOGY
Institution name	Dalhousie University
Expected presentation date	Feb 2020
Order reference number	none
Portions	Figure 1 and 2
Requestor Location	Dalhousie University Centre for Clinical Research Rm 247 5790 University Ave Halifax, B3H1V7 Canada Attn: Dan MacDougall
Billing Type	Invoice

Billing Address	Dalhousie University OCLC Headquarters, 6565 Kilgour Place Dublin, OH 43017 United States Attn: Jackie Fahmy
Total	**0.00 CAD**

Terms and Conditions

Wolters Kluwer Health Inc. Terms and Conditions

1. **Duration of License:** Permission is granted for a one time use only. Rights herein do not apply to future reproductions, editions, revisions, or other derivative works. This permission shall be effective as of the date of execution by the parties for the maximum period of 12 months and should be renewed after the term expires.
    i. When content is to be republished in a book or journal the validity of this agreement should be the life of the book edition or journal issue.
    ii. When content is licensed for use on a website, internet, intranet, or any publicly accessible site (not including a journal or book), you agree to remove the material from such site after 12 months, or request to renew your permission license
2. **Credit Line:** A credit line must be prominently placed and include: For book content: the author(s), title of book, edition, copyright holder, year of publication; For journal content: the author(s), titles of article, title of journal, volume number, issue number, inclusive pages and website URL to the journal page; If a journal is published by a learned society the credit line must include the details of that society.
3. **Warranties:** The requestor warrants that the material shall not be used in any manner which may be considered derogatory to the title, content, authors of the material, or to Wolters Kluwer Health, Inc.
4. **Indemnity:** You hereby indemnify and hold harmless Wolters Kluwer Health, Inc. and its respective officers, directors, employees and agents, from and against any and all claims, costs, proceeding or demands arising out of your unauthorized use of the Licensed Material
5. **Geographical Scope:** Permission granted is non-exclusive and is valid throughout the world in the English language and the languages specified in the license.
6. **Copy of Content:** Wolters Kluwer Health, Inc. cannot supply the requestor with the original artwork, high-resolution images, electronic files or a clean copy of content.
7. **Validity:** Permission is valid if the borrowed material is original to a Wolters Kluwer Health, Inc. imprint (J.B Lippincott, Lippincott-Raven Publishers, Williams & Wilkins, Lea & Febiger, Harwal, Rapid Science, Little Brown & Company, Harper & Row Medical, American Journal of Nursing Co, and Urban & Schwarzenberg - English Language, Raven Press, Paul Hoeber, Springhouse, Ovid), and the Anatomical Chart Company
8. **Third Party Material:** This permission does not apply to content that is credited to publications other than Wolters Kluwer Health, Inc. or its Societies. For images credited to non-Wolters Kluwer Health, Inc. books or journals, you must obtain permission from the source referenced in the figure or table legend or credit line before making any use of the image(s), table(s) or other content.
9. **Adaptations:** Adaptations are protected by copyright. For images that have been adapted, permission must be sought from the rightsholder of the original material and the rightsholder of the adapted material.
10. **Modifications:** Wolters Kluwer Health, Inc. material is not permitted to be modified or adapted without written approval from Wolters Kluwer Health, Inc. with the exception of text size or color. The adaptation should be credited as follows: Adapted with permission from Wolters Kluwer Health, Inc.: [the author(s), title of book, edition, copyright holder, year of publication] or [the author(s), titles of article, title of journal, volume number, issue number, inclusive pages and website URL to the journal page].
11. **Full Text Articles:** Republication of full articles in English is prohibited.
12. **Branding and Marketing:** No drug name, trade name, drug logo, or trade logo can be included on the same page as material borrowed from *Diseases of the Colon & Rectum, Plastic Reconstructive Surgery, Obstetrics & Gynecology (The Green Journal), Critical Care Medicine, Pediatric Critical Care Medicine, the American Heart Association publications and the American Academy of Neurology publications.*
13. **Open Access:** Unless you are publishing content under the same Creative Commons license, the following statement must be added when reprinting material in Open Access journals: "The Creative Commons license does not apply to this content. Use of the material in any format is prohibited without written permission from the publisher, Wolters Kluwer Health, Inc. Please contact permissions@lww.com for further information."
14. **Translations:** The following disclaimer must appear on all translated copies: Wolters Kluwer Health, Inc. and its Societies take no responsibility for the accuracy of the translation from the published English original and are not liable for any

errors which may occur.

15. **Published Ahead of Print (PAP):** Articles in the PAP stage of publication can be cited using the online publication date and the unique DOI number.
    i. Disclaimer: Articles appearing in the PAP section have been peer-reviewed and accepted for publication in the relevant journal and posted online before print publication. Articles appearing as PAP may contain statements, opinions, and information that have errors in facts, figures, or interpretation. Any final changes in manuscripts will be made at the time of print publication and will be reflected in the final electronic version of the issue. Accordingly, Wolters Kluwer Health, Inc., the editors, authors and their respective employees are not responsible or liable for the use of any such inaccurate or misleading data, opinion or information contained in the articles in this section.
16. **Termination of Contract:** Wolters Kluwer Health, Inc. must be notified within 90 days of the original license date if you opt not to use the requested material.
17. **Waived Permission Fee:** Permission fees that have been waived are not subject to future waivers, including similar requests or renewing a license.
18. **Contingent on payment:** You may exercise these rights licensed immediately upon issuance of the license, however until full payment is received either by the publisher or our authorized vendor, this license is not valid. If full payment is not received on a timely basis, then any license preliminarily granted shall be deemed automatically revoked and shall be void as if never granted. Further, in the event that you breach any of these terms and conditions or any of Wolters Kluwer Health, Inc.'s other billing and payment terms and conditions, the license is automatically revoked and shall be void as if never granted. Use of materials as described in a revoked license, as well as any use of the materials beyond the scope of an unrevoked license, may constitute copyright infringement and publisher reserves the right to take any and all action to protect its copyright in the materials.
19. **STM Signatories Only:** Any permission granted for a particular edition will apply to subsequent editions and for editions in other languages, provided such editions are for the work as a whole in situ and do not involve the separate exploitation of the permitted illustrations or excerpts. Please view: STM Permissions Guidelines
20. **Warranties and Obligations:** LICENSOR further represents and warrants that, to the best of its knowledge and belief, LICENSEE's contemplated use of the Content as represented to LICENSOR does not infringe any valid rights to any third party.
21. **Breach:** If LICENSEE fails to comply with any provisions of this agreement, LICENSOR may serve written notice of breach of LICENSEE and, unless such breach is fully cured within fifteen (15) days from the receipt of notice by LICENSEE, LICENSOR may thereupon, at its option, serve notice of cancellation on LICENSEE, whereupon this Agreement shall immediately terminate.
22. **Assignment:** License conveyed hereunder by the LICENSOR shall not be assigned or granted in any manner conveyed to any third party by the LICENSEE without the consent in writing to the LICENSOR.
23. **Governing Law:** The laws of The State of New York shall govern interpretation of this Agreement and all rights and liabilities arising hereunder.
24. **Unlawful:** If any provision of this Agreement shall be found unlawful or otherwise legally unenforceable, all other conditions and provisions of this Agreement shall remain in full force and effect.

For Copyright Clearance Center / RightsLink Only:

1. **Service Description for Content Services:** Subject to these terms of use, any terms set forth on the particular order, and payment of the applicable fee, you may make the following uses of the ordered materials:
    i. **Content Rental:** You may access and view a single electronic copy of the materials ordered for the time period designated at the time the order is placed. Access to the materials will be provided through a dedicated content viewer or other portal, and access will be discontinued upon expiration of the designated time period. An order for Content Rental does not include any rights to print, download, save, create additional copies, to distribute or to reuse in any way the full text or parts of the materials.
    ii. **Content Purchase:** You may access and download a single electronic copy of the materials ordered. Copies will be provided by email or by such other means as publisher may make available from time to time. An order for Content Purchase does not include any rights to create additional copies or to distribute copies of the materials

Other Terms and Conditions:
v1.18

AW: Permissions Request

P **Permission@thieme.de <permission@thieme.de>**
1/31/2020 5:10 AM

To: dan.macdougall@dal.ca

Dear Dan,

thank you for your request which has been forwarded to me.

Please note that in the case of this book, the copyright of the illustrations is being held by the illustrator. So please turn to Anne Johnson directly to obtain permission.

As far as I can see on the internet, you should be able to reach her via Facebook or Linkedin: Anne Johnson de Weissenbruch, WAG Design & Communications, Lasne, Belgium.

I'm sorry I cannot be of further help to you here.

Kind regards
Barbara Elias

This email is without prejudice and subject to contract

Barbara Elias
Permissions Associate

Thieme International Business
Georg Thieme Verlag KG
A Thieme Group Company
Ruedigerstrasse 14, 70469 Stuttgart, Germany

Tel. +49 [0]711 8931 681
Fax +49 [0]711 8931 143
www.thieme.de, www.thieme.com
Permissions@thieme.de

Dear Publisher,

I hear by give my written consent to Mr. Dan MacDougall to use two illustrations created for, 'Atlas of Middle Ear Surgery' (Michel Gersdorff and Jean-Marc Gerard, 2010, ref. Figures 4.82 and 5.36) to support his Thesis work.

I authorize one-time usage of these figures to be used strictly for the document entitled, “OPTICAL COHERENCE TOMOGRAPHY FOR CLINICAL OTOLOGY”, A PhD Thesis at Dalhousie University in Halifax, Nova Scotia, Canada.

The author will correctly reference the source of the images (Title, Authors and Illustrator) in his work.

The illustrations may be reproduced in digital format only and are to be used for EDUCATIONAL PURPOSES ONLY.

Upon publication, a digital copy of the work shall be provided to Anne Johnson as proof of usage.

The illustrations MAY NOT BE USED FOR RESALE and may NOT BE REPRODUCED in any other format or by a third party without the written consent of the Illustrator.

Respectfully,

[redacted]

Anne Johnson,

SPRINGER NATURE LICENSE
TERMS AND CONDITIONS

Jan 30, 2020

This Agreement between Dalhousie University -- Dan MacDougall ("You") and Springer Nature ("Springer Nature") consists of your license details and the terms and conditions provided by Springer Nature and Copyright Clearance Center.

License Number	4758871188082
License date	Jan 30, 2020
Licensed Content Publisher	Springer Nature
Licensed Content Publication	Springer eBook
Licensed Content Title	Theory of Optical Coherence Tomography
Licensed Content Author	J. A. Izatt, M. A. Choma
Licensed Content Date	Jan 1, 2008
Type of Use	Thesis/Dissertation
Requestor type	academic/university or research institute
Format	electronic
Portion	figures/tables/illustrations
Number of figures/tables	2

/illustrations	
Will you be translating?	no
Circulation/distribution	1 - 29
Author of this Springer Nature content	no
Title	OPTICAL COHERENCE TOMOGRAPHY FOR CLINICAL OTOLOGY
Institution name	Dalhousie University
Expected presentation date	Feb 2020
Order reference number	None
Portions	Figure 2.1 and 2.2 are used in an appendix to explain how swept-source OCT works. My thesis work uses the technique of swept-source OCT and the appendix is used to provide the reader with a basic understanding of how it work.
Requestor Location	Dalhousie University OCLC Headquarters, 6565 Kilgour Place Dublin, OH 43017 United States Attn: Dalhousie University
Total	0.00 CAD

Terms and Conditions

Springer Nature Customer Service Centre GmbH
Terms and Conditions

This agreement sets out the terms and conditions of the licence (the **Licence**) between you and **Springer Nature Customer Service Centre GmbH** (the **Licensor**). By clicking

'accept' and completing the transaction for the material (**Licensed Material**), you also confirm your acceptance of these terms and conditions.

1. Grant of License

1. 1. The Licensor grants you a personal, non-exclusive, non-transferable, world-wide licence to reproduce the Licensed Material for the purpose specified in your order only. Licences are granted for the specific use requested in the order and for no other use, subject to the conditions below.

1. 2. The Licensor warrants that it has, to the best of its knowledge, the rights to license reuse of the Licensed Material. However, you should ensure that the material you are requesting is original to the Licensor and does not carry the copyright of another entity (as credited in the published version).

1. 3. If the credit line on any part of the material you have requested indicates that it was reprinted or adapted with permission from another source, then you should also seek permission from that source to reuse the material.

2. Scope of Licence

2. 1. You may only use the Licensed Content in the manner and to the extent permitted by these Ts&Cs and any applicable laws.

2. 2. A separate licence may be required for any additional use of the Licensed Material, e.g. where a licence has been purchased for print only use, separate permission must be obtained for electronic re-use. Similarly, a licence is only valid in the language selected and does not apply for editions in other languages unless additional translation rights have been granted separately in the licence. Any content owned by third parties are expressly excluded from the licence.

2. 3. Similarly, rights for additional components such as custom editions and derivatives require additional permission and may be subject to an additional fee. Please apply to Journalpermissions@springernature.com/bookpermissions@springernature.com for these rights.

2. 4. Where permission has been granted **free of charge** for material in print, permission may also be granted for any electronic version of that work, provided that the material is incidental to your work as a whole and that the electronic version is essentially equivalent to, or substitutes for, the print version.

2. 5. An alternative scope of licence may apply to signatories of the STM Permissions Guidelines, as amended from time to time.

3. Duration of Licence

3. 1. A licence for is valid from the date of purchase ('Licence Date') at the end of the relevant period in the below table:

Scope of Licence	Duration of Licence
Post on a website	12 months
Presentations	12 months
Books and journals	Lifetime of the edition in the language purchased

4. Acknowledgement

4. 1. The Licensor's permission must be acknowledged next to the Licenced Material in print. In electronic form, this acknowledgement must be visible at the same time as the figures/tables/illustrations or abstract, and must be hyperlinked to the journal/book's homepage. Our required acknowledgement format is in the Appendix below.

5. Restrictions on use

5. 1. Use of the Licensed Material may be permitted for incidental promotional use and minor editing privileges e.g. minor adaptations of single figures, changes of format, colour and/or style where the adaptation is credited as set out in Appendix 1 below. Any other changes including but not limited to, cropping, adapting, omitting material that affect the meaning, intention or moral rights of the author are strictly prohibited.

5. 2. You must not use any Licensed Material as part of any design or trademark.

5. 3. Licensed Material may be used in Open Access Publications (OAP) before publication by Springer Nature, but any Licensed Material must be removed from OAP sites prior to final publication.

6. Ownership of Rights

6. 1. Licensed Material remains the property of either Licensor or the relevant third party and any rights not explicitly granted herein are expressly reserved.

7. Warranty

IN NO EVENT SHALL LICENSOR BE LIABLE TO YOU OR ANY OTHER PARTY OR ANY OTHER PERSON OR FOR ANY SPECIAL, CONSEQUENTIAL, INCIDENTAL OR INDIRECT DAMAGES, HOWEVER CAUSED, ARISING OUT OF OR IN CONNECTION WITH THE DOWNLOADING, VIEWING OR USE OF THE MATERIALS REGARDLESS OF THE FORM OF ACTION, WHETHER FOR BREACH OF CONTRACT, BREACH OF WARRANTY, TORT, NEGLIGENCE, INFRINGEMENT OR OTHERWISE (INCLUDING, WITHOUT LIMITATION, DAMAGES BASED ON LOSS OF PROFITS, DATA, FILES, USE, BUSINESS OPPORTUNITY OR CLAIMS OF

THIRD PARTIES), AND
WHETHER OR NOT THE PARTY HAS BEEN ADVISED OF THE POSSIBILITY OF SUCH DAMAGES. THIS LIMITATION SHALL APPLY NOTWITHSTANDING ANY FAILURE OF ESSENTIAL PURPOSE OF ANY LIMITED REMEDY PROVIDED HEREIN.

8. Limitations

8. 1. ***BOOKS ONLY:*** Where **'reuse in a dissertation/thesis'** has been selected the following terms apply: Print rights of the final author's accepted manuscript (for clarity, NOT the published version) for up to 100 copies, electronic rights for use only on a personal website or institutional repository as defined by the Sherpa guideline (www.sherpa.ac.uk/romeo/).

9. Termination and Cancellation

9. 1. Licences will expire after the period shown in Clause 3 (above).

9. 2. Licensee reserves the right to terminate the Licence in the event that payment is not received in full or if there has been a breach of this agreement by you.

Appendix 1 — Acknowledgements:

For Journal Content:
Reprinted by permission from [**the Licensor**]: [**Journal Publisher** (e.g. Nature/Springer/Palgrave)] [**JOURNAL NAME**] [**REFERENCE CITATION** (Article name, Author(s) Name), [**COPYRIGHT**] (year of publication)

For **Advance Online Publication papers:**
Reprinted by permission from [**the Licensor**]: [**Journal Publisher** (e.g. Nature/Springer/Palgrave)] [**JOURNAL NAME**] [**REFERENCE CITATION** (Article name, Author(s) Name), [**COPYRIGHT**] (year of publication), advance online publication, day month year (doi: 10.1038/sj.[JOURNAL ACRONYM].)

For Adaptations/Translations:
Adapted/Translated by permission from [**the Licensor**]: [**Journal Publisher** (e.g. Nature/Springer/Palgrave)] [**JOURNAL NAME**] [**REFERENCE CITATION** (Article name, Author(s) Name), [**COPYRIGHT**] (year of publication)

Note: For any republication from the British Journal of Cancer, the following credit line style applies:

Reprinted/adapted/translated by permission from [**the Licensor**]: on behalf of Cancer Research UK: : [**Journal Publisher** (e.g. Nature/Springer/Palgrave)] [**JOURNAL NAME**] [**REFERENCE CITATION** (Article name, Author(s) Name), [**COPYRIGHT]** (year of publication)

For **Advance Online Publication** papers:
Reprinted by permission from The [**the Licensor**]: on behalf of Cancer Research UK: [**Journal Publisher** (e.g. Nature/Springer/Palgrave)] [**JOURNAL NAME**] [**REFERENCE CITATION** (Article name, Author(s) Name), [**COPYRIGHT**] (year of publication), advance online publication, day month year (doi: 10.1038/sj. [JOURNAL ACRONYM])

For Book content:
Reprinted/adapted by permission from [**the Licensor**]: [**Book Publisher** (e.g. Palgrave Macmillan, Springer etc) [**Book Title**] by [**Book author**(s)] [**COPYRIGHT**] (year of publication)

Other Conditions:

Version 1.2

Questions? customercare@copyright.com or +1-855-239-3415 (toll free in the US) or +1-978-646-2777.